1-1-2012

An Acoustic Backscatter-Based Method for Estimating Attenuation Towards Monitoring Lesion Formation in High Intensity Focused Ultrasound

Siavash Rahimian
Ryerson University

AN ACOUSTIC BACKSCATTER-BASED METHOD FOR ESTIMATING ATTENUATION TOWARDS MONITORING LESION FORMATION IN HIGH INTENSITY FOCUSED ULTRASOUND

By

Siavash Rahimian

Bachelor of Engineering, Ryerson University, 2009

Toronto, Canada

A thesis

presented to Ryerson University

in partial fulfillment of the

requirements for the degree of

Master of Science

in Program of

Biomedical Physics

Toronto, Ontario, Canada, 2012

Author's Declaration

I hereby declare that I am the sole author of this thesis. This is a true copy of the thesis, including any required final revisions, as accepted by my examiners.

I authorize Ryerson University to lend this thesis to other institutions or individuals for the purpose of scholarly research.

I further authorize Ryerson University to reproduce this thesis by photocopying or by other means, in total or in part, at the request of other institutions or individuals for the purpose of scholarly research.

I understand that my thesis may be made electronically available to the public.

Siavash Rahimian

Abstract

"**An Acoustic Backscatter-based Method for Estimating Attenuation towards Monitoring Lesion Formation in High Intensity Focused Ultrasound"**

Siavash Rahimian

Master of Science, 2012

Department of Physics, Ryerson University

This work investigated the transient characteristics of tissue attenuation coefficients before, during and after HIFU treatment at different total acoustic powers in *ex vivo* porcine muscle tissues. Initially, preliminary data for the changes in attenuation coefficient induced in *ex vivo* porcine muscle tissues due to coagulation were obtained. The data indicated that changes in least squares attenuation coefficient slope ($\Delta\beta$) and attenuation coefficient intercept ($\Delta\alpha_0$) were both potentially reliable indicators of tissue thermal damage. Then, pulse-echo radiofrequency data were acquired to estimate $\Delta\beta$ and $\Delta\alpha_0$, and to construct $\Delta\beta$, $\Delta\alpha_0$, and B-mode images. Dynamic changes of $\Delta\beta$ and $\Delta\alpha_0$ were correlated with conventional B-mode ultrasound images over the HIFU treatment process. During HIFU treatment, $\Delta\beta$ and $\Delta\alpha_0$ increased rapidly with the appearance of bubble clouds in the B-mode images, and bubble activities appeared as strong hyperechoic regions in the B-mode images, caused fluctuations in the estimated $\Delta\beta$ and $\Delta\alpha_0$ values. After the treatment, $\Delta\beta$ and $\Delta\alpha_0$ gradually decreased, accompanied by fadeout of hyperechoic spot in the B-mode images, until they were stable at 10 minutes post-treatment, at 0.84 ± 0.11 [dB/(MHz.cm)] and 1.36 ± 0.19 [dB/cm], respectively. Finally the results showed that $\Delta\beta$ and $\Delta\alpha_0$ images had significantly higher contrast to speckle ratios than the conventional B-mode images.

Acknowledgements

I would like to give my sincere thanks to my supervisor, Dr. Jahan Tavakkoli, for his continuous support during the tenure of this thesis. His insights, comments, and directions have been most helpful in overcoming the numerous obstacles that we were facing.

I would like to thank Dr. Raffi Karshafian, Dr. Michael C. Kolios, and Dr. J. Carl Kumaradas, for their helpful comments, suggestions, and directions.

I would also like to thank Arthur Worthington along with all the faculty and staff of the department of physics for their resourcefulness and support.

This work was partially supported by the Ontario Research Fund-Research Excellence (ORF-RE Grant), and the Natural Sciences and Engineering Research Council of Canada (NSERC Discovery Grant) that were awarded to Dr. Jahan Tavakkoli.

Last but definitely not least, my most special thanks go to my lovely parents and my beautiful lovely sister for their love and encouragement since the day I was born, to my great friends without whom my life would probably have no meaning at all, and to my beautiful lovely niece who reminded me again of a certain something we call unconditional love.

Winter of 2012

Table of Contents

List of Symbols

φ	Velocity potential [m^2/s]
ϕ	Velocity potential phasor [m^2/s]
κ	Adiabatic compressibility of the medium [Pa^{-1}]
ρ_0	Mean density of the medium [Kg/m^3]
c_0	Small signal propagation speed of sound [m/s]
c	Finite amplitude speed of sound [m/s]
i	$\sqrt{-1}$
k	Wave number [rad/m]
k_0	Baseline wave number [rad/m]
$\underline{k}$	Complex wave number [rad/m]
f	Frequency [Hz]
f_c	Center frequency [Hz]
ω	Angular frequency [rad/s]
λ	Wavelength [m]
α	Amplitude attenuation coefficient [dB/cm]
α_0	Attenuation coefficient at f_c (attenuation intercept) [dB/cm]
β	Least squares attenuation slope (attenuation slope) [dB/(cm.MHz)]
β_1	Attenuation factor [$dB/(MHz^y.cm)$]
β_0	Attenuation intercept in the power law model [dB/cm]
α_a	Amplitude absorption coefficient [cm^{-1}]
α_s	Amplitude scattering coefficient [cm^{-1}]
μ_s	Intensity scattering coefficient [cm^{-1}]
μ_a	Intensity absorption coefficient [cm^{-1}]
μ	Coefficient of shear viscosity [(Kg.s)/m]
μ_B	Coefficient of bulk viscosity [(Kg.s)/m]
C_p	Specific heat capacity at constant pressure [J/(Kg.˚C)]
C_v	Specific heat capacity at constant volume [J/(Kg.˚C)]
K	Thermal conductivity [W/m.˚C]
$\bar{I}$	Time averaged intensity [W/cm^2]
I_{SA}	Free field spatially averaged intensity [W/cm^2]

p	Pressure [Pa]
p_0	Pressure amplitude at the source [Pa]
P	Pressure phasor [Pa]
F^{-1}	Inverse Fourier transform operator
P	Total acoustic power (TAP) [W]
D	Focal beam width at full width at half maximum [mm]
S_{in}	Mean signal measured inside a region of interest
S_{out}	Mean signal measured outside a region of interest
σ^2_{in}	Variances of the signal within the region of interest
σ^2_{out}	Variances of the signal outside the region of interest
C	Contrast between a given region interest and the background
S	Speckle contrast fluctuations
CSR	Contrast to speckle ratio

List of Tables

List of Figures

List of Appendices

1. Introduction and Background

1.1 High-Intensity Focused Ultrasound in High-Temperature Thermal Therapy

Recent trends in medicine have largely been focused on minimally invasive and noninvasive therapies. For example, solid abdominal tumors currently are preferably treated using laparoscopic techniques as opposed to the more traditional approach of being excised through abdominal surgeries (Vaezy et al., 2001b). In comparison to traditional open surgeries, the minimally invasive and noninvasive approaches have the advantages of reduced surgery times, tissue damage and side effects normally attributed to conventional surgeries. In addition, they greatly eliminate the need for transfusions, and consequently can greatly reduce the associated risks of infections. All of these advantages result in significantly shorter recovery times, and hospital stays for patients, and ultimately a reduction in health care costs.

High-temperature thermal therapy is one such minimally invasive or noninvasive therapeutic technique. Traditionally it has been employed to destroy tumors locally. During high-temperature thermal therapy, at the location where the tumor is located, the temperature of tissue is raised to levels approximately above 60°C, resulting in irreversible structural change (coagulative necrosis) of the cancerous tissue at that location. Details of tissue thermal damage are further explained in section 1.2. High-temperature thermal therapy can be targeted to various anatomical sites such as brain, eyes, bladder, kidney, and the prostate (ter Haar G. R., 1995).

There are various modalities for delivering the heat energy to the target area. Interstitial methods include antennas, radiofrequency electrodes, laser, and interstitial ultrasound transducers. A complete review of these interstitial methods was conducted by Stauffer et al. (Stauffer et al., 1995). However, in order for the therapeutic procedure to be truly noninvasive, usually external heating modalities are employed in extracorporeal approaches. The most common and promising external and noninvasive modality for high-temperature thermal therapy is high-intensity focused

ultrasound (HIFU). HIFU has the capability to deliver energy deep into the body and induce biological effects.

Initially it was in the 1940s that it was demonstrated that intensive focused ultrasound beams are able to produce regions of highly focused biological effects (Lynn & Putnam, 1944; Lynn et al., 1942). In the 1950s high intensity focused ultrasound (HIFU) was specifically developed for creating tissue destruction in brain (Fry F. J., 1958; Fry et al., 1955), and it was initially employed for treatment of Parkinson`s disease (Fry & Fry, 1960). In addition to treatment of Parkinson`s disease it was further employed for treatment of a few Ophthalmological problems such as treatment of glaucoma and retinal tears (Coleman, et al., 1985a; Coleman, et al., 1985b; Coleman , et al., 1985c). However, Introduction of L-dopa for treatment of Parkinson`s disease, and the introduction of lasers in eye surgery dampened any further interest and research efforts in the development and use of high intensity focused ultrasound in neurological and ophthalmological applications (ter Haar G. , 2006).

It was during the 1950s that it was first suggested that HIFU can be used for cancer therapy (Burov, 1956), by inducing coagulative necrosis as the main mechanism responsible for tumor treatment. In early 1980s, due to introduction and availability of more sophisticated imaging modalities for targeting and monitoring HIFU, and the medical community`s search for noninvasive treatments of benign prostatic hyperplasia (BPH), HIFU again emerged as the subject of interest within the medical research community and began to be employed on a larger scale (ter Haar G. , 2006). Currently some of HIFU's major applications in cancer therapy include treatment of benign prostatic hyperplasia and prostate cancer (Sanghvi, et al., 1999; Gelet, et al., 2000), fibroadenoma of breast tissue (Hynynen, et al., 1996), and uterine fibroids (Mencaglia, et al., 2000), in addition to treatment of cancer tumors of kidney, ovaries, and liver (Visioli, et al., 1999).

The use of megahertz ultrasound results in generation of a tight focus (millimeter-size) at a distance from the source. Additionally the HIFU beam can generate intensities anywhere in the range 1000-10000 W/cm^2 at the focal point (Vaezy, et al., 2001b). The combination of tight focusing and high intensities generated by the HIFU beam, result in generation of high temperatures at the focal spot without heating the surrounding spots. For example it has been shown that at 1.7 MHz, at focal peak intensities of 1500 W/cm^2, and exposure duration of 1-2 s,

temperatures at the focal spot can rise to levels in excess of 56°C in *ex vivo* liver tissue, resulting in instantaneous cell death and coagulative necrosis, with a margin of 6-10 cells between alive and dead cells at the periphery of the thermal damage zone (focal region) (ter Haar G. R., 1995; ter Haar & Robertson, 1993). The HIFU beam induces biological effects via thermal and mechanical mechanisms.

In thermal mechanism, the acoustic wave energy is converted to heat through a variety of mechanisms such as viscous shearing effects and relaxation processes (ter Haar G. , 1988). Throughout this project the focus is on tissue damage caused by thermal mechanisms.

In HIFU surgeries the biological effects of interest via mechanical mechanisms are results of tissue disruption. Very high-amplitude pressure waves usually cause rupturing of cellular and nuclear membranes, which further result in tissue death. In the mechanical realm, a variety of mechanisms such as radiation pressure, acoustic streaming, and acoustic cavitation are at play (ter Haar G. , 1988). These mechanisms are complicated, and they are still not very well understood. In addition, while these mechanisms are classified as mechanical mechanisms, it has been shown that they can significantly contribute to thermal mechanisms as well. For example, it is now recognized that acoustic cavitation enhances heating, which may be very advantageous in HIFU applications (ter Haar G. , 2006; Coussios, et al., 2007).

It should be mentioned that therapeutic applications of ultrasound are not limited to HIFU. Lithotripsy is one of the most established applications of therapeutic ultrasound and has been the most frequent treatment option for kidney stones since the early 1980s (Bailey, et al., 2003). In lithotripsy, lithotripters produce short (microsecond) focused pulses with peak positive pressures in the range of 20-140 MPa and peak negative pressures in the range of 8-15 MPa, at rates of 1-2 Hz (Bailey, et al., 2003). These pulses, usually referred to as acoustic shockwaves, are focused at the location of the kidney stones, causing their destruction. Physiotherapy is another one of the most established applications of therapeutic ultrasound (ter Haar G. , 2006). Physiotherapy ultrasound was originally used in the treatment of soft tissue injuries, and was originally thought of as an alternative to hot packs, microwaves, and radiofrequency methods of producing gentle heating (ter Haar G. , 2006). In addition to thermal mechanisms involved in physiotherapy ultrasound, currently studies are being conducted to exploit any possible beneficial non-thermal mechanisms that may exist (ter Haar G. , 2006). Finally, it should be mentioned that numerous

investigations are being conducted on the applicability of therapeutic ultrasound in fields such as drug delivery (Rosenthal, et al., 2004), gene therapy (Kim, et al., 1996), thrombolysis (Schafer, et al., 2005; Daffertshofer & Hennerici, 2003), and bone healing (Pilla, et al., 1990). The number and scope of these investigations continue to grow at an increasing rate. In one of the most recent books published on the topic of therapeutic ultrasound, Frenkel, et al. have produced a comprehensive review of therapeutic ultrasound (Frenkel, 2011), and provided detailed descriptions of different ultrasound mechanisms that produce biological effects in tissue.

1.2 Tissue Thermal Damage

Thomsen, through the application of gross and microscopic (qualitative and quantitative) pathologic techniques, has extensively studied the effects and mechanisms of thermal therapies in biological tissues, both *in vivo* and *in vitro* (Thomsen S. , 1999). A brief summary of that work is presented here.

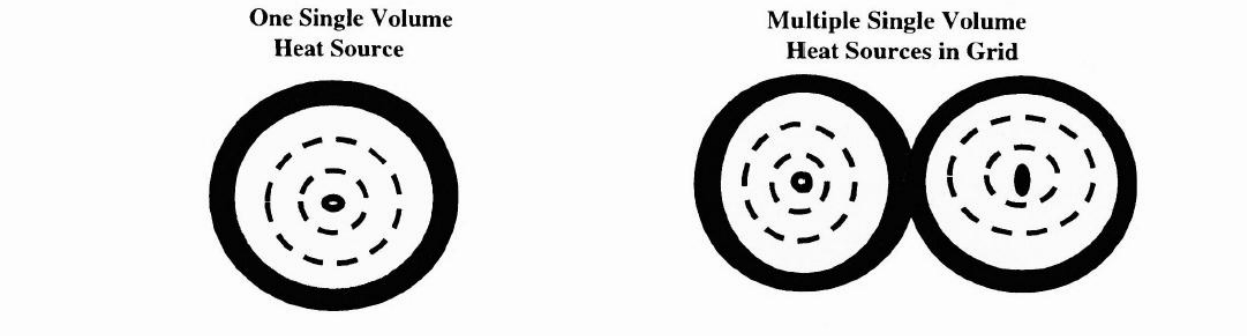

Figure 1-1 Schematic of concentric thermal damage zones around a single heat source volume, and multiple heat source volumes. The central holes are where the energy source is placed, and the dotted lines represent boundaries of thermal damage zones (Thomsen S. , 1999).

Around each heat source volume, concentric zones of thermal damage develop. These thermal damage zones are usually separated by distinct measurable boundaries. Depending on energy deposition distribution, tissue temperature, heating time, and tissue parameters, thermal lesions of various sizes and configurations are created. Therefore, beginning at the hotter center of the

concentric thermal damage zones and progressing towards the cooler periphery, the following damage zones can be present: 1) Ablation, 2) Carbonization, 3) Water Vaporization, 4) Structural Protein Thermal Coagulation (Denaturation), 5) Vital Enzyme Denaturation and Cellular Membrane Dissociation, 6) Red Thermal Damage Zone, 7)Necrosis, and 8) Wound Healing. The first five damage zones can be found in both *in vitro* and *in vivo* tissue targets, while the last three can only be found *in vivo* tissue targets.

1.2.1 Ablation

Ablation is defined as the physical removal of solid components of tissue (Thomsen S. , 1999). Depending on the energy delivery to the tissue, chunks, fragments, layers, cells, molecules, and ionized atoms can be removed from the tissue. Within the domain of thermal therapy, thermal tissue vaporization, combustion, or explosive fragmentation, can create holes, craters, or cuts. Explosive fragmentation (also referred to as the popcorn effect) is generally a characteristic feature of accelerated water or tissue vaporization. The rapid rate of vaporization leads to the collapse of the rapidly expanding superheated vapor bubbles in the heated tissue.

1.2.2 Carbonization

Carbonization is defined as the formation of black or nearly black residues on the surface of an ablative thermal lesion (Thomsen S. , 1999). It should be noted that tissue is an organic matter, and like all organic matter, when undergoing combustion reactions it is reduced to carbon and water. Carbonization is simply the result of reduction of tissue to carbon. The carbon layer is usually very thin. It can be measured microscopically as the lining of a hole or a crater, created as a result of rapid heating. It is particularly undesirable in laser interstitial thermal therapy since the carbon absorbs the light and prevents the transfer of energy to the surrounding tissue.

1.2.3 Water Vaporization

Water vapor formed close to the surface of tissue at temperatures below 100°C, can diffuse out of the tissue. But, at temperatures near or above 100°C, water vapor formation accelerates and the steam can no longer escape from the tissue by diffusion. Here, the vapor pockets grow larger and larger as the superheated steam expands. As the pressure increases, the vapor pockets burst open sometimes throwing tissue fragments into the air. Usually, the zone of water vaporization has a fairly distinct and measurable border (Thomsen S. , 1999).

As it is evident, ablation, carbonization, and water vaporization are all results of very high temperatures and rapid energy deposition. More relevant to our work, is the high-temperature thermal therapy that results in structural protein thermal coagulation (denaturation).

1.2.4 Structural Protein Thermal Coagulation (Denaturation)

Structural proteins are proteins that form the extracellular matrix, and the cytoskeleton of all cells. The changes that are caused in tissue structure due to thermal coagulation are mainly results of breakdown of structural proteins and cell shrinkage in the tissue (Thomsen S. , 1999). These changes can be detected and measured through changes in tissue color and opacity. Most thermally coagulated tissues become lighter colored and more opaque with the exception of fat and collagen-rich tissues which become more translucent. The borders of the coagulum within the tissue are usually grossly measureable. Microscopically, within the coagulum, beginning from the hotter center going to the cooler periphery, there are several concentric thermal damage zones with distinct boundaries. These zones include: 1) collagen denaturation 2) muscle cell birefringence changes (loss of the birefringent properties of muscle proteins due to the disruption of their tertiary molecular structures), and 3) cell shrinkage (disruption of organelles and denaturation of the proteins and DNA within the cell, while the cell looks intact). All of these zones are due to thermal denaturation of structural proteins. Thomsen has extensively elaborated on these zones in her study (Thomsen S. , 1999).

1.2.5 Vital Enzyme Denaturation and Cellular Membrane Dissociation

Vital enzyme denaturation is defined as the thermal denaturation of vital enzymes through protein denaturation processes similar to structural protein denaturation. However, vital enzyme denaturation occurs at lower temperatures, and shorter heating times in comparison to thermal coagulation. Therefore, vital enzyme denaturation usually occurs at the cooler periphery of the lesion (Thomsen S. , 1999).

Cellular membrane dissociation is simply a major disruption of the cellular membranes. The membranes of cells and organelles are layers of hydrophilic or hydrophobic lipoproteins. These membranes form the boundaries between the interiors and exteriors of structures such as cells or organelles. The membranes are critical components of cells and as a result, membrane disruption usually leads to inevitable cell death. Minor disruptions however, can be repaired allowing the cell or the organelle to survive.

1.2.6 Red Thermal Damage Zone

Red thermal damage zone is defined as a grossly apparent red zone that develops at the periphery of the coagulation zone in living organs with an intact blood supply (Thomsen S. , 1999). This zone is a consequence of thermal damage to the blood vessels in the target area, and a combination of physiological responses to heating. The result is hemostasis (cessation of blood flow), hemorrhage (escape of blood from blood vessels), and hyperhemia (increased blood flow). Hemostasis tends to be close to the coagulum, while hemorrhage and hyperhemia are usually more peripheral. But overall, the three phenomena are intermixed and do not form distinct microscopic zones within the red zone (Thomsen S. , 1999).

1.2.7 Necrosis

The full extent of lethal thermal damage can only be found out when all the damaged cells that are not capable of surviving undergo necrosis and die. It takes 1 to 5 days for the lethal thermal damage to reveal itself by necrosis. The general mechanisms of necrosis in thermal

lesions include, thermal coagulative necrosis, lytic necrosis (low temperature dissociation of lysosome membranes), ischemic necrosis (blockage of blood supply), and apoptosis (programmed cell death, here triggered by heat) (Thomsen S. , 1999). Thermal coagulative necrosis tends to occur closer to the heat source, while the latter three tend to occur near the periphery of the coagulum. In thermal coagulative necrosis, the cells may even appear intact under the microscope, however they are dead. In addition, since the cells' intrinsic proteolytic and lipolytic enzymes have been disabled due to vital enzyme denaturation, the cells will not undergo cellular and nuclear disintegration. Finally, there will be no blood flow to transport the inflammatory cells to digest all the dead cells (by releasing lipase and protease). The coagulum persists until new blood vessels invade into the necrotic tissue and bring in the inflammatory cells.

In several *in vivo* studies (Thomsen, et al., 1995) it has been shown that the outer boundary of the red thermal damage zone corresponds to the boundary of tissue necrosis. Therefore, the delayed effect of necrosis can be predicted *in vivo* by the extent of the red zone that develops during and/or immediately after thermal coagulation.

1.2.8 Wound Healing of Thermal Damage

Thermal damage wound healing is defined as the regeneration and replacement of necrotic tissue. It consists of organization of the necrotic debris, tissue regeneration and/or scar formation (Thomsen S. , 1999; Cohen, et al., 1992). During the organization step, the necrotic tissue is broken down into manageable components and removed in order for the healing process to take place. The smaller components are released into the circulation, while the larger components are phagocytized (eaten) by macrophages. The organization begins at the periphery of the necrotic area and proceeds into the lesion (Thomsen S. , 1999).

After the completion of the organization phase, several chemical and hormonal factors signal the initiation of tissue regeneration and/or scar formation. Tissue regeneration is initiated by the release of growth factors. These growth factors stimulate proliferation and differentiation of new tissue cells. In addition to growth factors, vascular growth factors stimulate new blood vessel

growth, and fibroblast growth factors stimulate fibroblast proliferation and collagen formation. The collagen feeds and supports the functioning tissue.

However, depending on the tissue type, vascular and fibrotic proliferations sometimes overcome the regeneration of the tissue. This leads to formation of fibrous granulation tissue, ultimately leading to formation of fibrous scar tissue. As the scar ages, many blood vessels are resorbed, the collagen fibers become larger and larger and more densely packed, and the entire scar shrinks (Cohen, et al., 1992).

Among the mechanisms mentioned above, structural protein thermal coagulation (denaturation) is most pertinent to HIFU therapies. Additionally, when dealing with *in vivo* targets, red thermal damage zone, necrosis, and wound healing become relevant as well.

1.3 Monitoring HIFU

Monitoring in high-temperature thermal therapy serves two purposes. The first purpose is ensuring that the target volume is completely treated (thermally damaged). The second purpose is ensuring the safety of sensitive structures near or outside the target volume. Ideally such a monitoring should be conducted in real-time using a closed loop system. While microscopic pathological examination provides a lot of information, it cannot be employed for real-time monitoring and assessment of the induced tissue thermal damage. Instead, usually gross pathological effects, or the temperature elevations causing them are employed for monitoring purposes.

In the realm of HIFU, the dominant form of thermal damage is coagulative necrosis. Following the above methodology, the monitoring and assessment methods employed for HIFU therapies are divided into two major categories. In the first category, it is the thermal damage and structural changes in tissue (gross pathological effects) that are detected and monitored. In the second category, also known as ultrasonic thermometry, it is the temperature that is monitored. Monitoring the temperature at the targeted area in the tissue is a very valuable tool, since it provides feedback to the interventionist, or an automated system. Maintaining a high temperature for an extended period of time will cause the necessary structural changes to destroy the targeted

area in the tissue. Both categories of monitoring and assessment are conducted through a number of invasive and noninvasive methods.

1.3.1 Invasive Monitoring Methods

1.3.1.1 Thermocouples

Calibrated thermocouples are fairly accurate and inexpensive temperature measurement devices that can readily be fabricated for different purposes. However, they are prone to errors especially when they are exposed to electromagnetic and ultrasonic fields. In addition, they can cause field distortions and perturbations, distorting the heating of the targeted location in tissue. Finally, they often heat up and they conduct this heat along their lengths, causing thermal damage to the surrounding area (Waterman, 1995).

1.3.1.2 Fluoroptic Thermocouples

Fluoroptic probes are fiber optic temperature sensors. These sensors are based on optical properties of phosphorescent materials. The temperature of the sensor and its surrounding environment is determined by measuring the decay time of its emitted light (since the decay time varies with temperature). Fluoroptic probes are nonmetallic and therefore they do not cause field distortions and perturbations (Waterman, 1995). In addition, they do not heat up therefore they do not cause any thermal damage to the surrounding area.

Whether metallic or nonmetallic, all the interstitial point temperature probes have a common disadvantage. The insertion of a few static sensors provides too few samples of temperature to provide info about the entire volume of interest. While, there are various techniques that can be employed to overcome this issue (Waterman, 1995) generally a large number of invasive point probes are required to map out the entire region of interest effectively. Therefore, noninvasive thermometry or imaging modalities are usually preferred for monitoring the progression of treatment. In addition to being noninvasive, these modalities provide a lot more information about the volume of interest and they are able to map out the region of interest quite effectively.

1.3.2 Noninvasive Monitoring Methods

X-ray imaging, magnetic resonance imaging (MRI), and ultrasound imaging have all been used as noninvasive methods for monitoring and assessment of tissue thermal damage in HIFU surgeries (Vaezy, et al., 2001b). However, MRI and ultrasound imaging have been more extensively studied, and more extensively employed for monitoring HIFU. As it was mentioned before, these modalities are employed in two broad categories of methods. First category are methods that are sensitive to temperature changes (such as ultrasound thermometry, or MR thermometry), and the second category are methods that are sensitive to changes in tissue structure. In the following subsections X-ray and MRI will be briefly discussed, and the next section will be entirely devoted to ultrasound imaging.

1.3.2.1 X-ray

X-ray was the earliest imaging modality for guidance and monitoring of HIFU. It was used in treatment of Parkinson's disease (Fry & Fry, 1960). X-ray images were used to monitor and map the area where the HIFU lesions (induced change in tissue structure) were present. X-ray guidance is used in thrombolysis approaches (Siegel, et al., 2000), and shock-wave lithotripsy for destruction of kidney stones (Chaussy, Brendel, & Schmiedt, 1980). However, X-ray has the usual problem of exposing both the patient and the interventionist to high doses of ionizing radiation during rather long HIFU treatment procedures.

1.3.2.2 Magnetic Resonance Imaging

T1-weighted MR imaging shows some dependence on both temperature and permanent structural changes in tissue (Matsumoto, et al., 1994; Hynynen, et al., 1995). The aim of using this parameter is to combine fast imaging times with high temperature sensitivities and resolutions over the range of temperatures that are relevant to HIFU therapy. However, the advantage of fast imaging times is offset by a decrease in temperature resolution, while, longer imaging times result in only a slight increase in temperature resolution, at the expense of low temporal resolution and low temperature sensitivity (Matsumoto, et al., 1994). T2-weighted MR

imaging on the other hand predominantly shows dependence on permanent structural changes (Hynynen, et al., 1993).

It has been suggested that diffusion coefficient of water parameter is the most straightforward MR imaging parameter for monitoring temperature *in vivo* (Le Bihan, et al., 1989). Phase difference imaging has been used to evaluate diffusion coefficient of water in the region of interest (ROI) and to relate the diffusion coefficient back to temperature (Bleier, et al., 1991). However, generation of diffusion images is a time-consuming and to some extent complex process.

Proton resonant frequency (PRF) shift has been shown to be temperature dependent (Ishihara, et al., 1995), and has been studied on various types of tissues both *in vitro* and *in vivo* (Stollberger, et al., 1997; Moriarty, et al., 1998; Peters, et al., 1998; Heisterkamp, et al., 1999). It has been shown that PRF shift temperature mapping is so far the only tissue independent method (Peters, et al., 1998). In the PRF method, given the direct proportionality of temperature change (ΔT) to phase difference ($\Delta\varphi$), temperature maps are constructed from phase difference ($\Delta\varphi$) images (Ishihara, et al., 1995).

Significant advances have so far been made in the application of MRI for guidance of thermal therapies and more specifically HIFU therapy (Jolesz & Hynynen, 2007). Currently MRI can provide good anatomical resolution of soft tissue, therefore providing good accuracy for localization of tumors and HIFU induced lesions. However, it is still restricted by factors such as, low image acquisition speeds (low temporal resolution), high costs, and the requirement for minimal use of metallic parts. The ultrasound transducer must be properly coupled with the MRI machine in such a way so that neither device interferes with the functionality of the other. The presence of ferromagnetic components of electronic parts and the need to fit everything within the confined space of the MRI chamber have made the coupling task especially difficult. Due to these complexities and the associated costs of using MRI for guidance of HIFU therapies, many research groups both in the academia and in the industry have been looking at ultrasound imaging as an attractive and promising modality for real-time monitoring of HIFU procedures.

1.4 Monitoring HIFU Using Ultrasound

1.4.1 Thermal Lesion Detection Based on Conventional B-mode Imaging

In the very first studies in which ultrasound was used for monitoring of high temperature thermal therapies, it was noted that there was always a region with very high echogenicity at the location where the thermal lesion was being created. The high echogenicity was due to the formation and presence of strongly scattering gas bubbles. These gas bubbles were formed in the tissue due to heating. As a result, one of the most straightforward methods of lesion detection and visualization has always been the ultrasound B-mode imaging technique itself (Vaezy, et al., 2001a; Arefiev, et al., 1998). The echogenicity was further quantified in the hyperechoic regions for the purpose of evaluation of tissue thermal damage after each HIFU exposure (Seo, et al., 2002). However, it has been shown that the hyperechoic region is consistently smaller than the actual coagulated region in the tissue, and it has a different shape. Therefore, the hyperechoic region is not considered to be an accurate indicator of thermal damage in tissue. Finally, the essence of using B-mode imaging for monitoring HIFU is the presence of cavitation, and microbubble activities (Zheng & Vaezy, 2010). However, it has been shown that cavitation and the presence of microbubble activities strongly correlate to unpredictable HIFU lesions (Hynynen K. , 1991), and in applications where avoidance of microbubble activities is desirable, relying on B-mode imaging will be problematic.

1.4.2 Thermal Lesion Detection Based on Estimation of Temperature Change

By detecting changes in the speed of sound as a function of temperature, temperature can be estimated. There are a lot of methods based on this technique (Anand, et al., 2007; Arthur, et al., 2003; Simon, et al., 1998; Seip & Ebbini, 1995). However, it was shown that variations in speed of sound as a function of temperature close to 50°C were very small, and as a result the sensitivity of temperature estimation at temperatures close to 50°C were found to be low (Bamber & Hil, 1979). In addition, in experiments on *ex vivo* porcine liver, it was shown that speed of sound increased monotonically as the temperature rose to 50°C, and after that as the temperature rose to levels above 50°C, the speed of sound monotonically decreased (Bloch, et

al., 1998). This behavior of speed of sound imposes great limitations on estimating the temperature using changes in speed of sound.

While temperature can indeed be estimated from changes in speed of sound, there is currently very little data available, tabulating the relationship between temperature and speed of sound for different types of tissue. Furthermore, even if such data was available, due to inter-patient variability, accurate temperature estimation would still be subject to serious limitations. For example, it has been shown that different people have different percentages of fat in their livers. This in turn leads to a wide range of temperature-dependent speed of sound profiles (Miller, Bamber, & Meany, 2002). Along with the inter-patient variability, other factors such as nonlinearity, thermal expansion, the effect of different intensity levels, and finally accuracy of measurement *in vivo*, have so far imposed serious limitations on temperature measurement using ultrasound (Damianou, et al., 1997).

1.4.3 Thermal Lesion Detection Based on Estimation of Changes in Elastic Modulus

Another physical parameter that can be exploited for HIFU lesion detection is the tissue elastic modulus (stiffness). More specifically, changes in tissue elastic modulus can be used for estimating the size and location of HIFU lesions. It was shown that HIFU lesions can be six to twelve times stiffer than normal tissue (Shi, et al., 1999). In a technique known as sonoelasticity imaging (Parker, et al., 1990), a low frequency vibration is applied to liver sample containing HIFU-induced lesions, and then using Doppler spectral analysis, the velocity pattern in the region of interest is measured. In a different study, the application of increased load and external harmonic stresses for estimating changes in mechanical properties of tissue as a function of HIFU exposure were studied (Righetti, et al., 1999). Finally, in a method known as acoustic radiation force imaging (ARFI) (Fahey, et al., 2004), internal forces within the tissue were exploited to estimate changes in mechanical properties of tissue as a function of HIFU exposure for the purpose of detection and localization of HIFU-induced lesions.

So far elastographic measurement techniques have proven feasible for detection and characterization of HIFU-induced lesions. But, except for the ARFI technique, all the other techniques rely on the presence of an external source of stress in order to cause the desired displacement in the tissue. Consequently, extra instruments will always be needed to generate this excitation. In addition, the application of the stress signal to deep-seated tissues, and regions that are generally not accessible, has proven to be rather problematic, imposing further limitations on this technique. Finally, the elastographic methods rely on the generation of elasticity maps before, and after the HIFU exposure, and these elasticity maps are sometimes contaminated by motion artifact distortions (Souchon, et al., 2003).

Recently, the topic of ultrasound guided HIFU was reviewed by Tavakkoli and Sanghvi (Tavakkoli & Sanghvi, 2011). Their review thoroughly covers the developmental history of ultrasound guided HIFU, and various methods of ultrasonic guidance and control, with more emphasis on various features and characteristics of systems that are currently available in clinical applications.

1.5 Ultrasound Interactions with Tissue

Many ultrasound properties of soft biological tissues are similar to aqueous solutions and suspensions. Consequently, very often the propagation of ultrasound waves in soft tissues is approximated by the propagation equation in fluids. For an inviscid, linear medium, the velocity potential,ϕ, is given by finding the solutions to the following linear wave equation (Cobbold, 2007),

$$\nabla^2\phi - \kappa\rho_0 \frac{\delta^2\phi}{\delta t^2} = 0 \qquad (1.1)$$

where ρ_0 is the mean density of the medium, and κ, is the adiabatic compressibility, which is also the reciprocal of the adiabatic bulk (elastic) modulus. In Cartesian coordinates, a plane longitudinal wave propagating in lossless, infinite medium can be written as,

$$\phi(\mathbf{r}: t) = \phi(c_0 t - \tilde{\mathbf{k}}.\mathbf{r}) \qquad (1.2)$$

where $\tilde{\mathbf{k}}$ is a unit vector always pointing in the direction of propagation. **r** represents the position vector, and c_0 represents the small-signal propagation speed. For the particular case of a simple harmonic wave, equation 1.2 can be written as,

$$\phi(\mathbf{r}: t) = \phi_0 e^{jk(c_0 t - \tilde{\mathbf{k}}.\mathbf{r})} \tag{1.3}$$

where $k = \frac{\omega}{c_0}$, is the wave number. Substitution of equation 1.3 into equation 1.1 shows that 1.3 is a solution to the homogeneous wave equation, and the propagation speed is,

$$c_0 = \frac{1}{\sqrt{\kappa \rho_0}} \tag{1.4}$$

As a result, equation 1.1 can now be written in terms of propagation speed,

$$\nabla^2 \phi - \frac{1}{{c_0}^2} \frac{\delta^2 \phi}{\delta t^2} = 0 \tag{1.5}$$

The simple 1-dimensional case of equation 1.5, in Cartesian coordinates is,

$$\frac{\delta^2 \phi}{\delta x^2} - \frac{1}{{c_0}^2} \frac{\delta^2 \phi}{\delta t^2} = 0 \tag{1.6}$$

The solution to equation 1.6 can be expressed as (Cobbold, 2007),

$$\phi(x: t) = \phi_1(c_0 t - x) + \phi_2(c_0 t + x) \tag{1.7}$$

where ϕ_1 and ϕ_2 represent velocity potentials for waves propagating in the positive and negative x-directions, respectively. For the case of a sinusoidal source located on the plane, x = 0, there will be a plane harmonic wave propagating in the positive and negative x-directions. For the plane harmonic wave propagating in the positive x-direction, the approximate steady-state velocity potential will be,

$$\phi(x: t) = \phi_0 \cos(\omega t - kx) \tag{1.8}$$

If we consider a plane harmonic wave, with the velocity potential phasor being given as,

$$\phi(\mathbf{r}: t) = \phi(\mathbf{r}: \omega) e^{j\omega t} \tag{1.9}$$

then substituting equation 1.9, into equation 1.1, for a viscous fluid yields the Helmholtz equation,

$$\nabla^2 \Phi + \underline{k}^2 \Phi = 0 \tag{1.10}$$

Where $\underline{k} = \frac{k}{\sqrt{1+j\omega\kappa(\mu_B+\frac{4}{3}\mu)}}$ is a complex wave number (Cobbold, 2007). If the wave is propagating in a medium with low viscous loss, then the complex wave number can be approximately expanded into,

$$\underline{k} = k\left[1 - \frac{j\omega\kappa}{2}\left(\mu_B + \frac{4}{3}\mu\right)\right] = k - j\alpha \tag{1.11}$$

α in equation 1.11 is the amplitude attenuation coefficient given as (Cobbold, 2007),

$$\alpha = \frac{\omega^2}{\rho_0 {c_0}^3}\left(\mu_B + \frac{4}{3}\mu\right) \tag{1.12}$$

For the case of a sinusoidal source located on the plane, x = 0, there will be a plane harmonic wave propagating in the positive and negative x-directions. For the wave propagating in the positive x-direction, the approximate steady-state velocity potential will be,

$$\phi(x{:}\,t) = \phi_0 e^{-\alpha x}\cos(\omega t - kx) \tag{1.13}$$

Equation 1.13 is essentially an expanded form of equation 1.8, describing an attenuated plane harmonic wave.

As ultrasound propagates through tissue the amplitude decreases as a function of depth. The ultrasound wave is attenuated through scattering, and absorption. While, it is the combination of the scattering, and absorption processes that contribute to the total attenuation, α, the greater loss of energy (75-95% of total attenuation) is due to the effect of absorption processes (Parker, 1983). Absorption processes are due to viscous losses, thermal conduction, and relaxation processes (Cobbold, 2007).

By assuming purely adiabatic conditions for a compressional wave, and ignoring the effects of bulk viscosity, Stokes obtained the following classical equation for the absorption coefficient in fluids (Cobbold, 2007),

$$\alpha_a \approx \frac{2\omega^2\kappa\mu}{3c_0} \tag{1.14}$$

where μ is the shear viscosity. Kirchhoff further added the effect of thermal conduction to the classical absorption coefficient equation and obtained the following equation (Cobbold, 2007),

$$\alpha_a = \frac{\omega^2 \kappa}{2c_0}\left[\frac{4}{3}\mu + (\gamma - 1)\frac{K}{C_p}\right] \quad (1.15)$$

where $\gamma = \frac{C_p}{C_v}$ is the ratio of specific heat capacities. C_p is the specific heat capacity at constant pressure, while C_v is the specific heat capacity at constant volume. Finally, K is the thermal conductivity of the medium. The contribution of thermal conduction to absorption processes is due to the fact that heat always flows from the compression regions to rarefaction regions of the waves. Compressed regions on re-expansion do less work in comparison to the amount of work that initially forced them into compression. Therefore energy is always lost to the surrounding. Additionally, it has been shown that structural and thermal relaxation processes can significantly affect the passage of a compressional wave. To account for these loss mechanisms, an additional bulk viscosity term μ_B is often added to equation 1.15, resulting in the following absorption coefficient equation (Cobbold, 2007),

$$\alpha_a = \frac{\omega^2 \kappa}{2c_0}\left[\frac{4}{3}\mu + \mu_B + (\gamma - 1)\frac{K}{C_p}\right] \quad (1.16)$$

As it was mentioned before, the attenuation coefficient, α, is due to the combination of the effects of absorption, α_a, and scattering of ultrasound energy in the medium. The attenuation coefficient α, is a frequency dependent term, and at the low end of frequency spectrum (low MHz rage) its behaviour is mostly dominated by the effects of absorption as opposed to scattering (Szabo, 2004). Based on attenuation measurement data obtained from soft biological tissues and other similar media, the frequency dependent attenuation coefficient is usually modeled with good approximation by the following model,

$$\alpha(f) = \beta_0 + \beta_1 |f|^y \quad (1.17)$$

where β_0, referred to as the attenuation intercept, is usually zero, y is a power law exponent that usually lies in the range from 1 to 2, and β_1 is the attenuation factor in $\frac{dB}{MHz^y.cm}$ (Szabo, 2004; Cobbold, 2007). Furthermore, within practical bandwidths, the attenuation of soft tissues are sometimes modelled by the following linear relationship (Ophir, et al., 1984),

$$\alpha(f) = \alpha_0 + \beta.(f - f_c) \quad (1.18)$$

where α_0 is the attenuation coefficient at the center frequency (f_c) of the transmitted pulse in $\frac{\text{dB}}{\text{cm}}$, usually referred to as the attenuation intercept, and β is the least squares attenuation slope in $\frac{\text{dB}}{\text{MHz.cm}}$, usually referred to as the attenuation slope.

1.6 Changes in Ultrasound Attenuation of Tissue Due to Heating

There have been various studies conducted based on changes in ultrasound tissue properties (e.g., backscattering, attenuation coefficient, and speed of sound) as a function of temperature or thermal dose (Damianou, et al., 1997; Bush, et al., 1993; Gertner, et al., 1997; Goss, et al., 1979). In all of these studies, it is observed that as the temperature of tissue rises, and ultimately, as the tissue coagulates, there is an increase in ultrasound attenuation. For example, in the study conducted by Bush, et al., the attenuation intercept, α_0, for *ex vivo* porcine liver almost doubled from 2dB/cm, to 4dB/cm at 5MHz (Bush, et al., 1993). Gertner, et al. similarly showed that the attenuation intercept, α_0, for *ex vivo* bovine liver increased from 2dB/cm to 3.6 dB/cm, at 5MHz, while the attenuation slope, β, increased from 0.22dB/(cm.MHz) to 0.38 dB/(cm.MHz) (Gertner, et al., 1997). Based on these results, the frequency dependent ultrasound attenuation, and its changes as a function of temperature and thermal dose may be a valuable tool in gaining more information about the location of the tissue at which the thermal damage occurs. Therefore, Measurement of change in ultrasound attenuation can be exploited for monitoring of high temperature thermal therapies such as HIFU (Ophir, et al., 1984; Bush, et al., 1993; Zhang, et al., 2009).

1.7 Ultrasound Attenuation Estimation for Monitoring HIFU

As it was previously stated above, there is a dramatic increase in the ultrasound attenuation slope, β, and ultrasound attenuation intercept, α_0 as tissue temperature increases. This dramatic increase can be exploited for differentiating normal and thermally coagulated tissue. Ultrasound attenuation slope and attenuation intercept measurement can be directly applied to the region of interest in the tissue, through analysis of the RF backscattered ultrasound signal.

Ophir, et al. extensively discussed various methods of attenuation estimation using the RF backscattered ultrasound signals (Ophir, et al., 1984). Using attenuation mapping it was shown that a thermally coagulated region (HIFU-induced lesion) of *ex vivo* liver tissue can be detected (Ribault, et al., 1998). Bevan and Sherar developed two sets of algorithms for generating attenuation maps for monitoring of high temperature thermal therapies (Bevan & Sherar, 2001a; Bevan & Sherar, 2001b). One algorithm relies on detecting changes in slope of the logarithm of the envelope of the RF signals, while the other one is based on the shift in the center frequency of the backscattered ultrasound signals. Seip, et al. conducted a comparison of a few detection algorithms, including attenuation change, for real-time monitoring and control of HIFU lesions in *in vivo* canine prostates using RF backscattered ultrasound signals (Seip, et al., 2002). Most recently Zhang, et al. studied the feasibility of using attenuation estimation using the RF backscattered ultrasound signals, along with other RF-based methods for monitoring of HIFU in transparent tissue mimicking phantoms and *ex vivo* bovine livers (Zhang, et al., 2009).

1.8 Thesis Hypothesis and Outline

This study has two main objectives. First objective is design and development of a system (both hardware, and software) capable of acquiring backscattered ultrasound RF data in the before, during, and after phases of any given HIFU procedure. Second objective is design and implementation of suitable algorithm(s) capable of quantitatively characterizing changes in attenuation of tissue in locations where HIFU lesions are created, in real-time, using the acquired backscattered ultrasound RF data. It is hypothesized that changes in the attenuation of HIFU lesions can be estimated with respect to initial attenuation of normal tissue, using the acquired backscattered RF data. The second chapter covers the theoretical basis, the experimental setup, and methodology associated with attenuation measurement using the insertion-loss method, along with the theoretical basis of attenuation estimation using backscattered ultrasound pulses. Finally, two frequency domain algorithms (attenuation slope and attenuation intercept algorithms) are developed and presented along with the experimental setup and the methodology pertaining to attenuation estimation using backscattered ultrasound RF data.

In the third chapter, initially attenuation measurement results using the insertion-loss technique for normal and coagulated *ex vivo* porcine muscle tissues are presented. Then, using the attenuation slope and attenuation intercept algorithms the transient characteristics of tissue attenuation coefficient parameters ($\Delta\beta$ and $\Delta\alpha_0$) before, during and after HIFU treatment at different total acoustic powers in *ex vivo* porcine muscle tissues, are investigated. Finally, using the two algorithms, $\Delta\beta$ and $\Delta\alpha_0$ images (attenuation maps) are generated. These attenuation maps are correlated with B-mode images, and the imaging performance of these attenuation maps are compared with each other and with conventional B-mode imaging.

The fourth and final chapter of this thesis, is a summary of important results presented in the preceding chapter, and additionally includes a discussion of concerns and future prospects of this study.

2. Methodology

2.1 Theoretical Basis of Attenuation Measurement

2.1.1 Attenuation, Absorption, and Scattering

Attenuation is defined as the loss of energy that an ultrasound wave experiences as it passes through a medium. This loss of energy is due to absorption and scattering (Szabo, 2004). Absorption results in the conversion of the wave energy into heat energy, while scattering represents the redirection of the wave energy along different paths that are different from the path of the incident wave. The scattered wave energy can be either absorbed or be further scattered (multiple scattering). So, to summarize, attenuation accounts for the effects of both absorption and scattering. In the simplest scenario it is assumed that the ultrasound wave passing through the medium is an ideal plane continuous wave, and this plane wave is incident on a given specimen. Assuming that the specimen is perfectly matched to the surrounding coupling medium, the energy exiting from the specimen in the direction of the incident wave can be calculated by considering the cross sectional area at each incremental distance that the wave propagates through. Figure 2-1 is an illustration of this scenario.

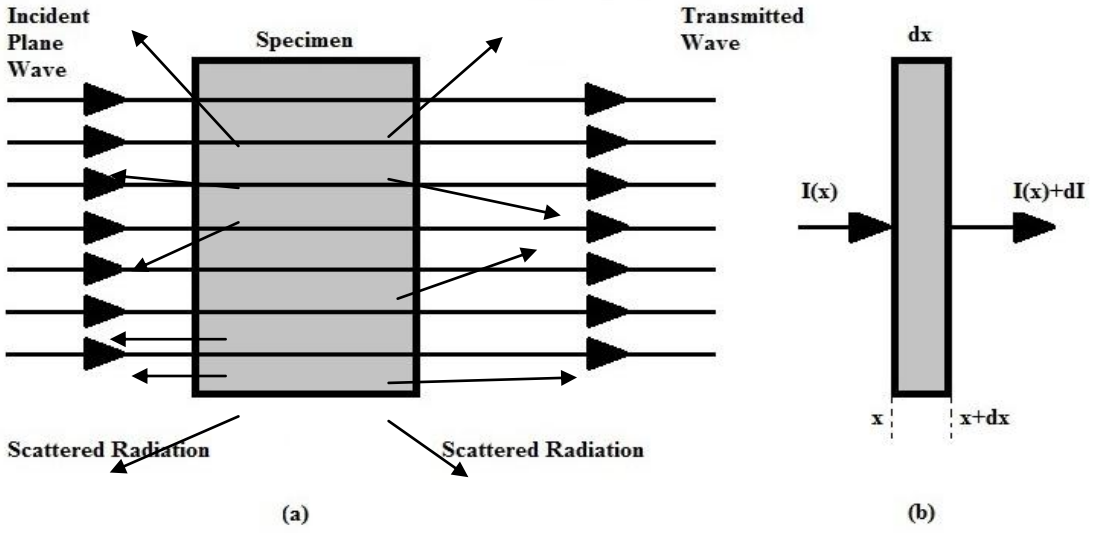

Figure 2-1 (a) The absorbed, scattered, and attenuated waves passing through a specimen, and (b) change in intensity of a plane wave as a result of its passage through an incremental propagation distance dx

Both the scattered power and the absorbed power are proportional to the time averaged intensity $\bar{I}(x)$ and the incremental propagation distance, dx. Over the incremental propagation distance dx, the change in time-averaged intensity due to scattering will be (Cobbold, 2007),

$$d\bar{I_s} = -\mu_s \bar{I}(x)dx \tag{2.1a}$$

where μ_s is the intensity scattering coefficient. Converting from intensity scattering coefficient to amplitude scattering coefficient, $\mu_s = 2\alpha_s$, results in,

$$d\bar{I_s} = -2\alpha_s \bar{I}(x)dx \tag{2.1b}$$

where and α_s is the amplitude scattering coefficient. Similarly, over the incremental propagation distance dx, the change in time-averaged intensity due to absorption will be,

$$d\bar{I_a} = -\mu_a \bar{I}(x)dx \tag{2.2a}$$

$$d\bar{I_a} = -2\alpha_a \bar{I}(x)dx \tag{2.2b}$$

where μ_a is the intensity absorption coefficient, and α_a is the amplitude absorption coefficient. So, over the incremental propagation distance dx, the overall change in time-averaged intensity due to both processes will be,

$$d\bar{I} = d\bar{I_s} + d\bar{I_a} = -2(\alpha_s + \alpha_a)\bar{I}(x)dx \tag{2.3}$$

therefore,

$$\frac{d\bar{I}}{\bar{I}(x)} = -2(\alpha_s + \alpha_a)dx \tag{2.4}$$

By taking $\bar{I}(0)$ as the time-averaged intensity at x=0, $\bar{I}(x)$, the time-averaged intensity at any given location x can be found by integration, yielding the following (Cobbold, 2007),

$$\bar{I}(x) = \bar{I}(0)e^{-2(\alpha_s+\alpha_a)x} = \bar{I}(0)e^{-2\alpha x} \tag{2.5}$$

where α is the amplitude attenuation coefficient. The units of α given at a specific frequency are generally expressed in terms of $\frac{\text{Np}}{\text{cm}}$. It is however advantageous to deal with α in terms of $\frac{\text{dB}}{\text{cm}}$. The advantage of the dB scale is in cases where the total attenuation over a given path involves the contributions of several different attenuation coefficients. In such cases, the total attenuation can quickly be estimated by simply adding all the attenuation coefficients over the given path. In order to express attenuation coefficient in terms of $\frac{\text{dB}}{\text{cm}}$, first the terms of equation 2.5 are slightly

rearranged and then the logarithm to the base 10 of both sides is taken. Both sides of the equation are further multiplied by 10, resulting in the following,

$$10\log\left[\frac{\bar{I}(0)}{\bar{I}(x)}\right] = 20\alpha_{NP}x\log e = 8.686\alpha_{NP}x \tag{2.6}$$

Amplitude attenuation coefficient expressed in units of $\frac{dB}{cm}$ will be $\alpha_{dB} = 8.686\alpha_{NP}$. The conversion between $\frac{dB}{cm}$ and $\frac{Np}{cm}$ can be achieved through the following pair of formulas (Cobbold, 2007),

$$\alpha_{dB} = 8.686\alpha_{Np} \tag{2.7}$$

$$\alpha_{Np} = 0.1151\alpha_{dB} \tag{2.8}$$

In terms of intensity the amplitude attenuation coefficient expressed in $\frac{dB}{cm}$ will be,

$$\alpha_{dB} = \frac{10}{x}\log[\frac{\bar{I}(0)}{\bar{I}(x)}] \tag{2.9}$$

For typical values of attenuation coefficient (values that are not too large), the square of pressure amplitude is proportional to average intensity, $p_0(x)^2 \propto \bar{I}(x)$. Therefore, the amplitude attenuation coefficient can additionally be written in terms of pressure amplitude as,

$$\alpha_{dB} = \frac{20}{x}\log[\frac{p_0(0)}{p_0(x)}] \tag{2.10}$$

2.1.2 Frequency Dependence of Attenuation Coefficient

As it was mentioned in section 2.1.1, attenuation accounts for the effects of both absorption and scattering. A variety of experimental techniques have been used for attenuation measurement, and determination of the frequency dependence of attenuation of biological tissues. Figure 2-2 is a compilation of the results from many different attenuation measurement experiments under a variety of experimental conditions (Bamber, 1998). The results have mostly been obtained through *ex vivo* experiments. For some specimens, there may be significant differences between the characteristics that are obtained through *ex vivo* experiments and those that are obtained through *in vivo* experiments. These differences are due to biological and physiological factors such as blood flow. In addition, some variations can also be attributed to

different specimen preparation techniques, and the conditions under which the specimens are stored. Attenuation measurement data obtained from soft biological tissues and other similar media indicate that the attenuation coefficient is a function of frequency and with good approximation,

$$\alpha(f) = \beta_0 + \beta_1 |f|^y \qquad (2.11)$$

where β_0, referred to as the attenuation intercept, is usually zero, y is a power law exponent that usually lies in the range from 1 to 2, and β_1 is the attenuation factor in $\frac{\mathrm{dB}}{\mathrm{MHz}^y.\mathrm{cm}}$ (Szabo, 2004; Cobbold, 2007). As equation 2.11 suggests, as the frequency of a wave propagating through a medium is increased, the wave loses more of its energy, and in other words its amplitude gets attenuated to a higher extent. Of course, as it was mentioned before, this loss of energy is due to both absorption, and scattering.

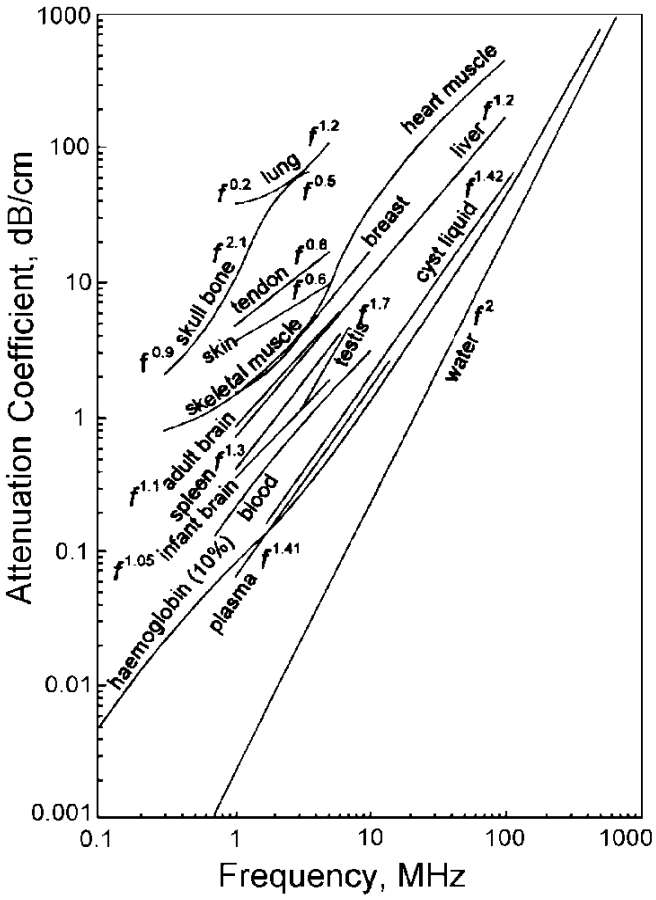

Figure 2-2 Summary of published experimental results for the attenuation vs. frequency characteristics of various biological media and water (Bamber, 1998)

In pure fluids, due to the absence of scatterers, the effect of scattering completely vanishes. As a result, in pure fluids the attenuation and absorption characteristics are identical. In biological tissues, it was initially widely thought that attenuation was entirely due to absorption. However, it was later realized that scattering can significantly contribute to attenuation in biological tissues (Chivers & Hill, 1975; Wells, 1975). Table 2-1 shows relative contributions of absorption and scattering to attenuation for a variety of biological tissues, at different frequencies (Nassiri & Hill, 1986). Data provided in Table 2-1 suggests that at high frequencies the contribution of scattering to attenuation increases. The extent of this increase however varies from tissue to tissue. For example, in the case of fresh human liver, the contribution of scattering to attenuation almost doubles from 12% to 23%, as the frequency is increased from 4MHz to 7MHz. While in the case of fresh skeletal muscle, the contribution of scattering rises only 1%, from 17% to 18%, as the frequency is increased from 4MHz to 7MHz. Bamber (Bamber, 1998) has summarized similar results on relative contributions of scattering and absorption to attenuation for a variety of biological tissues. Overall, at low-MHz frequency ranges, scattering contributes to typically 10-15% of the total value of attenuation for most biological tissues (Bamber, 1998).

Table 2-1 Contributions of scattering to the attenuation coefficient in some biological tissues (Nassiri & Hill, 1986)

Medium	$\mathbf{2\alpha_s [cm^{-1}]}$	$\mathbf{2\alpha\ [cm^{-1}]}$	$\frac{\alpha_s}{\alpha}$	**Frequency**
Fresh human liver	0.09	0.72	12%	4 MHz
Fresh human liver	0.32	1.4	23%	7 MHz
Human blood, Hct = 40%	0.28×10^{-3}	0.17	0.1%	4 MHz
Human blood, Hct = 40%	1.8×10^{-3}	0.37	0.5%	7 MHz
Fresh skeletal muscle	0.16	0.94	17%	4 MHz
Fresh skeletal muscle	0.32	1.8	18%	7 MHz

2.1.3 Linear Approximation of α(f)

Even though α(f) is usually presented as a power law function, it has been shown that attenuation coefficient of soft biological tissues, for practical frequency ranges and bandwidths used in biomedical applications (1 to 20 MHz), increases approximately linearly with frequency. Thus, the slope is approximately constant over practical bandwidths (Ophir, et al., 1984). This approximation relies on a Taylor series expansion about the center frequency f_c of attenuation coefficient exhibiting an arbitrary monotonic increase with frequency as follows (Ophir, et al., 1984),

$$\alpha(f) \approx \alpha(f_c) + \frac{\partial \alpha}{\partial f}\Big|_{f=f_c} \cdot (f - f_c) + \frac{\partial^2 \alpha}{\partial f^2}\Big|_{f=f_c} \cdot \frac{(f-f_c)^2}{2!} + \ \ldots \qquad (2.12)$$

The slope of attenuation is simply the first nonzero term in the frequency derivative of the Taylor series expansion,

$$\frac{d\alpha}{df} \approx \text{zero} + \text{least squares slope} + \text{higher order terms} \qquad (2.13)$$

For practical bandwidths of a few MHz the contributions of the higher order terms of the derivative of the Taylor series expansion are considered insignificant. Thus, the least squares slope is potentially a very useful index quite independent of whether or not tissue attenuation exhibits a linear dependence on frequency over a long range of frequency (Bush, et al., 1993; Ophir et al., 1984).

It should be noted that in this context, "linear" means that attenuation coefficient is proportional to frequency to the first power, and "non-linear" means attenuation coefficient is not proportional to frequency to the first power. Throughout this study, the simplifying assumption is made that the frequency dependent attenuation coefficient, α(f) increases linearly with frequency (Zhang, et al., 2009; Ophir, et al., 1984), with least squares attenuation slope β,

$$\alpha(f) = \alpha_0 + \beta(f - f_c) \qquad (2.14)$$

where α_0 is the attenuation coefficient in $\frac{dB}{cm}$ at the center frequency f_c of the transmitted pulse, and β is the least squares attenuation slope in $\frac{dB}{MHz.cm}$ over the bandwidth of the transmitted pulse. Parameters α_0 and β are usually referred to as attenuation intercept and attenuation slope, respectively (Bush, et al., 1993).

2.2 Insertion-Loss Method for Attenuation Measurement

The insertion-loss method for attenuation measurement in its essence is based on the equation 2.10. As represented in Figure 2-3, in the insertion-loss method, an ultrasound source transmits a planar narrow-band ultrasound wave with frequency f, incident on a given specimen, and a receiver detects the transmitted ultrasound wave propagating in the direction of incidence out of the specimen (Bush, et al., 1993; Cobbold, 2007). The assumption is that the measurement process is taking place in a medium that has zero attenuation, and the only source of attenuation is the specimen under measurement. In addition, it is assumed that the specimen is perfectly matched to the surrounding medium to eliminate the losses associated with reflection, and refraction at the medium-specimen, and specimen-medium boundaries. Initially, the source transmits the ultrasound wave without the specimen being present in the path of the incident wave, between the source (transmitter) and the receiver (detector). Given the assumption that the medium has zero attenuation, the amplitude of the signal that the receiver detects is the peak pressure $p_0(0)$. Then, the specimen is placed in the path of the incident wave, and this time the amplitude of the receiver signal is $p_0(x)$, where x represents the thickness of the specimen under measurement. Substitution of all these parameters back into equation 2.10 yields attenuation, α_{dB} of the specimen at frequency f. The same process can be repeated over a range of frequencies, thereby generating a set of points, $\alpha_{dB}(f)$, for determining the frequency dependence of the attenuation coefficient of the specimen (Cobbold, 2007).

Attenuation coefficient has so far been defined in terms of the relative contributions of absorption and scattering on an incident plane wave. Consequently, in an ideal scenario, attenuation measurement must be conducted using waves that closely approximate the behavior of plane waves. Generating plane waves may prove to be rather difficult. If so, then the non-planar diffractive characteristics of the ultrasound field must be accounted for (Cobbold, 2007).

Aside from the non-planar filed characteristics, there are many other difficulties associated with attenuation measurement and even more difficulties associated with determining the relative contributions of scattering and absorption to attenuation. For example, as it was shown in Figure 2-1, even in the presence of an ideal incident plane wave and perfect impedance matching to the specimen, the transmitted wave will always include a portion of the scattered field (forward

scattered field). To resolve this issue, usually a small transducer aperture that is placed far away is utilized at the receiving end. This significantly reduces the contribution of the forward scattered field (Cobbold, 2007).

Even though it is usually assumed that there is a perfect impedance matching between the specimen and the surrounding medium, in practice it is very difficult to achieve perfect impedance matching. Instead of trying to match the specimen and the surrounding medium, the reflection losses at the medium-specimen and specimen-medium boundaries can be eliminated by considering and using pressure waves propagating out of two separate specimens, in two separate cases. While the two specimens are always made up of the same material, they have different thicknesses. Figure 2-3 illustrates this technique.

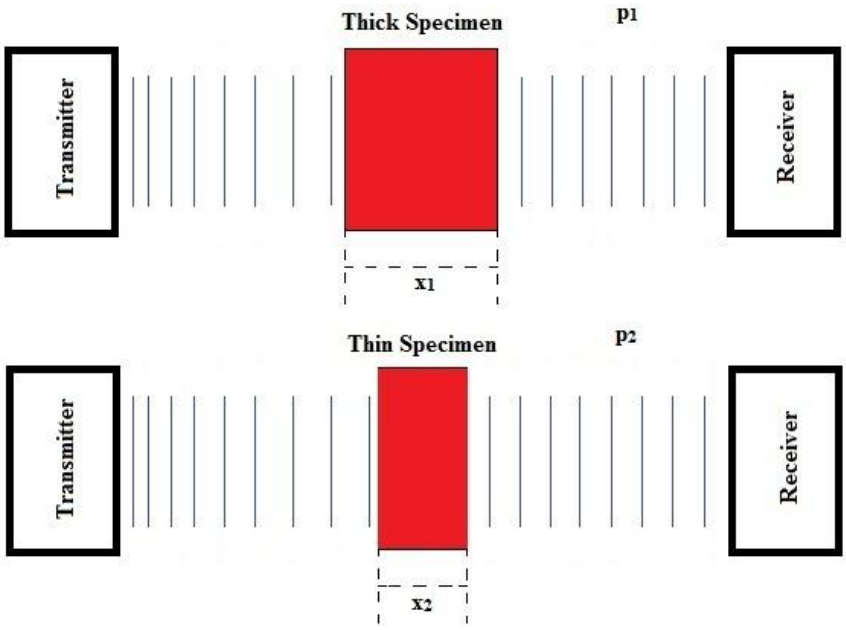

Figure 2-3 Schematic of acoustic attenuation measurement using the insertion-loss technique

As shown in Figure 2-3, the pressure amplitude of the wave propagating out of specimen 1 is denoted as p_1, and the pressure amplitude of the wave propagating out of specimen 2 is denoted as p_2. x_1 and x_2 represent the thicknesses of specimens 1 and 2, respectively, such that $x_1 > x_2$, and $\Delta x = |x_1 - x_2|$ represents the difference in thicknesses of the two specimens. Using these

parameters the attenuation of the specimen at frequency f can be calculated using the following equation,

$$\alpha(f)_{dB} = \frac{-20}{\Delta x}\log\frac{P_1}{P_2} \quad (2.15)$$

thus eliminating the contribution of the transmission and reflection coefficients in both p_1 and p_2. Finally, usually either a long single-frequency tone burst or a wide bandwidth pulse is used. In the case of the broadband pulse, the frequency spectra of the incident and the transmitted pulse waveforms are obtained and utilized to determine the frequency dependence of the attenuation coefficient over a range of frequencies. In the case of the long single-frequency tone burst, the experiments are conducted over a range of frequencies and for every value of frequency, f, equation 2.15 is employed. Earlier publications (Bamber & Hil, 1979; Chivers & Hill, 1975) have thoroughly reviewed the pros and cons associated with each method. More specifically, they have provided a lot of details with regards to sources of error and validations of different methodologies. In this study the insertion-loss method using long single-frequency tone bursts generated at different frequencies were employed to conduct attenuation measurements.

2.2.1 Insertion-Loss Attenuation Measurement Setup

The setup consists of two identical single element ultrasound transducers. To conduct measurements using the insertion-loss method, an attenuation measurement setup based on the schematic shown in Figure 2-4 was employed. Figure 2-5 shows the actual measurement setup that was employed in the laboratory. The two identical single element transducers were aligned along a common axis, 20 cm apart from each other in a water tank.

In order to measure the thicknesses of different specimens, a pulser-receiver was used to excite the transmitting transducer, and the same transducer was used to receive the echo signals. The echo signals were displayed and recorded using the oscilloscope. While measuring attenuation, instead of using the pulser receiver, a function generator was used to excite the transmitting transducer (the source) to generate 30-cycle bursts of ultrasound beams at various frequencies. Each sample was placed at the common foci of the two transducers. The receiving transducer received the ultrasound pressure wave propagating out of the sample, and the received signal was

converted and displayed on an oscilloscope. The trigger signal generated by the function generator at the beginning of each burst was connected to the trigger input of the oscilloscope. This ensured that oscilloscope would start reading the signal from the receiver right after the transmission of the wave.

Finally, degassed, deionized water was used as the surrounding medium. The experiment was conducted over a bandwidth of 3 MHz, from 3 MHz to 6 MHz. As Figure 2-2 illustrates, attenuation coefficient of water exponentially increases as function of frequency. Thus, in the frequency range that was used (3-6 MHz) the maximum value of attenuation coefficient was the attenuation coefficient at 6 MHz. According to Figure 2-2, attenuation coefficient of water at 6 MHz is 0.08 $\frac{\text{dB}}{\text{cm}}$. Since the ultrasound wave traveled a path of 20 cm to reach the receiving transducer, the total attenuation due to water would be 1.6 dB. Although this value was small, for measurement purposes it could not be ignored. However, given the relative nature of attenuation measurement in the insertion-loss technique, the contribution of water (surrounding medium), to attenuation of the ultrasound pressure waves was eliminated when dividing p_1 by p_2.

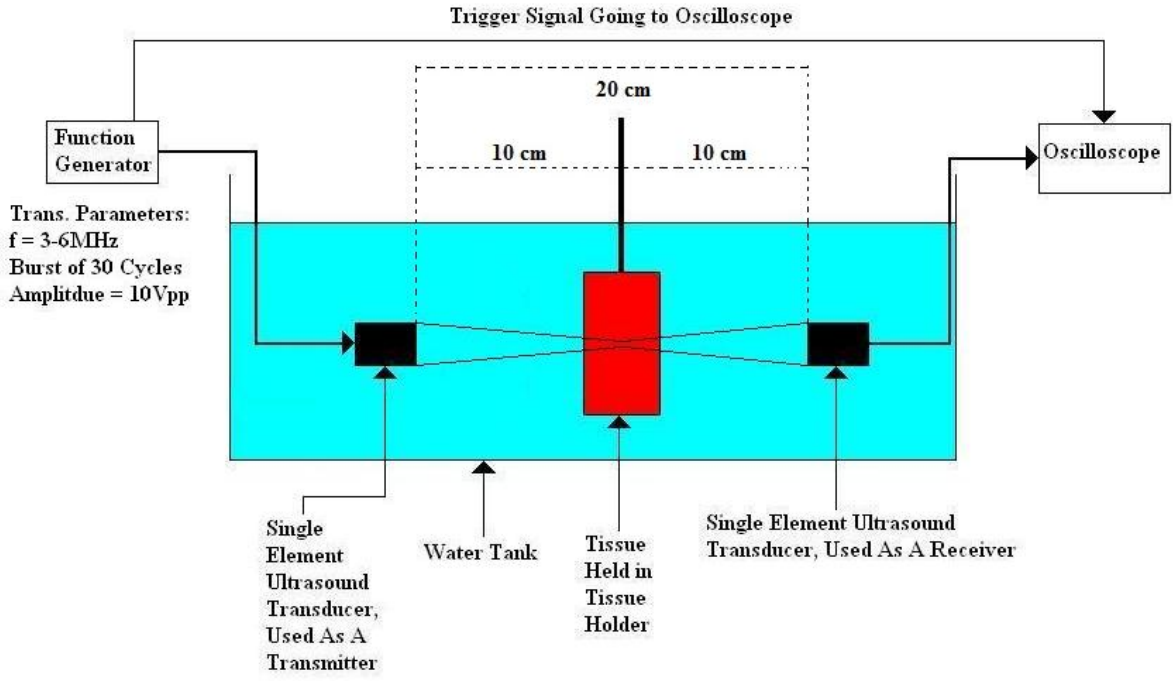

Figure 2-4 Schematic of acoustic attenuation measurement setup using the insertion-loss method

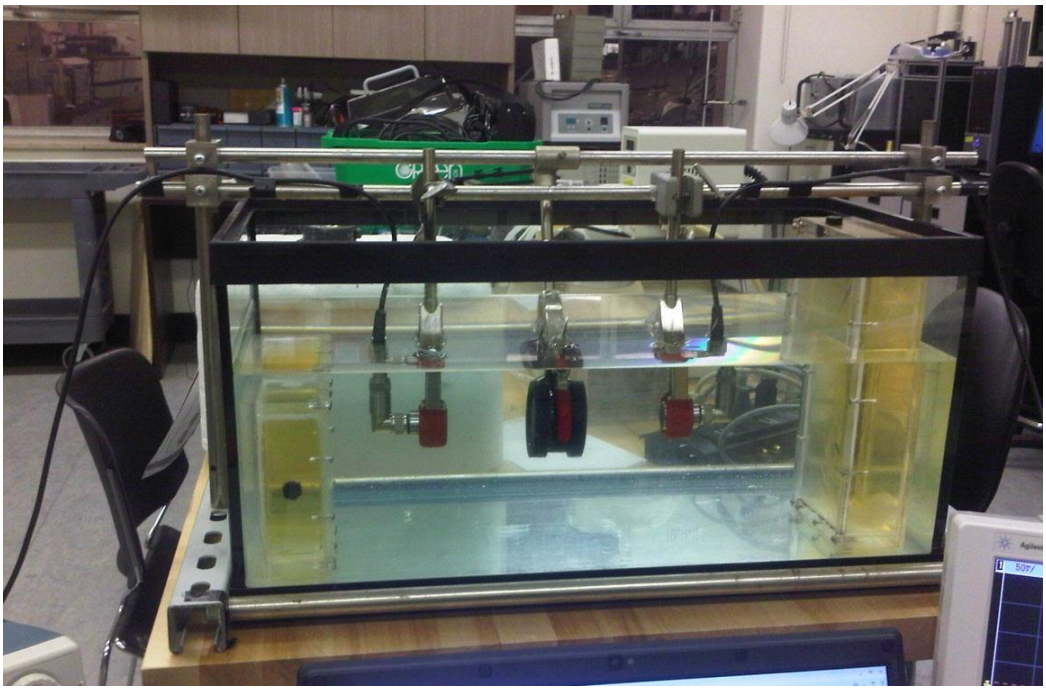

Figure 2-5 Insertion-loss acoustic attenuation measurement setup

The details associated with the main components of the attenuation measurement setup are covered in the following subsections.

2.2.1.1 Function Generator

The signal driving the single element ultrasound transducers was generated by an arbitrary digital function generator (Model AFG3010; Tektronix, Beaverton, OR, USA)

2.2.1.2 Oscilloscope

The received signal detected by the single element ultrasound transducers was displayed and recorded by a 350 MHz digital oscilloscope (Model 7032A; Agilent Technologies, Santa Clara, CA, USA).

2.2.1.3 Pulser-Receiver

In order to drive the single element ultrasound transducers for the purpose of measuring the thicknesses of the specimens, and generating the point spread function (PSF) of the single element ultrasound transducers, a pulser-receiver (Model 5077PR; Olympus NDT, Waltham, MA, USA) was used. The pulser-receiver was capable of generating very high amplitude broadband pulses over a range of center frequencies, and pulse repetition rates.

2.2.1.4 Single Element Ultrasound Transducers

Two identical single element ultrasound transducers (Model V308; Olympus NDT, Waltham, MA, USA) with approximate center frequencies of 5 MHz were used throughout this study. The transducers had aperture diameters of approximately 20 mm, and geometric focal lengths (radius of curvature) of 100 mm. In addition to manufacturer's data, the transducers were characterized by conducting laboratory experiments and computer simulations. The computer simulations were conducted using the simulation software called LATS (Linear Acoustic and Temperature Simulation) developed by our own research group (Butt & Tavakkoli, 2011; Butt, Abhari, & Tavakkoli, 2011; Butt F. , 2011). Some of the details related to LATS are further discussed in section 2.8.

In order to obtain the experimental data under laboratory conditions, the transducers were driven using the pulser-receiver, and the echoed signals were displayed, analyzed, and recorded on the oscilloscope. To generate the echoed signals, the tip of an iron pin with a diameter of 300 μm was placed at the focal points of the transducers. In order to accurately locate the focal point of each transducer, the iron pin was initially placed somewhere in the focal region. The transducer was then continuously excited using the pulser-receiver, while the iron pin was moved around the focal region until an echoed pulse with the maximum amplitude was detected on the oscilloscope. After locating the focal points, the transducers were again excited using the pulser-receiver at their optimum resonant frequencies. The echoed pulses were displayed and recorded on the oscilloscope at a sampling frequency of 200 MHz. Finally, the digitized signals were analyzed, and the frequency impulse responses of the transducers were obtained by taking the Fourier transfers of each of echoed pulses, corresponding to the particular transducer. It should

be noted that the same method was employed by the manufacturer. However, instead of a 300 μm iron pin, a steel ball with a diameter of 2 cm was used. The substantially smaller diameter of the scatterer (the iron pin) used in our experiment ensured a more unidirectional response from the backscattered pulse (Cobbold, 2007).

2.2.2 Insertion-Loss Attenuation Measurement Procedure

In this study, the following procedure was followed for measuring the attenuation coefficient of different specimens.

1. As shown in Figure 2-4, and Figure 2-5, the specimen (tissue or phantom) under measurement was initially prepared and placed on the common axis of both transducers, at a distance of 10 cm (equal to the focal length of both transducers) from both transducers (transmitter and the receiver).
2. Using the pulser-receiver the transmitting transducer (source) sent a single pulse at its center frequency, f_c, and the echo signal received by the same transducer was displayed and recorded by the oscilloscope. By calculating the distance between the two echoes at the water-specimen, and specimen-water boundaries, the initial thickness of the specimen was measured and recorded as x_1 in cm.
3. After determining the thickness of the specimen under study, the pulser-receiver was disconnected from the transducer, and instead the function generator was connected to it. The transmitter sent out bursts of 30 cycles at frequencies in the range of f = 3-6MHz, at step sizes of, Δf = 0.1MHz. The average value of the amplitude of the received burst on the receiving transducer was recorded for each frequency value. These amplitude values represented a set of initial amplitude values denoted by $A(f)_1$ in V, for all values of frequency f = {3.1, 3.2, …, 5.9, 6} in MHz.
4. The role of the two transducers was switched by turning the transmitter into a receiver and turning the receiver into a transmitter.
5. Steps 2-3 were repeated.
6. The values of x_1, and $A(f)_1$ obtained during the two trials, were averaged and denoted by $\bar{x}_1$ and $\overline{A(f)_1}$.
7. The original specimen was replaced by an identical piece of specimen, only with a smaller thickness.
8. Steps 1-6 were conducted again using the thin specimen, and $\bar{x}_2$ and $\overline{A(f)_2}$ were obtained.
9. The attenuation of the tissue was calculated in $\frac{\text{dB}}{\text{cm}}$ using the formula,

$$\alpha(f) = \left(\frac{1}{\bar{x}_1 - \bar{x}_2}\right) \times \left(-20 \log_{10}\left(\frac{\overline{A(f)_1}}{\overline{A(f)_2}}\right)\right) \quad (2.16)$$

It should be noted that the attenuation could also be calculated in $\frac{Np}{cm}$ using the formula,

$$\alpha(f) = \left(\frac{1}{\bar{x}_1 - \bar{x}_2}\right) \times \left(-\ln\left(\frac{\overline{A(f)_1}}{\overline{A(f)_2}}\right)\right) \quad (2.17)$$

However, the $\frac{dB}{cm}$ version of the formula was utilized in order to avoid conversion from $\frac{Np}{cm}$ to $\frac{dB}{cm}$.

It should be noted that there was no need for conversion of amplitude values from V to Pa, since,

$$\overline{A(f)_1} = C.\overline{p(f)_1} \quad (2.18)$$

and,

$$\overline{A(f)_2} = C.\overline{p(f)_2} \quad (2.19)$$

Where, C was a constant in $\frac{V}{Pa}$, dependent on the characteristics of the transducer crystal, and p(f) was pressure amplitude values at different frequencies over the range of f = 3-6MHz. Therefore,

$$\frac{\overline{A(f)_1}}{\overline{A(f)_2}} = \frac{C.\overline{p(f)_1}}{C.\overline{p(f)_2}} = \frac{\overline{p(f)_1}}{\overline{p(f)_2}} \quad (2.20)$$

10. Based on the linear approximation of α(f) presented in equation 2.14, a straight line was fitted to α(f) over f = 3-6MHz, resulting in, $\alpha(f) = \alpha_0 + \beta.f$. Where, α_0 was the attenuation coefficient in $\frac{dB}{cm}$ at the center frequency f_c of the transmitted pulse, and β was the least squares attenuation slope in $\frac{dB}{MHz.cm}$ over the frequency range of f = 3-6MHz.As it was mentioned before, α_0 was referred to as the attenuation intercept, and β was referred to as the attenuation slope.

2.2.3 Construction of PVCP Attenuation Phantoms

To ensure the accuracy of the measurements, the attenuation measurement setup had to be tested using samples of known attenuation coefficients, usually referred to as attenuation phantoms. PVCP (Polyvinyl Chloride Plastisol, MF manufacturing Co., Fort Worth, Texas, USA) solid attenuation phantoms were used for this study (Spirou, et al., 2005).

PVCP itself is a non-toxic, white opaque material, which is insoluble in water. It is homogeneous and can be stored for an extended period of time without any degradation in its properties. At the time of this study, a set of ten PVCP attenuation phantoms had already been constructed for a previous research project (Soleimankhani, 2007). Therefore, the same set of phantoms was used for this study.

In order to build attenuation phantoms out of PVCP, the PVCP stock solution is heated to 200˚C. As the stock solution reaches a temperature of 200˚C, it is continuously stirred in order to avoid the formation of air bubbles within the solution. Air bubbles strongly attenuate ultrasound, and they introduce inhomogeneity to the phantom. Consequently, a lot of care must be given in order to prevent the formation of these air bubbles. As the heating process continues, the white opaque plastic solution turns to a translucent yellowish color. At this point the solution is ready and can be poured into the desired mold and must be given enough time to cool down. In order to produce this set of phantoms, PVC (polyvinyl chloride) pipes were cut into specific lengths, and used as molds (Soleimankhani, 2007). Each PVC pipe was clamped between two pieces of glass, and the heated PVCP solution was poured into each PVC pipe (mold) through holes that were drilled into the PVC pipes. As the solution cooled down, the phantoms solidified and were ready to be used in direct contact with water, and other similar surrounding mediums. Figure 2-6 illustrates this set of attenuation phantoms. Table 2-2 lists the phantoms along with their respective thicknesses.

Table 2-2 PVCP Phantom Thickness Estimation

Phantom	Thickness (cm)
Phantom A	0.52 ± 0.05
Phantom B	1.17 ± 0.05
Phantom C	1.71 ± 0.05
Phantom D	2.42 ± 0.05
Phantom E	3.07 ± 0.05
Phantom F	3.72 ± 0.05
Phantom G	4.30 ± 0.05
Phantom H	4.93 ± 0.05
Phantom I	5.45 ± 0.05
Phantom J	6.30 ± 0.05

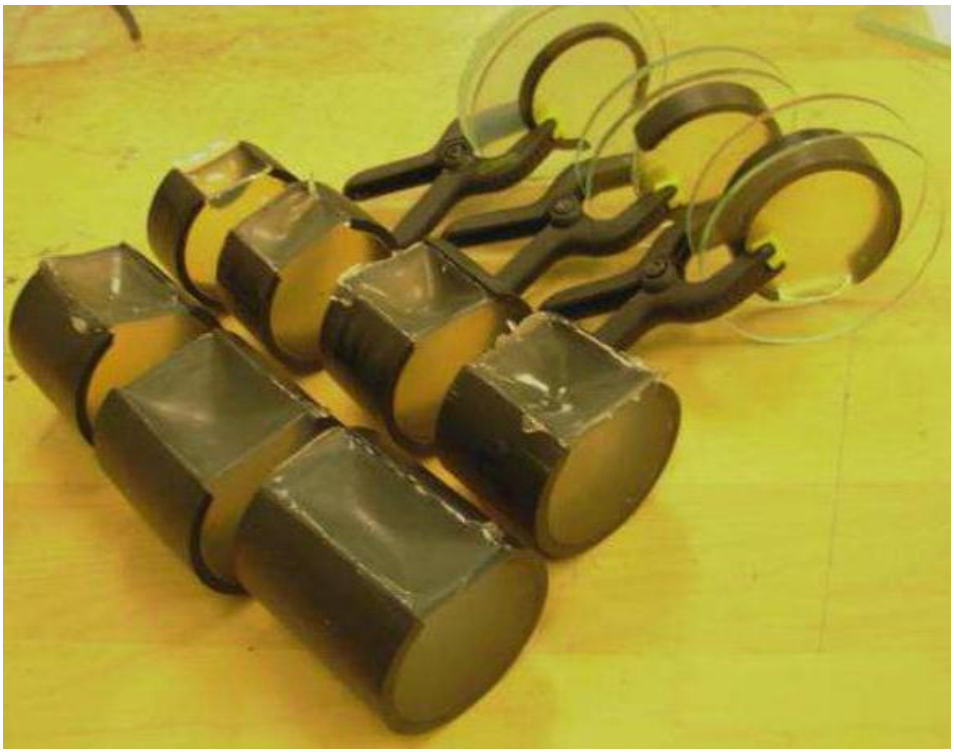

Figure 2-6 A set of 10 PVCP tissue-mimicking phantoms, which corresponds to the phantoms listed in Table 2-2

2.2.4 Insertion-Loss Attenuation Measurement on PVCP Phantoms

The procedure outlined in subsection 2.2.2 for attenuation measurement using the insertion-loss technique was followed to measure the acoustic attenuation of the PVCP phantoms. The only variation was that instead of determining the thicknesses of the phantoms ultrasonically as it was outlined in step 2 of the procedure, given the symmetric and solid nature of the phantoms, the measured thickness values listed in Table 2-2 were used, and step 2 was skipped. Given the large number of attenuation phantoms there were many different combinations of phantoms that could be used in pairs, with one phantom representing the thick specimen, and the other phantom representing the thin specimen. For this study, the attenuation phantoms were utilized in the combinations listed in Table 2-3.

Table 2-3 List of pairs of PVCP attenuation phantoms used in attenuation measurement

Combination	Pair of PVCP Phantoms Used	x_1 (cm)	x_2 (cm)	Δx (cm)
1	{A, B}	1.17 ± 0.05	0.52 ± 0.05	0.65
2	{B, C}	1.71 ± 0.05	1.17 ± 0.05	0.54
3	{C, D}	2.42 ± 0.05	1.71 ± 0.05	0.71
4	{D, E}	3.07 ± 0.05	2.42 ± 0.05	0.65
5	{E, F}	3.72 ± 0.05	3.07 ± 0.05	0.65
6	{F, G}	4.30 ± 0.05	3.72 ± 0.05	0.58
7	{G, H}	4.93 ± 0.05	4.30 ± 0.05	0.63
8	{H, I}	5.45 ± 0.05	4.93 ± 0.05	0.52
9	{I, J}	6.30 ± 0.05	5.45 ± 0.05	0.85

As it was mentioned before, the while measuring attenuation, the role of the transmitter and receiver were switched between the two single element ultrasound transducers, resulting two sets of data for each combination. Based on the total number of combinations, there were a total of 18 data samples for attenuation coefficient at each frequency.

2.2.5 Insertion-Loss Attenuation Measurement on Normal *Ex vivo* Porcine Muscle Tissue

Normal (non-coagulated) fresh porcine muscle tissues were acquired from a local grocery store. Before measurement, the tissue specimens were cut and trimmed to 20×80×100 mm pieces, and stored in degassed, deionized water at 5˚C for 12 hours. This ensured that some of the preexisting gas bubbles were transferred from the tissue into the degassed water. The specimens were then mounted on the tissue holder for measurement. The procedure outlined in subsection 2.2.2 was exactly followed to measure the acoustic attenuation of normal *ex vivo* porcine muscle tissues. To generate pairs of tissues with different thicknesses, initially the prepared tissue would be mounted and used for measurement. Then the same piece of tissue would be cut through its cross section, generating two pieces of tissues with thicknesses approximately half the thickness of the original tissue, representing the thin specimens.

2.2.6 Insertion-Loss Attenuation Measurement on Fully Coagulated *Ex vivo* Porcine Muscle Tissue

Before measurement, normal muscle specimens were cut and trimmed to 20×80×100 mm pieces. These specimens were then kept in boiling water for 30 minutes at 100˚C. This ensured that the muscle samples were fully and uniformly coagulated. Then, just as in the case of normal samples, the coagulated samples were stored in degassed, deionized water at 5˚C for 12 hours, with the rest of the procedure being exactly the same as in subsection 2.2.5.

2.3 Theoretical Basis of Attenuation Estimation Using Backscattered Ultrasound RF Signal

2.3.1 Material Transfer Function (MTF)

All the details associated with attenuation were already discussed in the previous sections. As it was mentioned, attenuation is a frequency dependent loss. In addition to

attenuation, the phase velocity of tissue is frequency dependent and therefore also varies with frequency (Szabo, 2004),

$$c(f) = c_0 + \Delta c(f) \tag{2.21}$$

where $\Delta c(f)$ is a small change in sound speed. This change of phase velocity with frequency is required by causality. Although this velocity dispersion is small, the effect of this small velocity dispersion on broadband pulses can be rather significant (Szabo, 2004). Equation 2.21 can be rearranged in the following format,

$$\Delta c(f) = c(f) - c_0 \tag{2.22}$$

Based on equation 2.22, the change in sound speed can be plotted as a function of frequency dependent sound speed, and a baseline value. Figure 2-7 illustrates phase velocity dispersion change by plotting the phase velocity dispersion minus a baseline phase velocity value at 5 MHz for different types of soft biological tissues (Szabo, 2004).

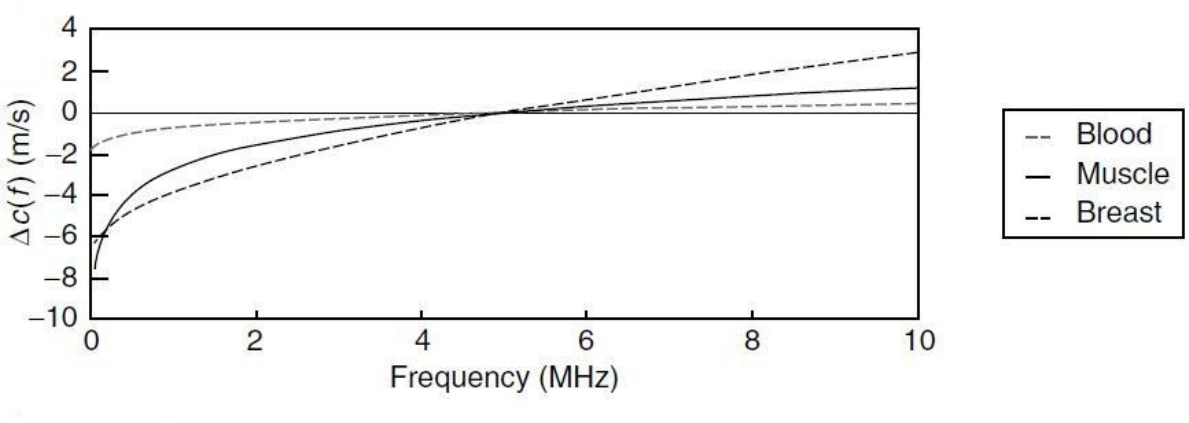

Figure 2-7 Frequency dependent phase velocity minus a baseline phase velocity value at 5MHz for different tissues (Szabo, 2004)

Bandwidths employed throughout this study were relatively narrow (≈3 MHz). As a result, the effect of velocity dispersion was not very significant. The combined effects of absorption loss (α_a) and dispersion on pulse propagation in a lossy medium is described by the following material transfer function in the frequency domain (Szabo, 2004):

$$\mathrm{MTF}(f, z) = \exp[\gamma_T(f) z] \tag{2.23}$$

where,

$$\gamma_T(f) = -\alpha_a(f) - i\delta(f) \tag{2.24}$$

where, α_a is the frequency dependent absorption loss and,

$$\delta(f) = k_0(f) + \delta_E(f) \tag{2.25}$$

where, k_0 is the baseline wave number which is equal to $\frac{\omega}{c_0}$, c_0 is the sound speed at the center frequency of the spectrum of the pulse, and $\delta_E(f)$ is an excess dispersion term required by causality.

The MTF's time domain counterpart is called the material impulse response function, mirf(t,z),

$$\text{mirf}(t,z) = \mathbf{F^{-1}}\{\exp[\gamma_T(f)z]\} \tag{2.26}$$

where $\mathbf{F^{-1}}$ is the inverse Fourier transform operator. In time domain, for an initial pulse $p_0(t)$, the pulse p(t, z) propagating in a medium, at time t and a distance z can be described by,

$$p(t,z) = p_0(t) * \text{mirf}(t,z) \tag{2.27}$$

Taking the Fourier transfer of both sides of equation 2.27 results in the following equation in frequency domain,

$$P(f,z) = P_0(f)\text{MTF}(f,z) \tag{2.28}$$

2.3.2 The Material Transfer Function in Pulse-Echo Imaging

In order for the material transfer function (MTF) to be employed in pulse-echo ultrasound imaging, the effect of back scattering, and the return path of the transmitted pulse $P_0(f)$ must be included in the MTF. To do that, first the general case is addressed. For the general case of a given pulse $P_0(f)$, propagating in a given material over the paths z_1 and z_2, the total MTF will be, the product of the individual MTF's for each path, resulting in the following,

$$\text{MTF}(f, z_1 + z_2) = \exp[\gamma_T(f)z_1] \times \exp[\gamma_T(f)z_2] \tag{2.29}$$

so,

$$\text{MTF}(f, z_1 + z_2) = \exp[\gamma_T(f)(z_1 + z_2)] \tag{2.30}$$

In the specific case of pulse echo imaging, assuming each echo travels the same distance z back and forth,

$$z_1 = z_2 = z \tag{2.31}$$

so,

$$\mathrm{MTF}(f, z_1 + z_2) = \mathrm{MTF}(f, 2z) \tag{2.32}$$

and,

$$\exp[\gamma_T(f)(z_1 + z_2)] = \exp[\gamma_T(f)(z + z)] = \exp[2.\gamma_T(f).z] \tag{2.33}$$

therefore,

$$\mathrm{MTF}(f, 2z) = \exp[2.\gamma_T(f).z] \tag{2.34}$$

2.3.3 Simplifying Assumptions

To use the material transfer function in estimating changes in attenuation coefficient of a given material (here soft biological tissues), a number of simplifying assumptions had to be made. The material transfer function is a mathematical model describing the propagation of an ultrasound pulse in an absorptive media. Soft biological tissues are indeed examples of absorptive media. However, they are also made up of many scatterers. So, as a simple model, soft biological tissues can be modeled as a group of scatterers (spherical and cylindrical) imbedded in an absorptive medium (Cobbold, 2007). The MTF model given by the equation 2.34 does not take into account the effect of the frequency dependent scattering, α_s. To compensate for this deficiency of the MTF, throughout this study, the simplifying assumption was made that, for any given material, the scattering characteristics of that material always remained constant. More specifically, it was assumed that the scattering properties of any given soft biological tissue remained constant, before, during, and after the HIFU exposure. Going back to equations 2.3-5, in mathematical terms, the frequency dependent attenuation coefficient is described as a linear combination of the frequency dependent scattering coefficient and frequency dependent absorption coefficient,

$$\alpha(f) = \alpha_s(f) + \alpha_a(f) \tag{2.35}$$

By making the assumption that $\alpha_s(f)$ remains constant, then equation 2.34 is reduced to,

$$\alpha(f) = C + \alpha_a(f) \quad (2.36)$$

Equation 2.36 further implies that any change in frequency dependent attenuation coefficient will be equal to change in frequency dependent absorption coefficient. In other words, by estimating the changes in $\alpha_a(f)$, any changes in $\alpha(f)$ can be estimated as well, as given by equations 2.37a-c.

$$\alpha_{initial}(f) = C + \alpha_{a\_initial}(f) \quad (2.37a)$$

$$\alpha_{final}(f) = C + \alpha_{a\_final}(f) \quad (2.37b)$$

subtracting 2.37a from 2.37b,

$$\rightarrow \Delta\alpha(f) = \Delta\alpha_a(f) \quad (2.37c)$$

To estimate $\Delta\alpha(f)$, the real part of $\gamma_T(f)$ of the material transfer function was isolated and treated as the frequency dependent attenuation coefficient, $\alpha(f)$. Furthermore, by estimating $\Delta\alpha(f)$, $\Delta\beta$ and $\Delta\alpha_0$ could be estimated.

Given the negligible contribution of velocity dispersion within the narrow bandwidths used in this study (~3 MHz), the $\delta(f)$ term of $\gamma_T(f)$ was neglected by discarding the imaginary component of $\gamma_T(f)$.

2.4 Estimating Changes in Attenuation of *Ex vivo* Porcine Muscle Tissue as a Function of HIFU Exposure

2.4.1 Experimental Setup

Figure 2-8 illustrates the schematic diagram for the experimental setup. The experiments were conducted on fresh *ex vivo* porcine muscle tissues purchased from a local grocery store. The muscle specimens were cut and trimmed to 20×80×100 mm, and stored in degassed, deionized water at 5˚C for 12 hours prior to conducting the experiment. This ensured that any preexisting gas bubbles were transferred from the tissue into the degassed water. The specimens were then mounted on the tissue holder for HIFU treatment. The HIFU transducer was installed inside a water tank filled with degassed deionized water at room temperature. The tissue in the tissue holder was then submerged in the tank at the focal region such that it would cover the

entire focal area. Enough time was allocated for the tissue inside the water tank to reach room temperature. The imaging probe was installed confocally through a hole at the center of the HIFU transducer to ensure that it was always scanning the focal region of the HIFU transducer on the *xz* plane. Figure 2-9 illustrates the confocal arrangement of the imaging probe and the HIFU transducer.

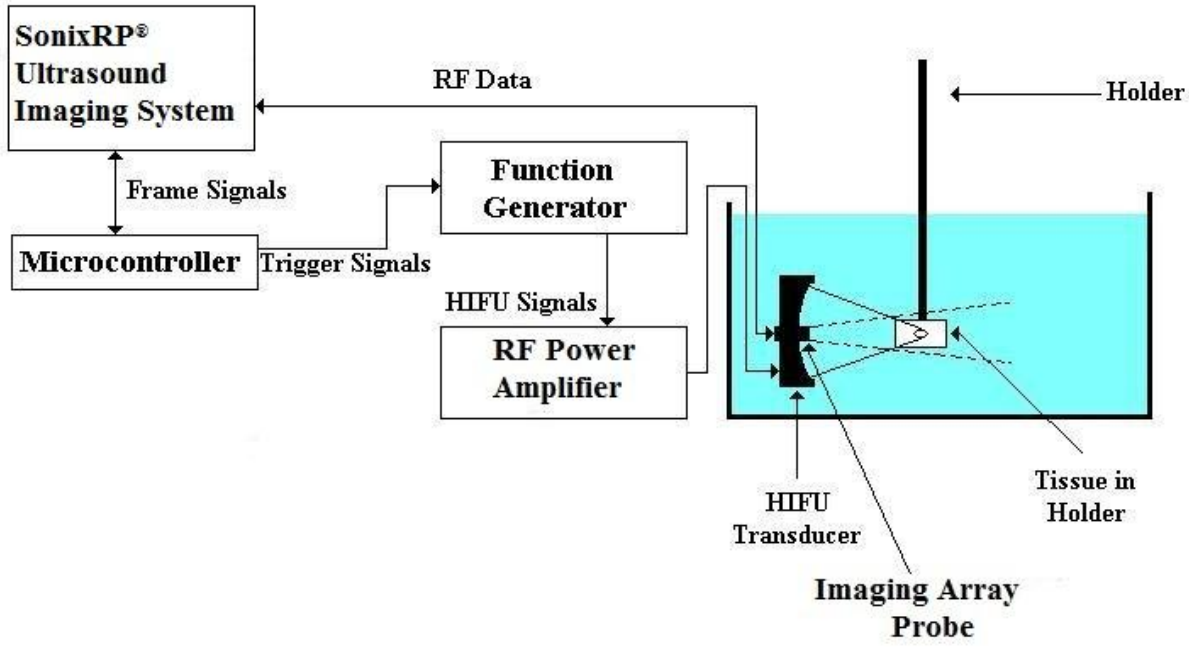

Figure 2-8 Schematic diagram of the image-guided HIFU experimental setup

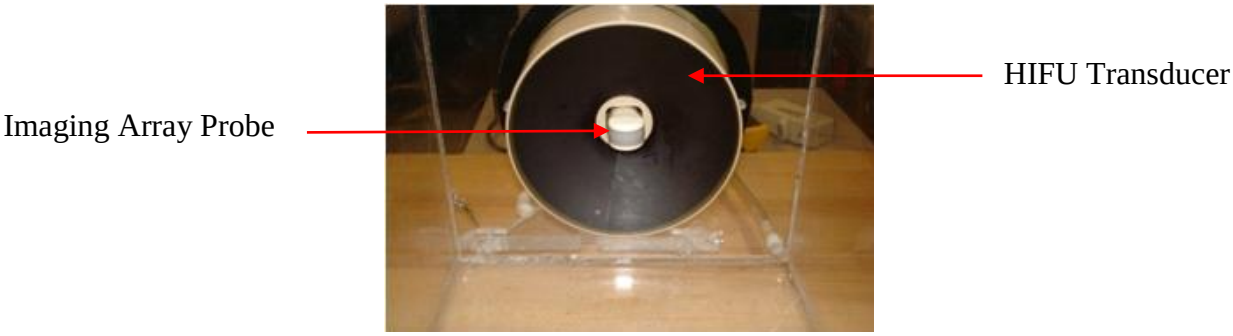

Figure 2-9 The HIFU transducer and the imaging probe in a confocal arrangement

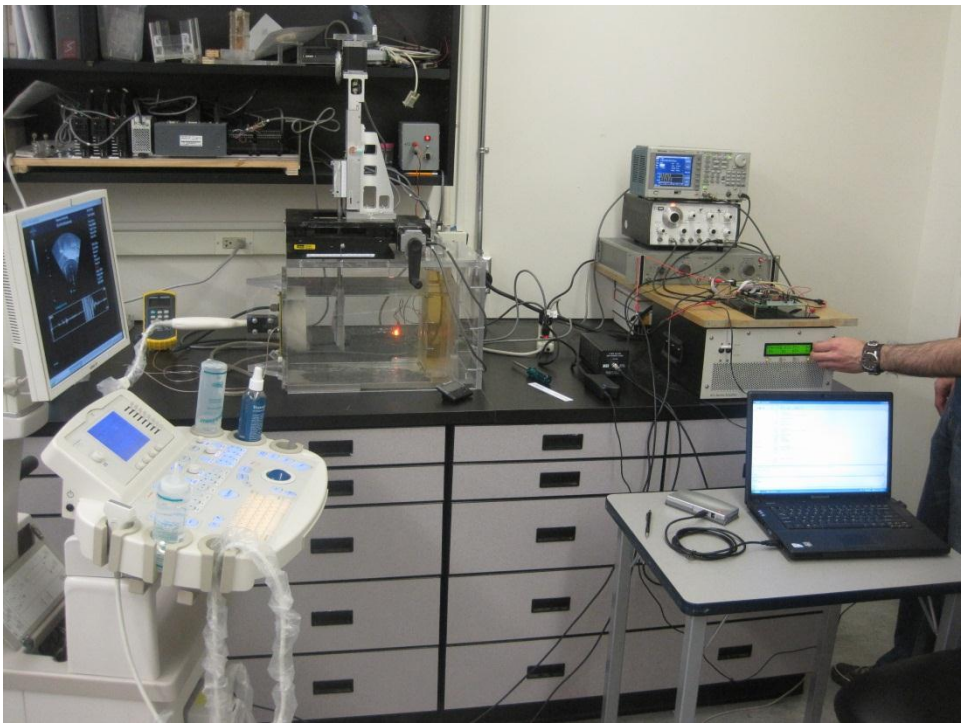

Figure 2-10 The experimental setup in the laboratory

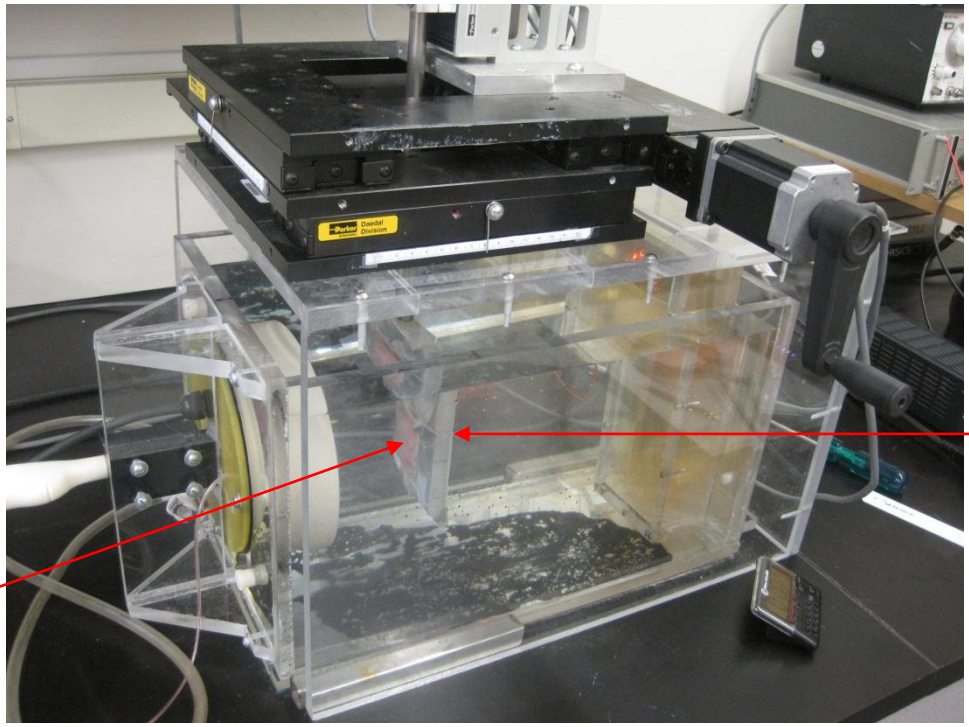

Figure 2-11 Tissue in the tissue-holder submerged in the water tank in front of the HIFU transducer, covering the entire focal region

Figure 2-10 shows the actual setup used in the laboratory. Figure 2-11 shows the tissue in the tissue-holder placed in front of the HIFU transducer. An acoustic absorber is placed at the end of the water tank to absorb acoustic waves, and prevent any reverberations within the water tank.

2.4.1.1 Function Generator

The radio frequency (RF) signal driving the HIFU transducer was generated by an arbitrary function generator (Model AFG3010; Tektronix, Beaverton, OR, USA).

2.4.1.2 RF Power Amplifier

The RF signal was amplified by a class A broadband RF power amplifier (Model A150; E&I, Rochester, NY, USA), with frequency range of 300 kHz-35 MHz, nominal gain of 53 dB, and class A nominal linear electric output power of 150 W. The output signal was transferred to the HIFU transducer throughout a matching network (to maximize the transmitted power).

2.4.1.3 HIFU Transducer

A single element HIFU transducer (Model 6699A101; Imasonic S. A., Voray sur l'Ognon, France) with a resonant frequency of 1 MHz was used throughout this study. The transducer had a 125 mm diameter of aperture, and a 100 mm geometric focal length (radius of curvature). The transducer was calibrated by a needle hydrophone with an active element diameter of 400 μm (Model HNA-0400; ONDA Corporation, Sunnyvale, CA, USA). Figure 2-12 shows the needle hydrophone scanning the acoustic filed of the HIFU transducer at various locations in space. In addition to hydrophone measurements, the acoustic field profile of the HIFU transducer was characterized using computer simulations.

The efficiency of the HIFU transducer was defined as the ratio of the converted acoustic power to the transmitted electric power. The transmitted electric power was measured using an electrical power meter (Bird Power Meter 4021; Bird Technologies Group, Cleveland, OH,

USA). The acoustic power was measured by a radiation force balance unit (Model RFB-2000; ONDA Corporation, Sunnyvale, CA, USA). Figure 2-13 shows the HIFU transducer positioned at the top of the radiation force balance unit.

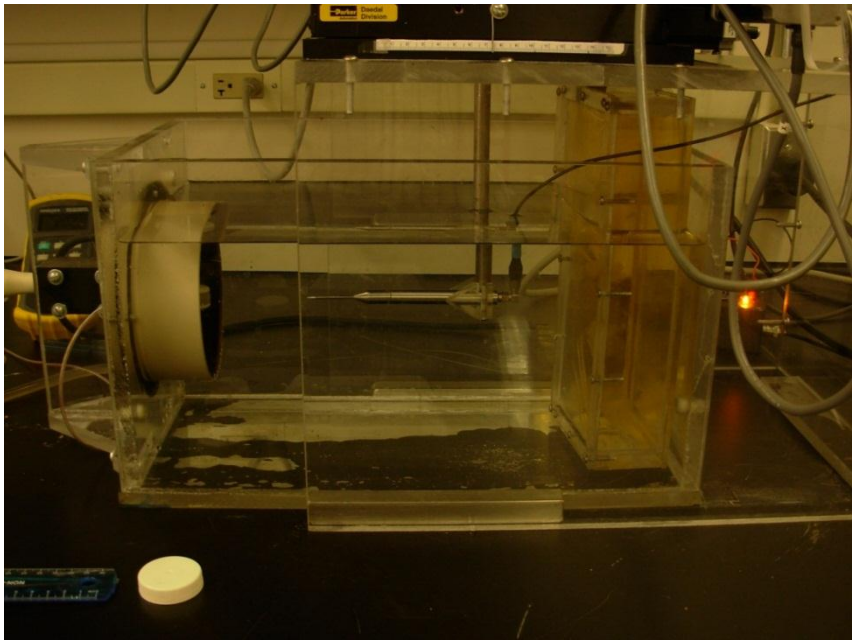

Figure 2-12 Needle hydrophone placed in the acoustic field of the HIFU transducer

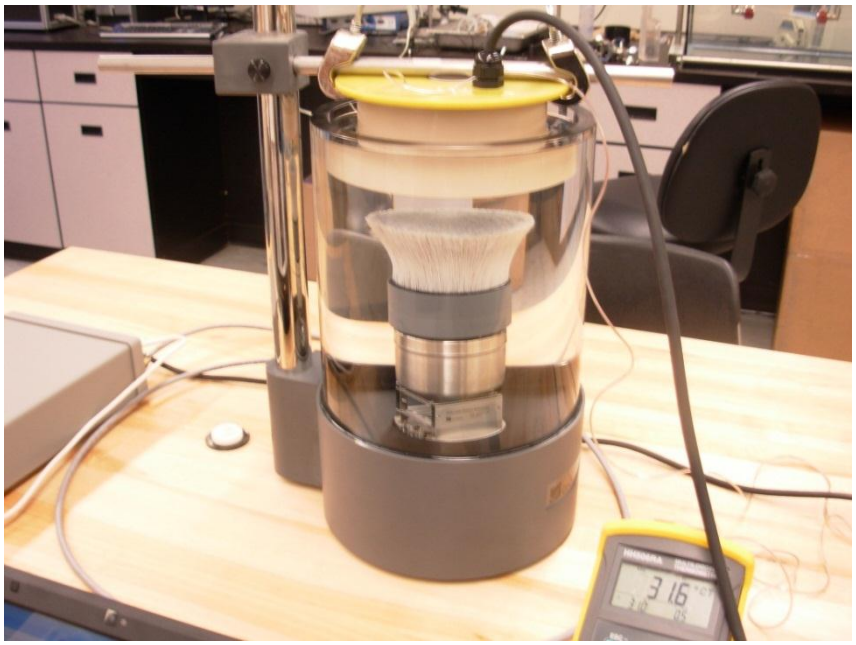

Figure 2-13 The HIFU transducer positioned on top of the radiation force balance

For the HIFU transducer, the free field (in water) spatially averaged intensity, I_{SA}, was estimated using the following equation (Hill, et al., 1994),

$$I_{SA} = 0.867 \frac{P}{D^2} \tag{2.38}$$

Where, P was the total acoustic power measured using the calibrated acoustic power meter at the surface of the transducer and D is the focal beam width at FWHM measured using the calibrated hydrophone.

2.4.1.4 Ultrasound Imaging System

An ultrasound imaging system (SonixRP® scanner, Ultrasonix Inc., Richmond, BC, Canada) and an endocavity array probe (EC9-5/10, Ultrasonix Inc., Richmond, BC, Canada) with 128 elements, a center frequency of 7 MHz, and bandwidth of 3 MHz, were used for acquisition of B-mode images, and RF backscattered data.

2.4.1.5 Micro-Controller

In order to acquire RF backscattered data throughout all phases of treatment, a micro-controller (Model M68HC11; Motorola, Inc., Schaumburg, Illinois, USA) was used. To obtain RF data without any interference, the trigger signals from the ultrasound imaging system were directed to the microcontroller, and the micro-controller in turn, in synchronicity with the ultrasound imaging system, generated its own trigger signals that were in turn directed to the function generator. Upon receiving every trigger signal from the micro-controller, the function generator would generate a burst of sine waves at 1MHz, with specific durations (depending on the duty cycle).

2.4.2 HIFU Exposure and Data Acquisition

RF data frames were acquired before, during, and after HIFU exposure. During HIFU treatment, the RF data frames were obtained by briefly turning off the HIFU transducer in order

to avoid acoustic and electrical interferences (caused by the HIFU transducer) on the acquired RF data frames. The duration of interruption was 120 ms (OFF-Time), for every HIFU ON-Time. The 120 ms interruption allowed the capture of two RF data frames for every HIFU ON-Time. Throughout this study, the HIFU ON-Time was kept constant at 400 ms, resulting in a duty cycle of 77% for HIFU exposures of 40 seconds in total duration. Figure 2-14 illustrates the timeline of HIFU exposure and acquisition of B-mode images, and RF data. A total of 76 RF frames were acquired during every 40 seconds of HIFU exposure.

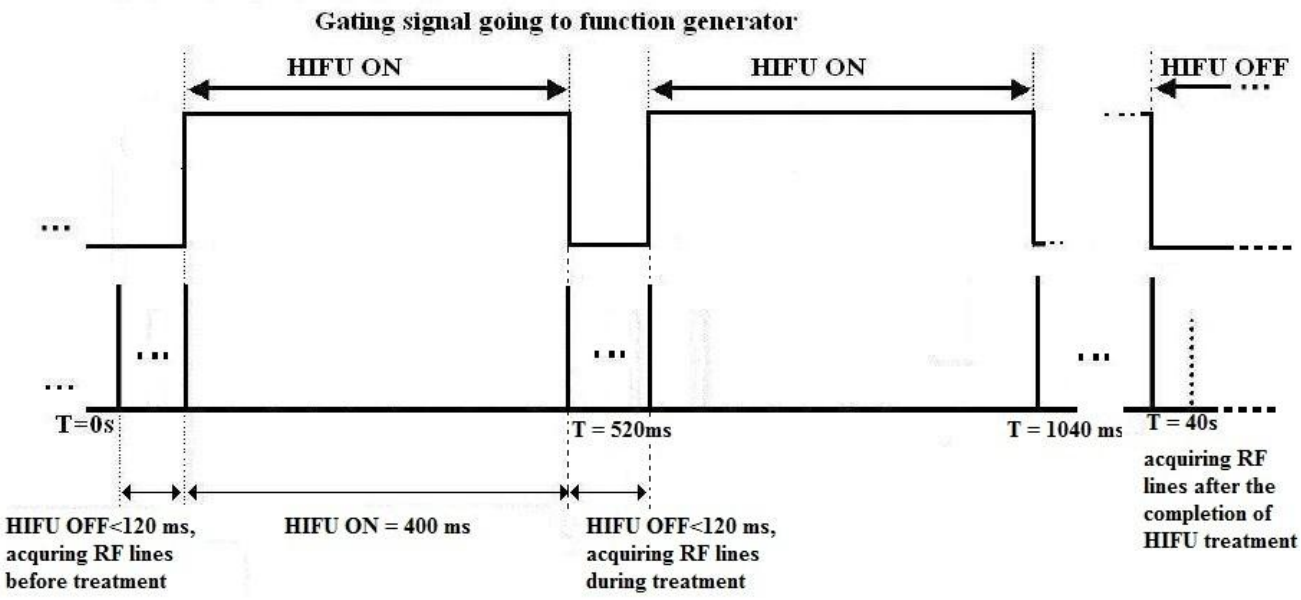

Figure 2-14 Timing diagram of HIFU exposure and data acquisition

The total HIFU treatment time was kept constant at 40 s for input electric powers between 70 W to 100 W. RF data were also acquired before, and after HIFU treatments to estimate the initial and final acoustic properties. RF data were acquired for 10 minutes after the completion of HIFU treatment. In one of the experiments, RF data were acquired overnight, 13 hours after the completion of HIFU treatment as well.

2.5 Estimating Changes in Attenuation Slope (Δβ) Using Backscattered Ultrasound Pulses (Attenuation Slope Algorithm)

Using the linear approximation of the attenuation coefficient, α(f), it is shown in the following that Δβ can be estimated by finding the least squares slope of the line fitted to Δα(f). In other words, based on the linear model (equation 2.14) it can be inferred that the slope of change in attenuation coefficient is equivalent to the change in attenuation slope, Δβ.

As it was explained in section 2.4, using the experimental setup in the laboratory, backscattered ultrasound signals (RF data) were acquired before, during, and after HIFU exposure. As it was explained, the acquired RF data consisted of many individual frames, with each frame in turn consisting of many individual echo lines that were detected by each individual element of the ultrasound imaging transducer array.

The attenuation slope algorithm was implemented to estimate Δβ in $[\frac{\mathrm{dB}}{\mathrm{MHz.cm}}]$ as a function of location in space, with respect to an initial value of β (as a function of space) right before the beginning of HIFU treatment. In order to accomplish that, changes in the least squares slope of the line fitted to Δα(f) were constantly estimated throughout the entire treatment cycle, with respect to a reference frame obtained right before the beginning of HIFU exposure. The algorithm would generate a set of 2D matrices, each representing a map of Δβ values (as a function of time (T), depth (z), and line number), with respect to the reference frame obtained at T_0 (T = 0s).

The following is a mathematical description of the steps taken by the attenuation slope algorithm in order to estimate Δβ for one window of signal with respect to a reference window, at location z, in frequency domain (Szabo, 2004),

$$P(f,z)_{signal} = P_0(f)MTF(f,z) \tag{2.39}$$

$$\ln P(f,z)_{signal} = \ln P_0(f) + \ln \exp[2.\gamma_T(f).z] \tag{2.40a}$$

$$\ln P(f,z)_{signal} = \ln P_0(f) + 2.\gamma_T(f).z \tag{2.40b}$$

$$S_{signal}(f) = -\mathrm{Re}\{\ln P_0(f) + 2.\gamma_T(f).z\} \tag{2.41a}$$

Substituting $\gamma_T(f) = -\alpha(f) - i\delta(f)$ in equation 2.41a yields,

$$S_{signal}(f) = -Re\{\ln P_0(f)\} + 2.\alpha(f)_{signal}.z \quad (2.41b)$$

Similarly, the reference obtained at T_0 (T = 0s) is,

$$S_{reference}(f) = -Re\{\ln P_0(f) + 2.\gamma_T(f).z\} \quad (2.42a)$$

$$S_{reference}(f) = -Re\{\ln P_0(f)\} + 2.\alpha(f)_{reference}.z \quad (2.42b)$$

Figure 2-15 is a graphical representation of the two spectra, $S_{reference}(f)$ and $S_{signal}(f)$ for a typical representative ultrasound RF data acquisition (Ophir, et al., 1984).

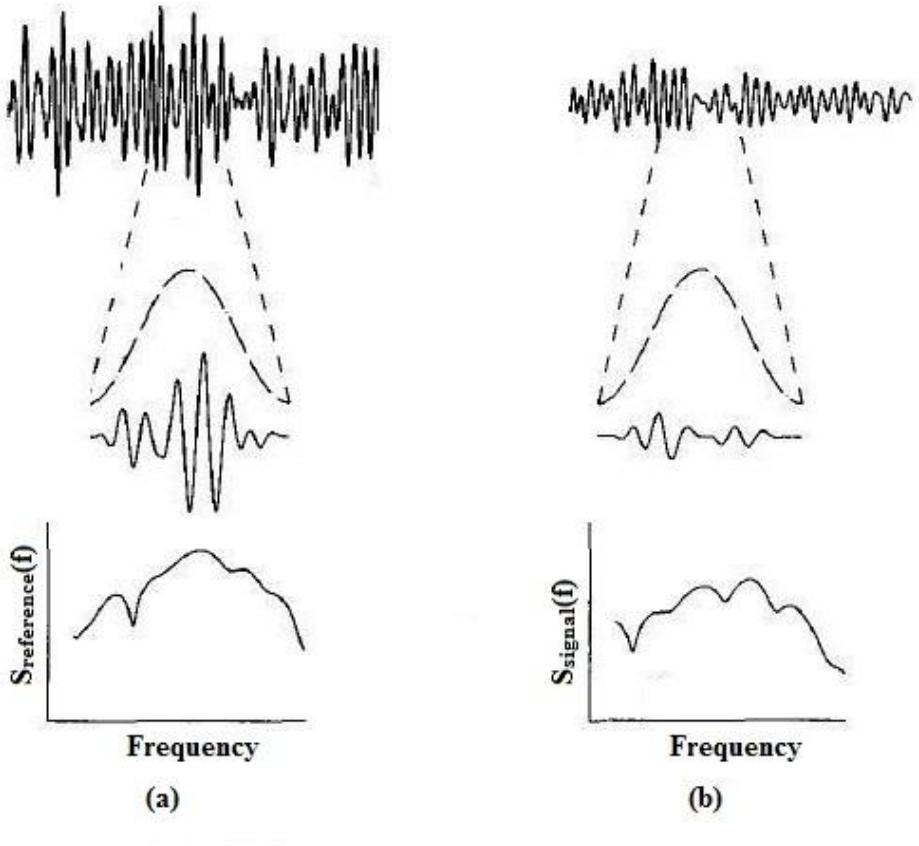

Figure 2-15 (a) $S_{reference}(f)$ vs. (b) $S_{signal}(f)$ (Ophir, et al., 1984)

Subtracting $S_{reference}$ from S_{signal} results in,

$$\Delta S(f) = S_{signal}(f) - S_{reference}(f) \quad (2.43a)$$

$$\Delta S(f) = 2.z.\left(\alpha(f)_{signal} - \alpha(f)_{reference}\right) \quad (2.43b)$$

substituting $\alpha(f) = \alpha_0 + \beta(f - f_c)$,

$$\Delta S(f) = 2.z.(\Delta\alpha_0 + \Delta\beta(f - f_c)) \quad (2.43c)$$

$$\Delta S(f) = 2.z.\Delta\alpha_0 + 2.z.\Delta\beta.(f - f_c) \quad (2.43d)$$

Fitting a line to ΔS(f), and then diving the slope of the fitted line by 2z yields the value of Δβ in $[\frac{Np}{MHz.cm}]$, which is ultimately converted to $[\frac{dB}{MHz.cm}]$. Figure 2-16 illustrates the steps involved in obtaining ΔS(f), and estimating Δβ.

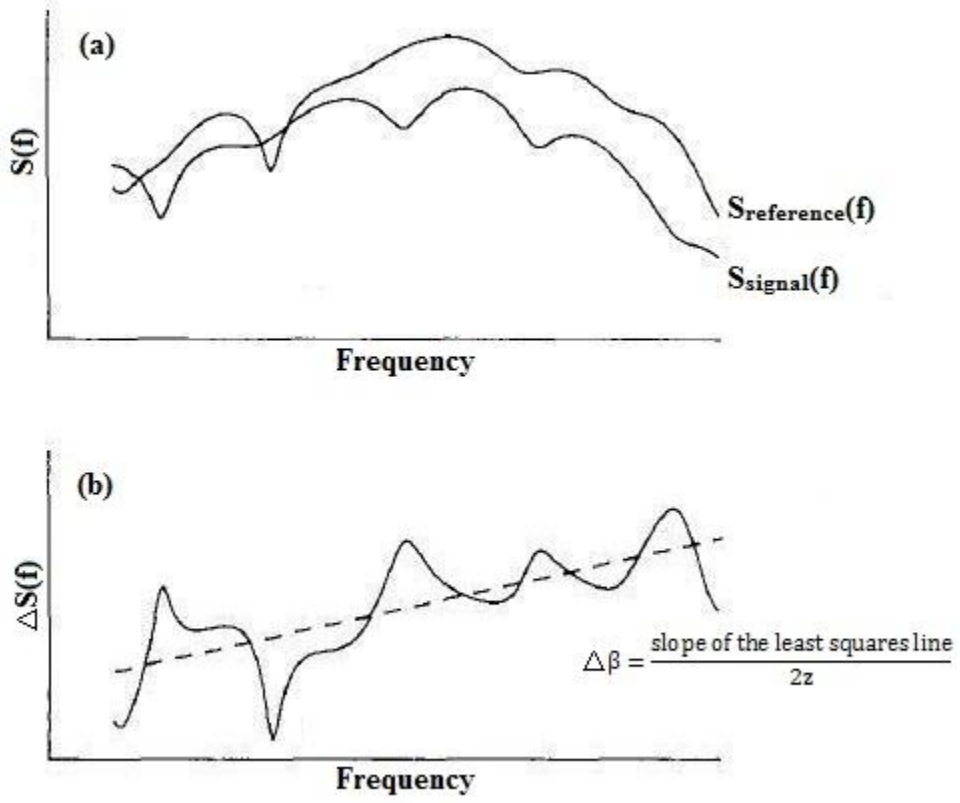

Figure 2-16 (a) $S_{reference}(f)$ and $S_{signal}(f)$ superimposed on the same graph (b) Estimating Δβ by calculating the least squares slope of the line fitted to ΔS(f) (Ophir, et al., 1984)

The attenuation slope algorithm along with a detailed list of the algorithm parameters are presented in appendix B.

2.6 Estimating Changes in Attenuation Intercept ($\Delta\alpha_0$) Using Backscattered Ultrasound Pulses (Attenuation Intercept Algorithm)

Attenuation intercept algorithm is very similar to the attenuation slope algorithm with only a few minor variations. The attenuation slope algorithm was implemented to estimate $\Delta\alpha_0$ in $[\frac{\mathrm{dB}}{\mathrm{cm}}]$ as a function of location in space, with respect to an initial value of α_0 (as a function of space) right before the beginning of HIFU treatment. In order to accomplish that, the changes in the frequency dependent attenuation coefficient at the center frequency of the transmitted pulse, $\Delta\alpha(f_c)$, were constantly estimated throughout the entire treatment cycle, with respect to a reference frame obtained right before the beginning of HIFU exposure. The algorithm would generate a set of 2D matrices, each representing a map of $\Delta\alpha_0$ values (as a function of time (T), depth (z), and line number), with respect to the reference frame obtained at T_0 (T = 0s).

The mathematical description of the steps taken by the attenuation intercept algorithm is identical to that of the attenuation slope algorithm. However, after the acquisition of $\Delta S(f)$, in equation 2.43d, instead of fitting a line to $\Delta S(f)$, the value of $\Delta S(f)$ at the center frequency, f_c, is simply evaluated as follows:

$$\Delta S(f_c) = 2.z.\Delta\,\alpha_0 + 2.z.\Delta\beta.(f_c - f_c) \tag{2.44a}$$

$$\Delta S(f_c) = 2.z.\Delta\,\alpha_0 \tag{2.44b}$$

$\Delta S(f_c)$ is further divided by 2z,

$$\frac{\Delta S(f_c)}{2.z} = \frac{2.z.\Delta\,\alpha_0}{2.z} = \Delta\,\alpha_0 \tag{2.44c}$$

yielding the value of $\Delta\alpha_0$ in $[\frac{\mathrm{Np}}{\mathrm{cm}}]$, which is ultimately converted to $[\frac{\mathrm{dB}}{\mathrm{cm}}]$. The attenuation intercept algorithm along with a detailed list of the algorithm parameters are presented in the appendix C. Figure 2-17 illustrates the steps involved in obtaining $\Delta S(f)$, and estimating $\Delta\alpha_0$.

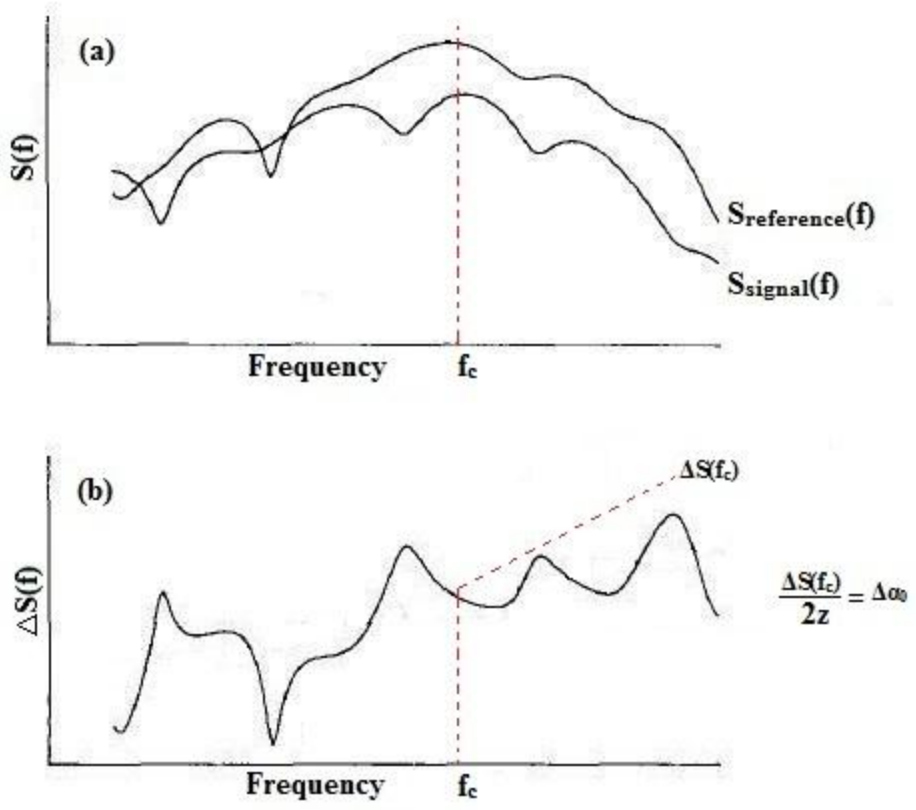

Figure 2-17 (a) $S_{reference}(f)$ and $S_{signal}(f)$ superimposed on the same graph (b) Estimating $\Delta\alpha_0$ by evaluating $\Delta S(f_c)$ (Ophir, et al., 1984)

2.7 Generating Conventional B-mode Images

By definition, a B-mode image is a brightness-modulated image in which depth or axial direction is along the z-axis, and the lateral direction (azimuth) is along the x-axis (Szabo, 2004). It is sometimes referred to as "B-scan" as well. In B-mode images the position of the backscattered pulses or the echoes are determined and mapped based on their acoustic transit times (assuming the speed of sound is constant), and the beam direction in the plane (Szabo, 2004).

In this study, signal x(t) at the receiving end was obtained in the form of digitized RF data (raw backscattered ultrasound data) straight from the SonixRP® ultrasound system. In order to

generate B-mode images, the envelope of the signal x(t), at the receiving end was estimated based on a common envelope estimation method shown in Figure 2-18 (Cobbold, 2007).

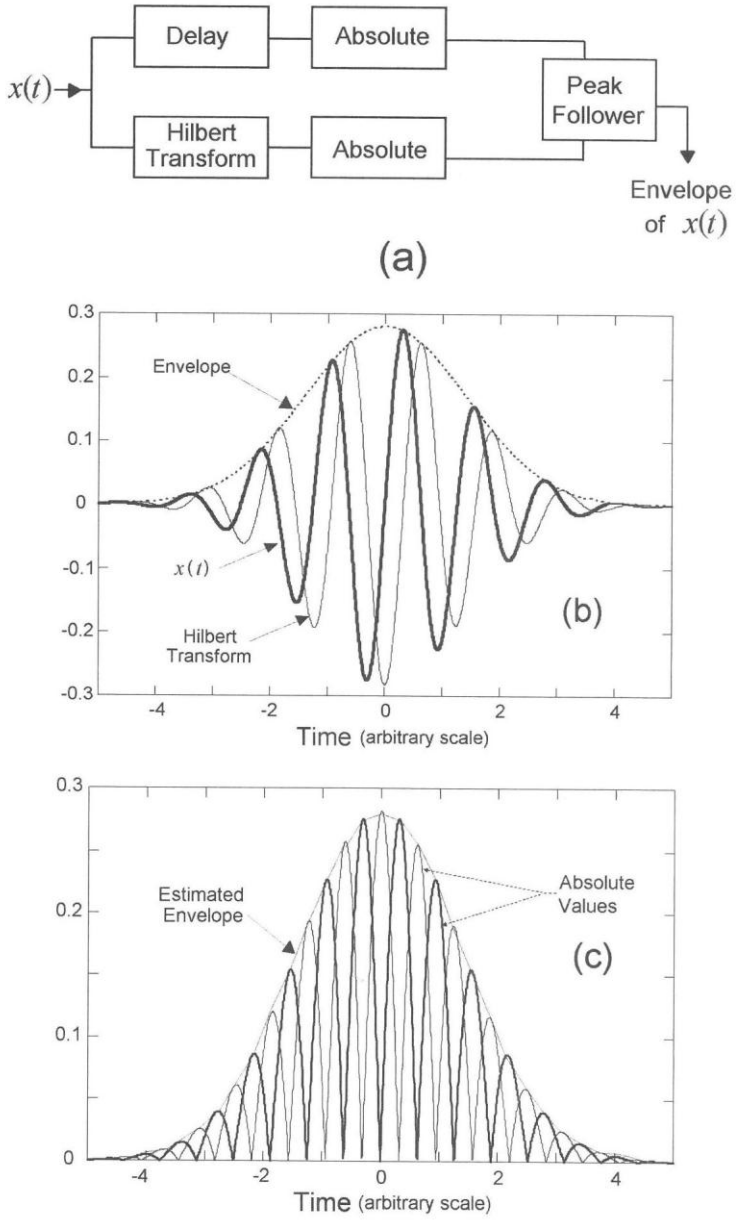

Figure 2-18 Envelope estimation using the Hilbert transform (a) schematic of the method (b) received pulse, x(t), its envelope, and its Hilbert transform (c) absolute value and peak follower outputs (Cobbold, 2007)

In this method, x(t) is a real signal at the receiver end, and the Hilbert transform acts as an ideal -90-degree phase shifter. The original signal, x(t), and the phase shifted signal are added together. The Hilbert transform is typically implemented as an FIR filter so the original signal is delayed to match the group delay of the Hilbert transform. This process is then followed by absolute and then peak follower functions.

The envelope estimation method described in Figure 2-18 was implemented. However, given the fact that during this study the envelope estimation process was not conducted in real-time, the group delay of the Hilbert transform function was no longer consequential, and therefore the duration of the delay shown in Figure 2-18(a) was set to zero.

2.8 LATS (Linear Acoustic and Temperature Simulation)

All computer simulations during this study were conducted using the simulation software called LATS (Linear Acoustic and Temperature Simulation) developed by our own research group (Butt & Tavakkoli, 2011; Butt, Abhari, & Tavakkoli, 2011; Butt F. , 2011). The LATS simulation software conducts simulations based on the linear Rayleigh-Sommerfeld diffraction integral (Cobbold, 2007). The Rayleigh-Sommerfeld integral is commonly applied in the frequency domain in the following form (Harris, 1981),

$$\Phi(r,s) = \int_A \frac{V_n(r_0,s)e^{-sR/c}}{2\Pi R}\,dA \tag{2.45}$$

where Φ(r, s) is the Laplace transform of the velocity potential at a point P located in a homogeneous, isotropic, and non-dissipative medium for a source vibrating with uniform velocity distribution in an infinitely rigid baffle as shown in Figure 2-19.

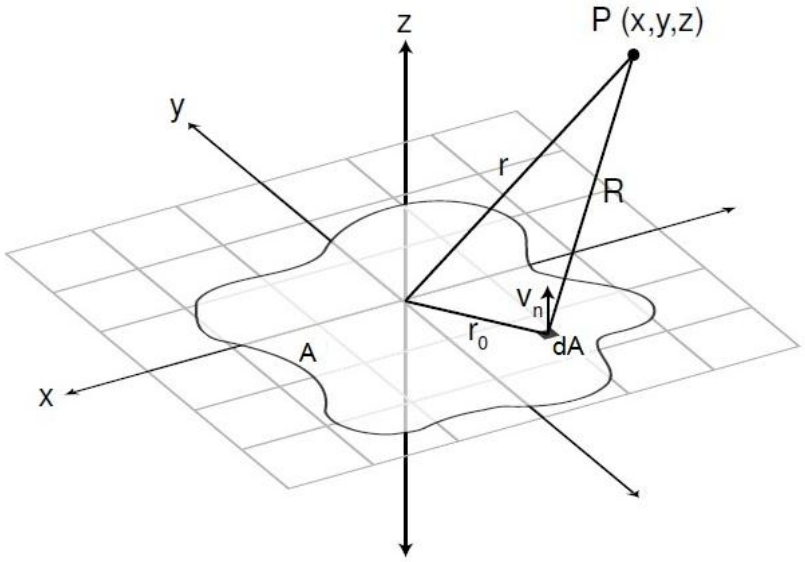

Figure 2-19 An acoustic source with an arbitrary shape, vibrating into a homogeneous, isotropic, non-dissipative medium

By further dividing the acoustic source into several incremental rectangular elements, equation 2.45 (Rayleigh-Sommerfeld integral) can be approximated by (Ocheltree & Frizzell, 1989),

$$p_0 = \frac{j\rho c \Delta w \Delta h}{\lambda} \sum_{n=1}^{N} \frac{u_n e^{(-(\alpha+jk)R)}}{R} \operatorname{sinc}\left(\frac{kx'_n \Delta w}{2R}\right) \operatorname{sinc}\left(\frac{ky'_n \Delta h}{2R}\right) \tag{2.46}$$

where u_n is the velocity amplitude, λ is the wavelength, α is the attenuation coefficient, k is the wave number and ρc is the acoustic impedance.

LATS is a valuable tool for calculating linear acoustic field distributions along with the corresponding temperature profiles and thermal dose distributions, for transducers with different geometries and different propagation mediums. LATS runs simulations based on input parameters such as the geometry and the resonant frequency of the transducer, exposure duration, and the attenuation coefficient of the propagation medium.

3. Results

3.1 Single Element Ultrasound Transducers

3.1.1 Field Profile Simulation

Figure 3-1 illustrates the simulated time averaged acoustic intensity profiles for the single element transducers, used for attenuation measurements. The LATS simulations were run for a total acoustic power (TAP) of 1W at the surface of the transducer.

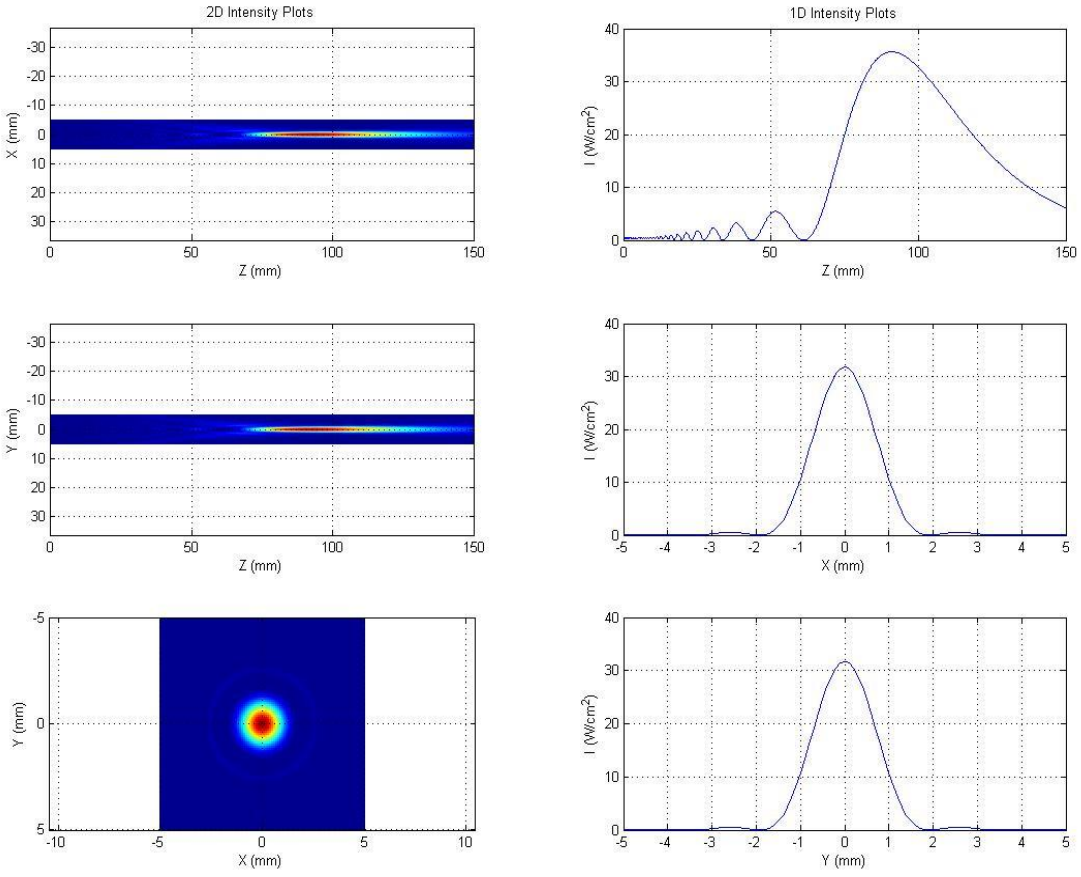

Figure 3-1 Transducer field profile – LATS simulation

The 1-D plots on the right-hand column of Figure 3-1 illustrate free field time averaged acoustic intensities, $\bar{I}$ in $\frac{W}{cm^2}$, along the axial, and lateral directions (x and y directions), from top to bottom, respectively. For a symmetrical circular source, the lateral profiles should theoretically be the same, as they are in this case. The lateral profiles were obtained at the focal point of the transducer. The axial and lateral focal width of the single element ultrasound transducers, based on simulation results, were determined to be 50 mm and 2 mm at full width at half maximum (FWHM), respectively, while the focal length was determined to be 95 mm. The value of focal length obtained from simulations was later compared with the manufacturer and experimental data.

The tissue specimens (both normal and coagulated) used for attenuation measurement were trimmed to 20×80×100 mm pieces. Since the axial focal width always exceeded the thickness of the tissue specimens (50 mm > 20 mm), the tissue specimens placed at the focal region of the single element ultrasound transducers were always entirely within the axial focal width of the ultrasound beam. Similarly, given the lateral focal width of 2 mm, and the given tissue dimensions, the tissue specimens entirely covered the ultrasound beam in the lateral direction as well.

3.1.2 Single Element Ultrasound Transducer Impulse Response

Figure 3-2 is the data provided by the manufacturer for each of the single element ultrasound transducers that were used for attenuation measurements. It illustrates the impulse responses and the spectra for each of the transducers. Although the transducers were identical, there were still minor differences between the two. The same data obtained experimentally under laboratory conditions is presented in appendix-B.

Table 3-1 is a comparison of the manufacturer's data with the experimental data for both of the transducers. The table contains information about the focal length, F#, center frequency, peak frequency, and the 6dB bandwidth for both transducers. As it is evident, there are minor differences between the manufacturer's data, and the experimental data obtained in our laboratory.

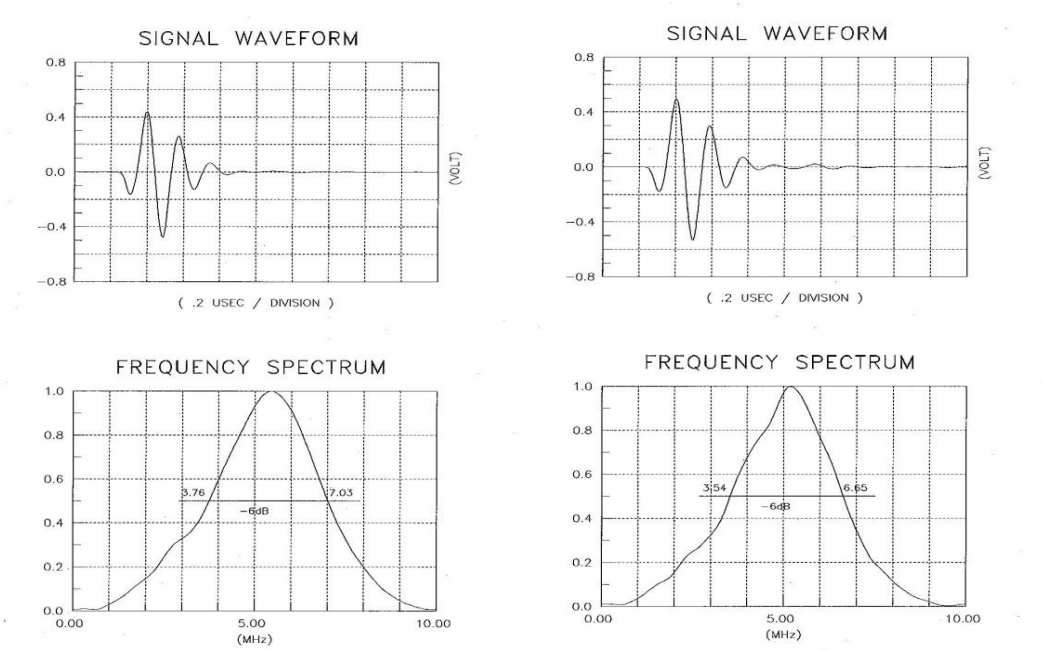

Figure 3-2 Manufacturer's data for impulse response of single element ultrasound transducers and their spectra (a) v308_546803 (b) v308_556849

Table 3-1 Comparison of manufacturer's data and the experimental data

	V308_546803		**V308_556849**	
	Manufacturer Dada	**Experimental Data**	**Manufacturer Data**	**Experimental Data**
F#	5.54	5.11	5.2	5.11
Diameter	19.05 mm	19.05 mm	19.05 mm	19.05 mm
Focal Length	103.175 mm	97.425 mm	101.168 mm	97.275 mm
Center Frequency (f_c)	5.40 MHz	5.32 MHz	5.1 MHz	5.52 MHz
Peak Frequency	5.44 MHz	5.42 MHz	5.2 MHz	5.015 MHz
6dB Bandwidth	3.27 MHz	2.81 MHz	3.11 MHz	1.81 MHz

The value of focal length obtained from simulation results closely matched the focal length values (for both transducers) obtained from experimental results, while it was also very close to the focal length values obtained from manufacturer data.

3.2 HIFU Transducer

3.2.1 Field Profile Analysis

The measured axial and lateral focal width of the HIFU transducer were measured to be 2 mm and 8 mm at full width at half maximum (FWHM), respectively. Figure 3-3 and Figure 3-4 show the axial and lateral field profiles of the HIFU transducer based on hydrophone measurements and simulation results. The simulations were run for a total acoustic power (TAP) of 1W at the surface of the HIFU transducer.

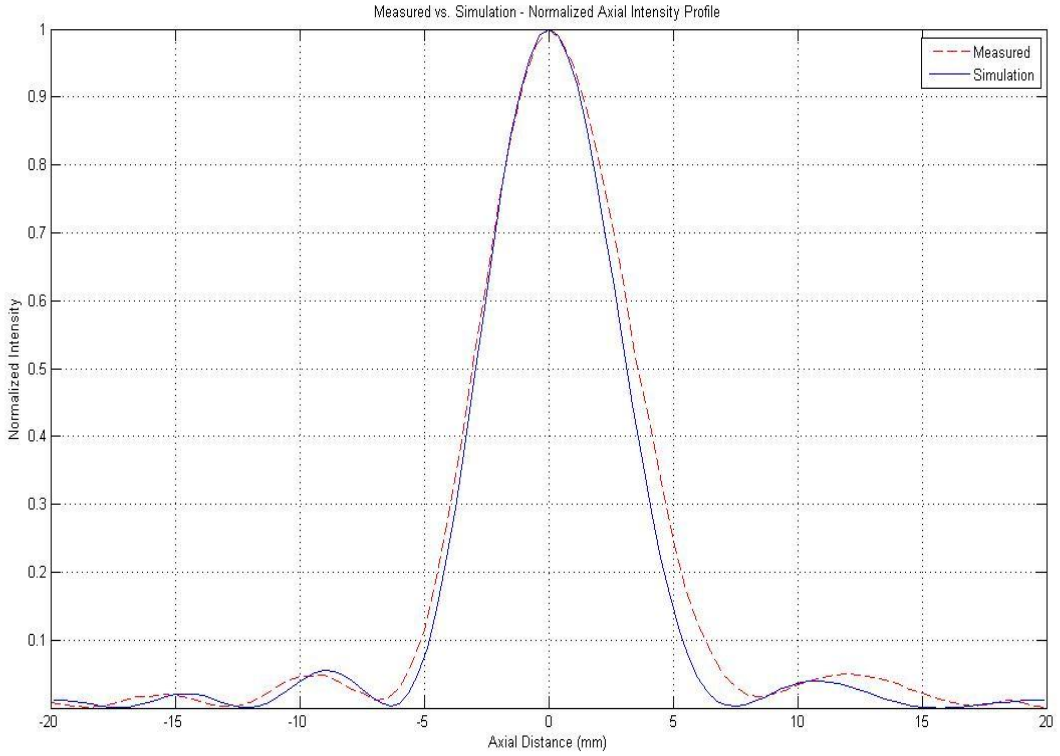

Figure 3-3 Measured and simulated normalized intensity along the axial direction

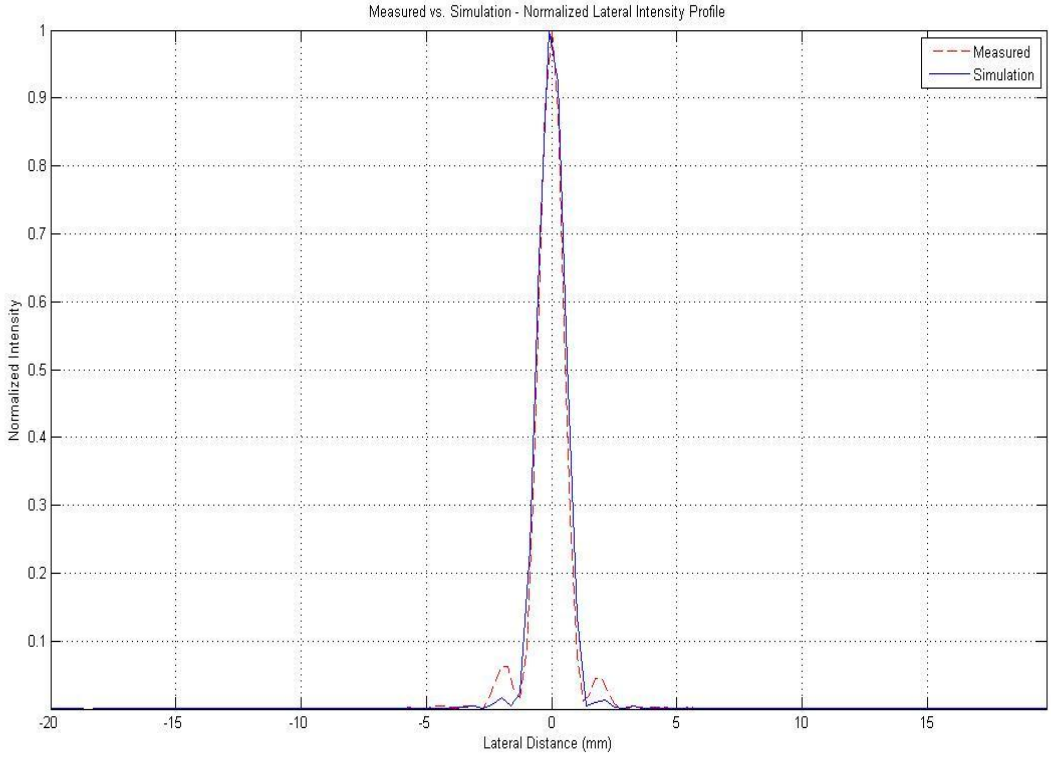

Figure 3-4 Measured and simulated normalized intensity along the lateral direction

3.2.2 Efficiency of the HIFU Transducer

Figure 3-5 illustrates the measured output acoustic power vs. the input electric power for the HIFU transducer. Using linear regression analysis the slope of the fitted line was calculated to be 0.639. Therefore, the efficiency of the transducer was measured to be 63.9% for input electric powers in the range of 0.8 W and 157 W.

Total acoustic powers and the corresponding free field (in water) spatially averaged intensities (I_{SA}) at different input electric power levels were estimated based on the efficiency of the HIFU transducer, the duty cycle (77%), and equation 2.38 with the maximum beam width at FWHM of 2 mm. Table 3-2 is a summary of these values.

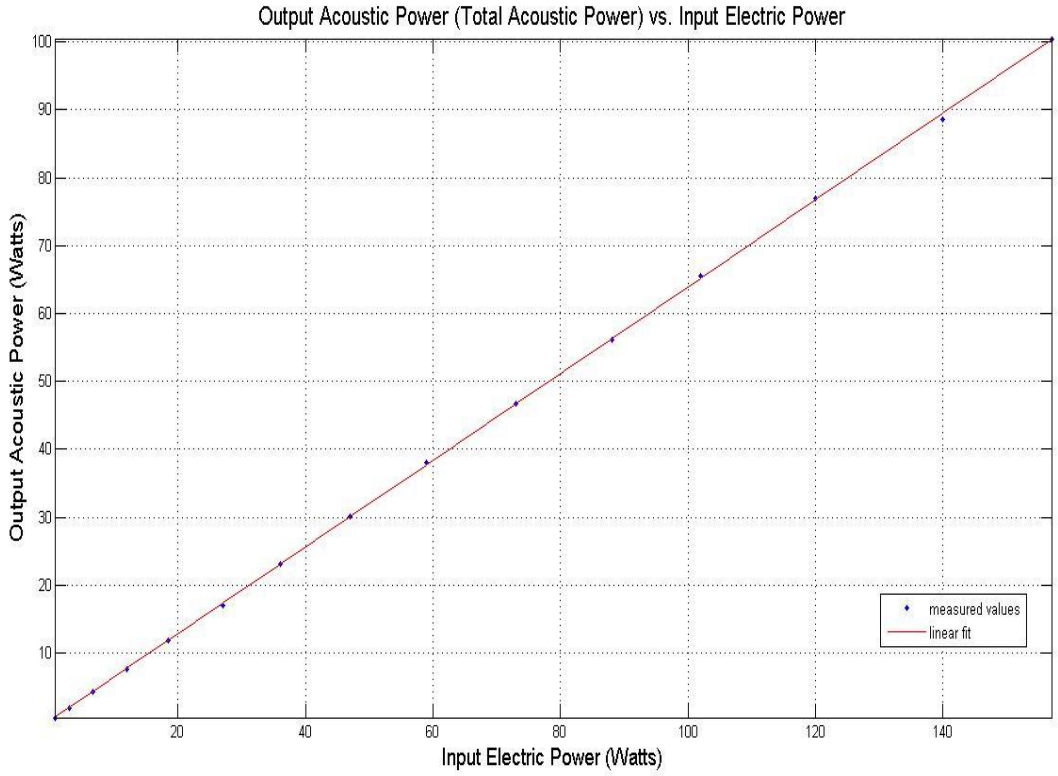

Figure 3-5 Measured output acoustic power (total acoustic power) vs. input electric power

Table 3-2 Total acoustic powers and I_{SA} calculated at corresponding input electric power levels

Input Electric Power (W)	Total Acoustic Power (W)	I_{SA} (W/cm^2)
70	34	737
75	37	801
80	39	845
90	44	961
100	49	1068

3.3 Results of Attenuation Measurement on Phantoms

3.3.1 Attenuation Coefficient of PVCP

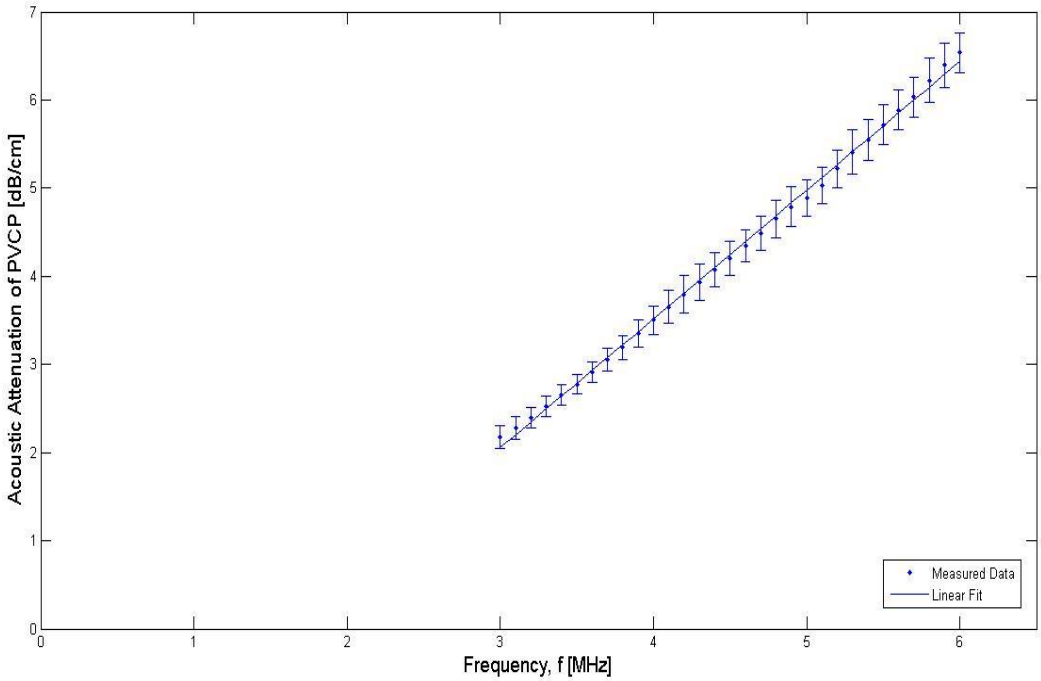

Figure 3-6 Means and standard errors of the attenuation coefficient versus frequency for PVCP attenuation phantoms, along with least squares best fit straight line for the data set

Figure 3-6 presents the mean attenuation coefficient of the PVCP phantoms, averaged over 18 sets of measured data, plotted as a function of frequency between 3-6 MHz and the least squares straight line (equation 2.14) was fitted to the data set. Based on linear regression analysis, at a 99% confidence, the least squares attenuation slope was measured to be,

$$\beta = (1.46 \pm 0.03)\ \frac{\text{dB}}{\text{MHz.cm}} \tag{3.1}$$

While, the attenuation coefficient at the center frequency of 5MHz (attenuation intercept) was measured to be,

$$\alpha_0 = (4.79\ \pm 0.23)\ \frac{\text{dB}}{\text{cm}} \tag{3.2}$$

Based on the values of α_0 and β, the linear approximation of the frequency dependent attenuation coefficient, $\alpha(f)$, for the PVCP attenuation phantoms at f_c = 5 MHz, was determined to be,

$$\alpha(f)_{PVCP\_dB} = (4.79 \pm 0.23) + (1.46 \pm 0.03)(f - f_c) \quad (3.3)$$

3.3.2 Comparison of Results with Previous Measurement

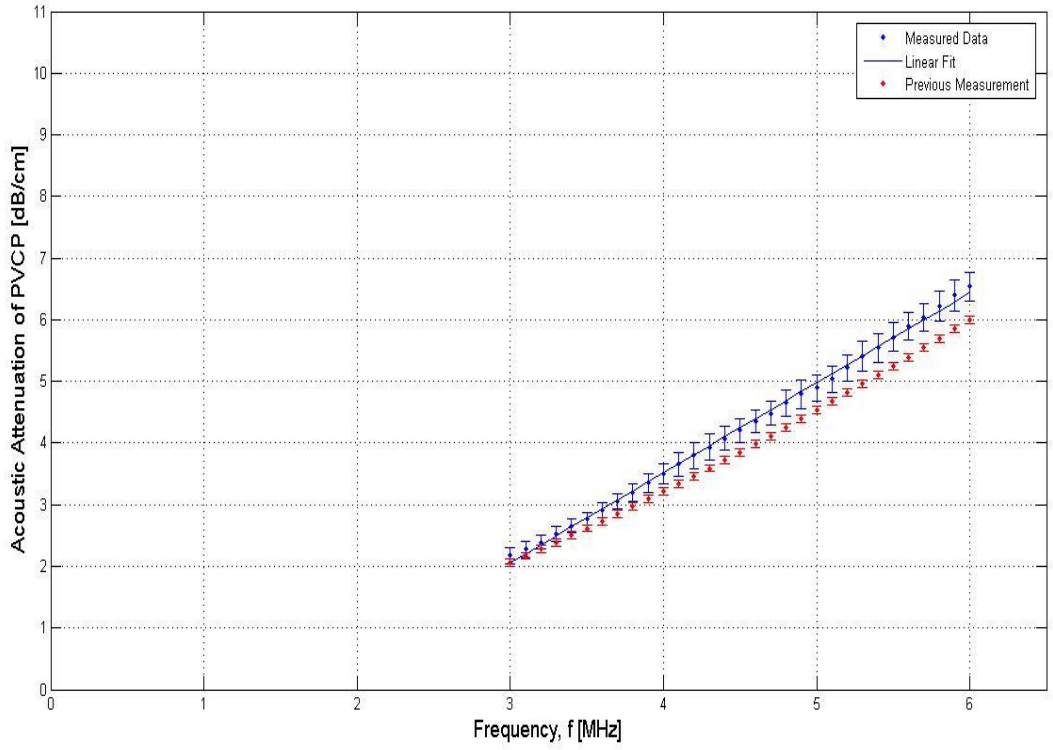

Figure 3-7 Attenuation coefficient versus frequency for PVCP, comparison with published data

Figure 3-7 illustrates frequency dependent attenuation coefficient of PVCP that was measured during this study along with previous measurements conducted throughout a previous study on the same PVCP phantoms (Soleimankhani, 2007). The results from the previous measurements on the same phantoms were generated under identical experimental conditions, the same frequency range, and the same ultrasound transducers.

3.4 Results of Attenuation Measurement on *Ex vivo* Porcine Muscle Tissue

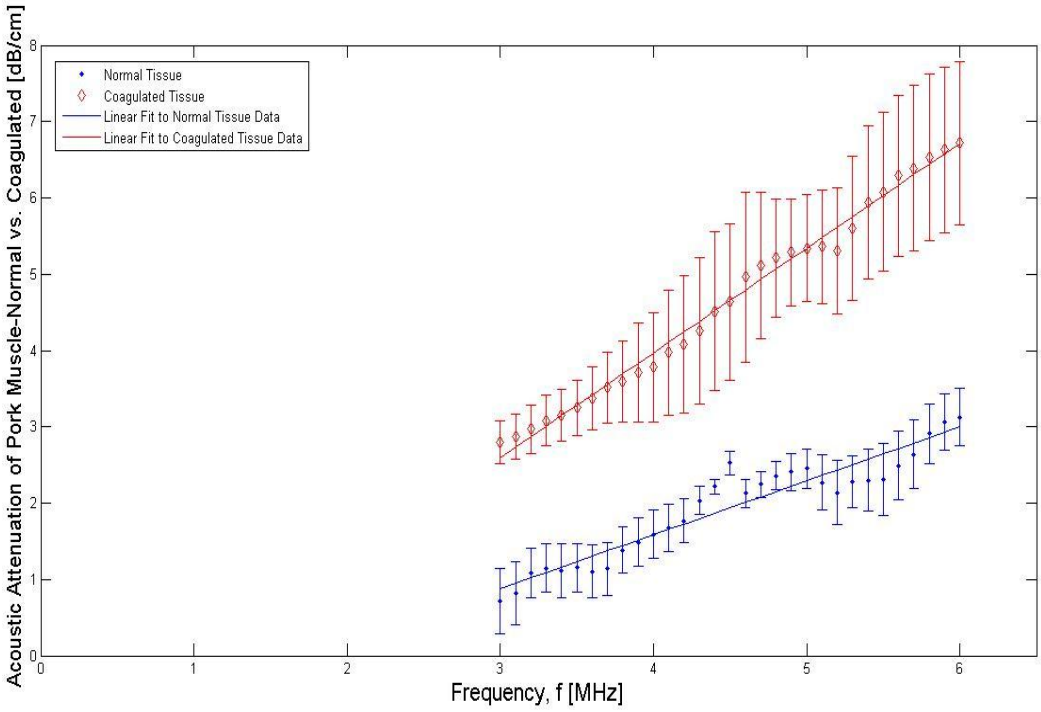

Figure 3-8 Means and standard errors of the attenuation coefficient versus frequency for normal and coagulated ex vivo porcine muscle tissues, along with least squares best fit straight lines for the data sets

Figure 3-8 presents data sets for both normal and coagulated *ex vivo* porcine muscle tissues. It presents the mean attenuation coefficient of normal *ex vivo* porcine muscle tissues, averaged over 8 sets of measured data, plotted as a function of frequency between 3-6MHz. The least squares straight line (equation 2.14) was fitted to the averaged data points. Based on linear regression analysis, at a 99% confidence, the least squares attenuation slope for normal *ex vivo* porcine muscle tissue was measured to be,

$$\beta = (0.71 \pm 0.12)\ \frac{\text{dB}}{\text{MHz.cm}} \tag{3.4}$$

While, the attenuation coefficient for normal *ex vivo* porcine muscle tissue at the center frequency of 5 MHz (attenuation intercept) was measured to be,

$$\alpha_0 = (2.41 \pm 0.24)\ \frac{\text{dB}}{\text{cm}} \tag{3.5}$$

Based on the values of α_0 and β, the linear approximation of the frequency dependent attenuation coefficient, $\alpha(f)$, for normal *ex vivo* porcine muscle tissue at f_c = 5 MHz, was determined to be,

$$\alpha(f)_{N\_dB} = (2.41 \pm 0.24) + (0.71 \pm 0.12)(f - f_c) \tag{3.6}$$

Similarly in Figure 3-8, the mean attenuation coefficient of coagulated *ex vivo* porcine muscle tissues, averaged over 8 sets of measured data was plotted as a function of frequency between 3 to 6 MHz, and the least squares straight line (equation 2.14) was fitted to the data set. Based on linear regression analysis, at a 99% confidence, the least squares attenuation slope for coagulated *ex vivo* porcine muscle tissue was measured to be,

$$\beta = (1.37 \pm 0.07)\ \frac{\text{dB}}{\text{MHz. cm}} \tag{3.7}$$

While, the attenuation coefficient for coagulated *ex vivo* porcine muscle tissue at the center frequency of 5 MHz (attenuation intercept) was measured to be,

$$\alpha_0 = (5.28 \pm 0.71)\ \frac{\text{dB}}{\text{cm}} \tag{3.8}$$

Based on the values of α_0 and β, the linear approximation of the frequency dependent attenuation coefficient, $\alpha(f)$, for coagulated *ex vivo* porcine muscle tissue at f_c = 5 MHz, was determined as,

$$\alpha(f)_{C\_dB} = (5.28 \pm 0.71) + (1.37 \pm 0.07)(f - f_c) \tag{3.9}$$

As it is evident, the results indicate that there is a significant difference between the frequency dependent attenuation coefficients of normal and coagulated porcine muscle tissues. Based on the trend presented in Figure 3-8 there is a significant increase in the attenuation coefficient of coagulated tissue relative to attenuation coefficient of normal tissue. This increase manifests itself in both the attenuation intercept term (α_0) and the least squares attenuation slope term (β) of the frequency dependent attenuation coefficient. Table 3-3 and Table 3-4 present quantitative summaries of increase in attenuation intercept, and attenuation slope between normal and coagulated tissues.

Table 3-3 Attenuation coefficient slopes (β) measured in normal and coagulated *ex vivo* porcine muscle tissues

Normal [dB/(MHz.cm)]	**Coagulated [dB/(MHz.cm)]**	**Δβ [dB/(MHz.cm)]**	**% Change of attenuation slope relative to normal**
0.71 ± 0.12	1.37 ± 0.07	0.67 ± 0.14	+ 94

Table 3-4 Attenuation coefficient intercepts (α_0) measured in normal and coagulated *ex vivo* porcine muscle tissues

Normal [dB/cm]	**Coagulated [dB/cm]**	**$\Delta\alpha_0$ [dB/cm]**	**% Change of attenuation slope relative to normal**
2.41 ± 0.24	5.28 ± 0.71	2.87 ± 0.75	+ 119

The results indicate that there is a 94% increase in the value of attenuation slope (β) and a 119% increase in the value of attenuation intercept (α_0) of coagulated tissue with respect to normal tissue. Bush et al. (Bush, Rivens, ter Haar, & Bamber, 1993), in a very similar experiment have reported similar results for *ex vivo* porcine livers with, $\Delta\beta \approx 1 \frac{\text{dB}}{\text{MHz.cm}}$ (≈+139% increase), and $\Delta\alpha_0 \approx 3 \frac{\text{dB}}{\text{cm}}$ (≈ +94% increase).

3.5 Results of Attenuation Estimation on *Ex vivo* Porcine Muscle Tissue as a Function of HIFU Exposure

3.5.1 Results of Attenuation Slope Algorithm

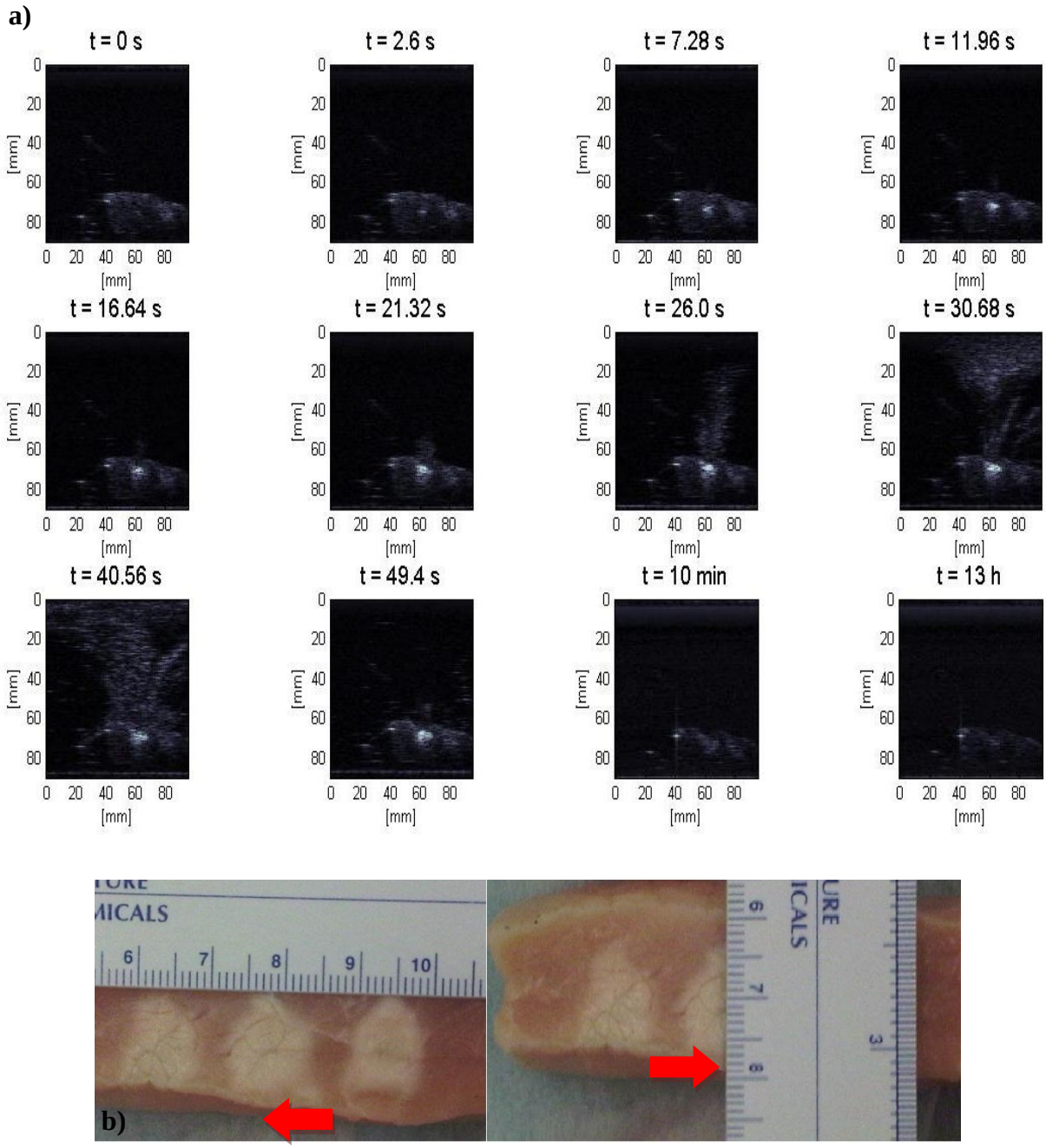

Figure 3-9 (a) Lesion growth in *ex vivo* porcine muscle tissue in conventional B-mode images, the input electric power of HIFU was 100 W, and the duty cycle was 77% for a total HIFU treatment time of 40 s (b) Lesion induced in degassed *ex vivo* porcine muscle tissues, where the average focal intensity at the HIFU treatment site was 1068 W/cm^2

The visualization of lesion formation was directly correlated with the B-mode images formed from the pulse-echo RF data, shown in Figure 3-9, with the HIFU transducer being on top. Figure 3-10 showed the corresponding Δβ images generated using the same RF data, with every frame representing a 2-D map of change in least squares attenuation coefficient slope (Δβ). Figure 3-11 showed the dynamic changes of attenuation slope as a result of HIFU treatment in *ex vivo* porcine muscle tissue. The results presented in Figure 3-9 to Figure 3-11 were all obtained from the same experiment. The created lesion was monitored for duration of 13 hours.

As shown in Figure 3-9 a bright hyperechoic region appeared at the focal region in the B-mode image at 2.6 s, and then enlarged and grew in intensity during HIFU treatment. Corresponding to the hyperechoic region that appeared in the B-mode images, Figure 3-10 revealed a high intensity region that appeared in the Δβ images at 2.6 s, and then enlarged and grew in intensity during HIFU treatment. After the treatment, the bright hyperechoic region in the focal region of the B-mode image began to gradually fade, and after 10 minutes it was hardly visible in the B-mode images. After 13 hours, the hyperechoic region was virtually invisible in the B-mode image. Meanwhile, even after 13 hours, the high intensity region in the Δβ images remained visible. However, this high intensity region decreased in size and intensity after 10 minutes had passed, and after 13 hours it decreased in size and intensity to a higher extent. Figure 3-11 provided a more quantitative assessment of the dynamic changes of Δβ in the region of interest. Based on Figure 3-11, Δβ rose very rapidly in the first 20 s of treatment, from 0 to 2 $\frac{\text{dB}}{\text{MHz.cm}}$ and then stayed at 2 $\frac{\text{dB}}{\text{MHz.cm}}$ with some fluctuations for the next 20 s until the end of HIFU treatment at 40 s. After treatment, Δβ gradually decreased and At 10 minutes, the Δβ algorithm detected a value of 1.3 $\frac{\text{dB}}{\text{MHz.cm}}$. At 13 hours, the Δβ algorithm detected a value of 0.75 $\frac{\text{dB}}{\text{MHz.cm}}$.

The assumption was made that all bubble activities had completely vanished 10 minutes after the end of HIFU treatment (Coussios, et al., 2007; Khokhlova, et al., 2006). In addition, due to the heat transfer properties of soft biological tissues, it could safely be assumed that the temperature in the region of interest had cooled down to its pre-treatment level. As a result, the output of the Δβ algorithm at 10 minutes was used as an indication of the performance of the algorithm under steady state conditions (the absence of boiling bubbles, and no temperature rise).

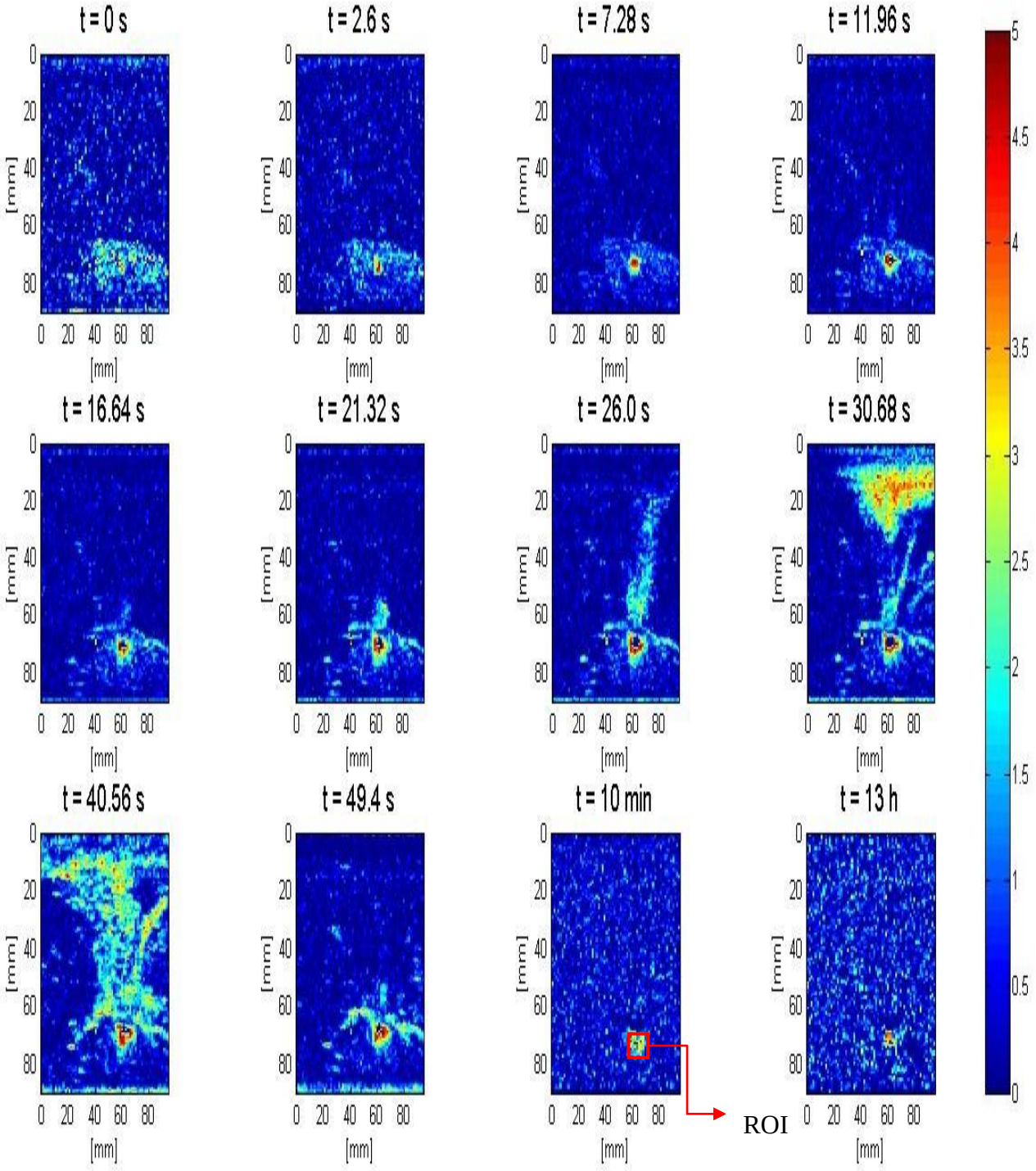

Figure 3-10 Lesion growth in *ex vivo* porcine muscle tissue in Δβ images, the input electric power of HIFU was 100 W, and the duty cycle was 77% for a total HIFU treatment time of 40 s

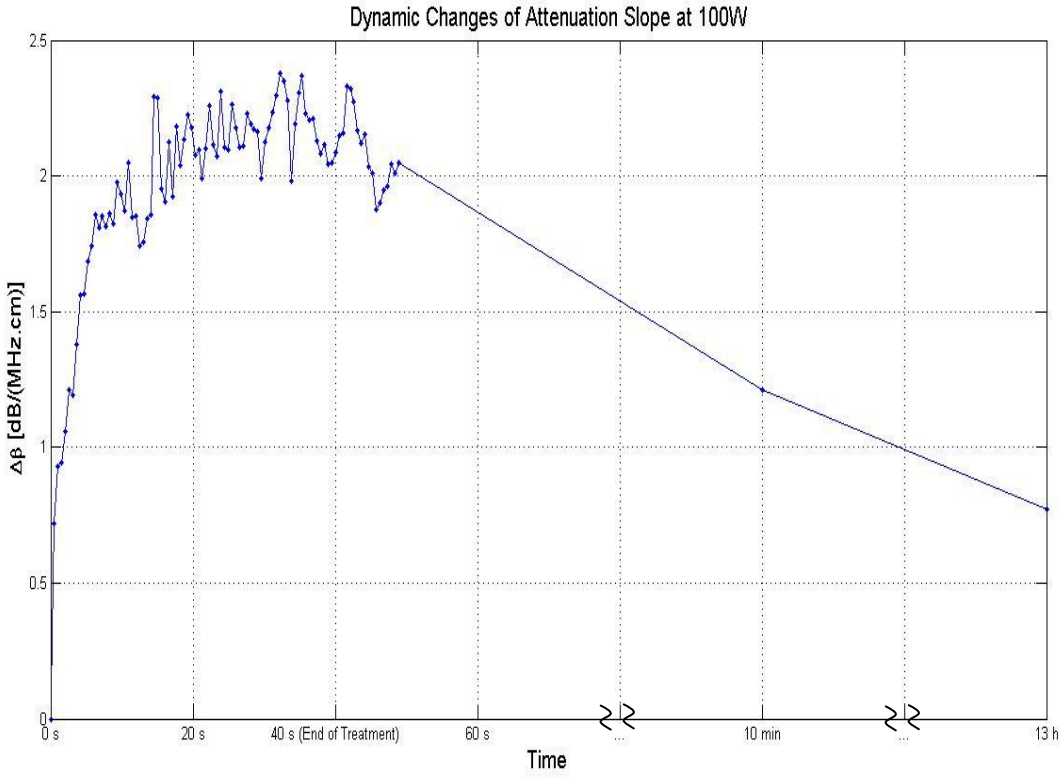

Figure 3-11 Dynamic changes of Δβ in *ex vivo* porcine muscle tissue during HIFU treatment, Δβ values were estimated by spatially averaging the Δβ values, axially and laterally in the region of interest (10 mm × 10 mm) centered around the lesion generated by HIFU as shown in Figure 3-10**, the input electric power of HIFU was 100 W, and the duty cycle was 77% for a total HIFU treatment time of 40 s**

Figure 3-12 showed Δβ images generated by the attenuation slope algorithm at different input electric powers, nearly 10 minutes after the end of treatment (steady state). A total of four lesions were created at every power level. These Δβ images were used to assess the performance of the attenuation slope algorithm.

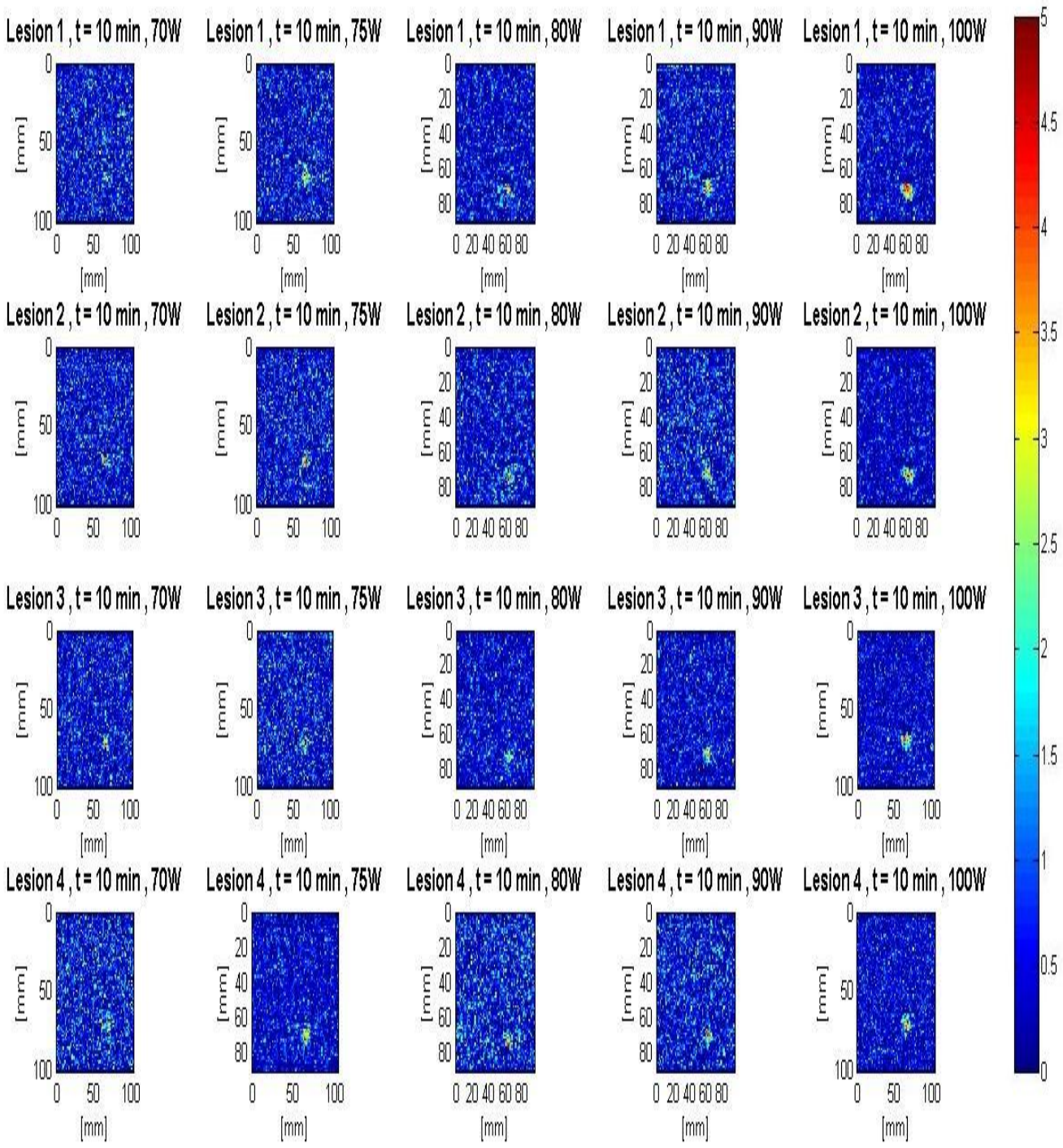

Figure 3-12 Δβ images detecting lesions in *ex vivo* porcine muscle tissues at 10 minutes, the input electric power of HIFU was 70 W, 75 W, 80 W, 90 W, and 100 W, and the duty cycle was 77% for a total HIFU treatment time of 40 s, a total of four lesions were created at every power level

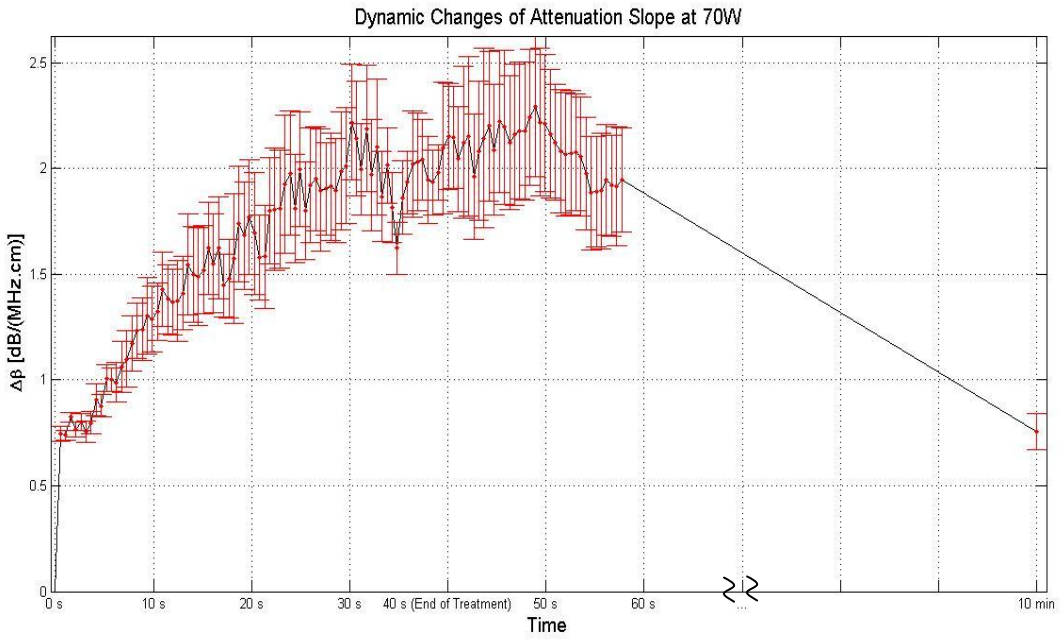

Figure 3-13 Dynamic changes of Δβ (spatially averaged in ROI) in *ex vivo* porcine muscle tissue during HIFU treatment, for monitoring duration of 10 min, the input electric power of HIFU was 70 W, and the duty cycle was 77% for a total HIFU treatment time of 40 s

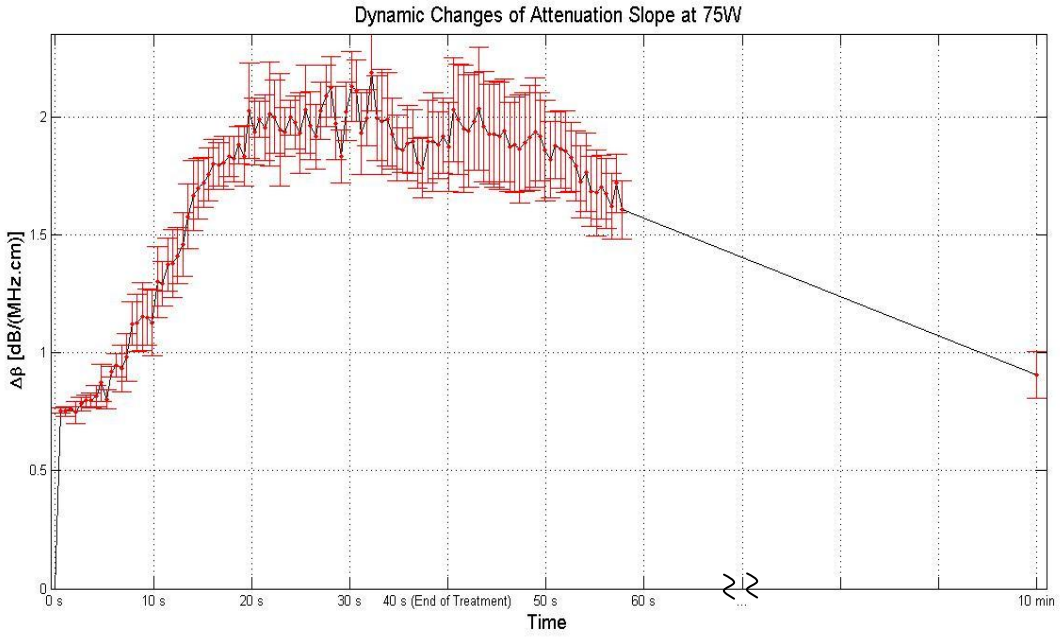

Figure 3-14 Dynamic changes of Δβ (spatially averaged in ROI) in *ex vivo* porcine muscle tissue during HIFU treatment, for monitoring duration of 10 min, the input electric power of HIFU was 75 W, and the duty cycle was 77% for a total HIFU treatment time of 40 s

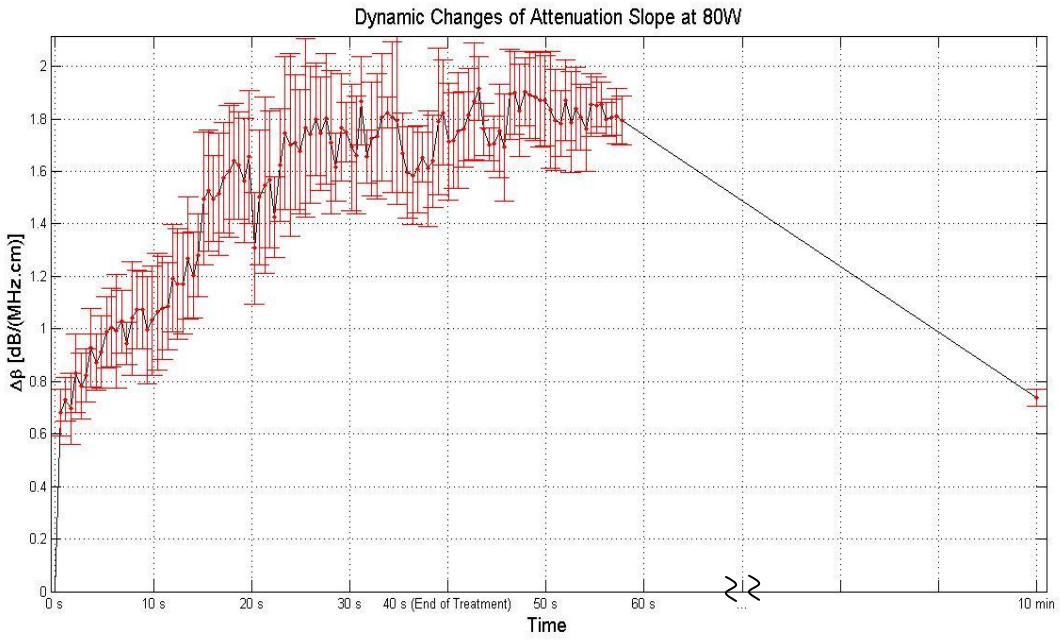

Figure 3-15 Dynamic changes of Δβ (spatially averaged in ROI) in *ex vivo* porcine muscle tissue during HIFU treatment, for monitoring duration of 10 min, the input electric power of HIFU was 80 W, and the duty cycle was 77% for a total HIFU treatment time of 40 s

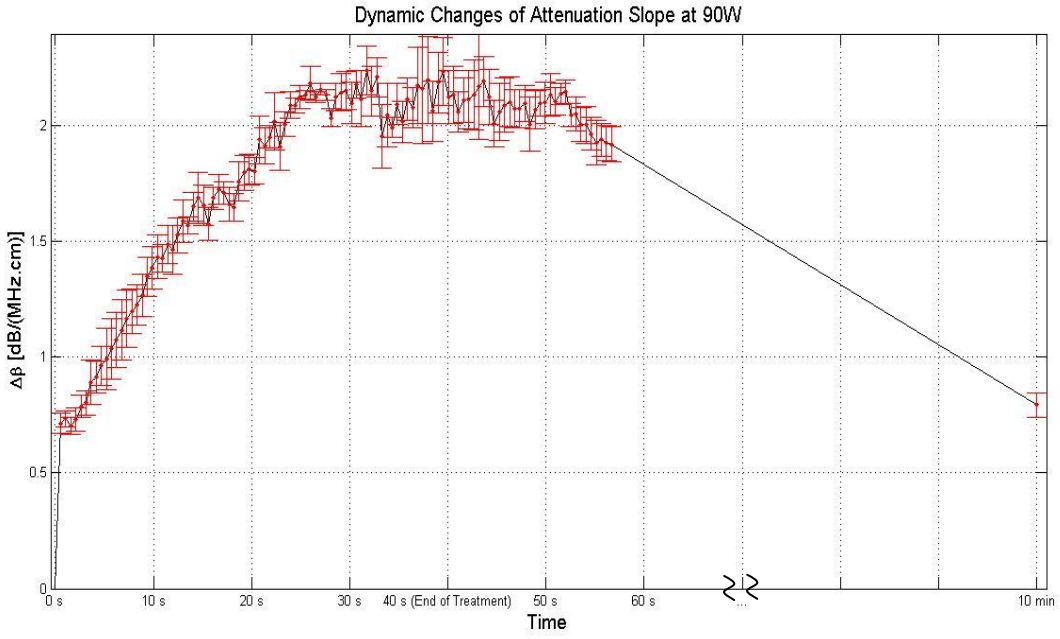

Figure 3-16 Dynamic changes of Δβ (spatially averaged in ROI) in *ex vivo* porcine muscle tissue during HIFU treatment, for monitoring duration of 10 min, the input electric power of HIFU was 90 W, and the duty cycle was 77% for a total HIFU treatment time of 40 s.

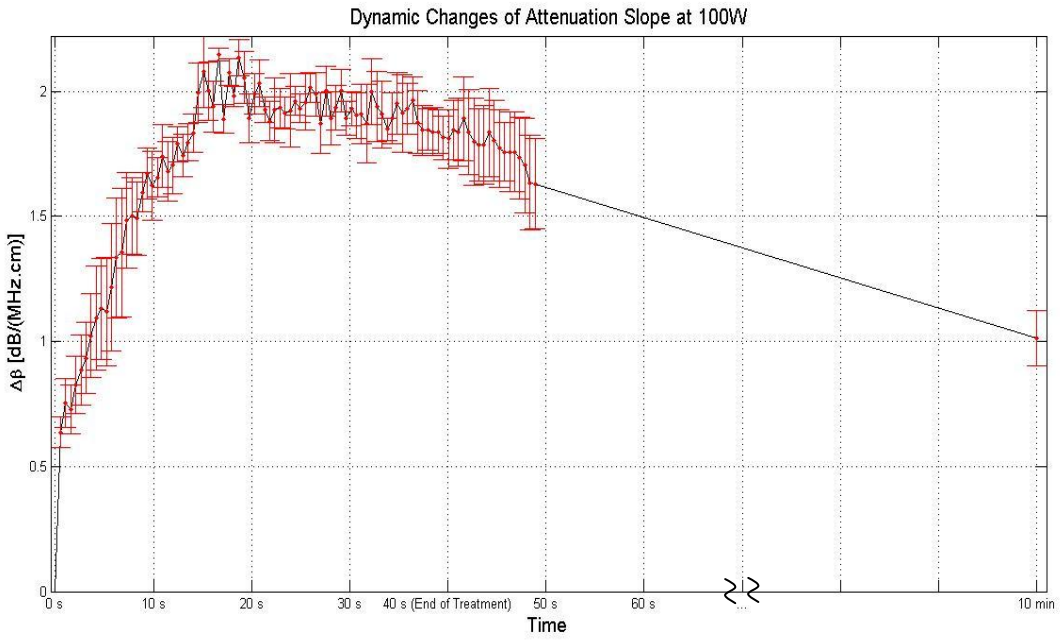

Figure 3-17 Dynamic changes of Δβ (spatially averaged in ROI) in *ex vivo* porcine muscle tissue during HIFU treatment, for monitoring duration of 10 min, the input electric power of HIFU was 100 W, and the duty cycle was 77% for a total HIFU treatment time of 40 s

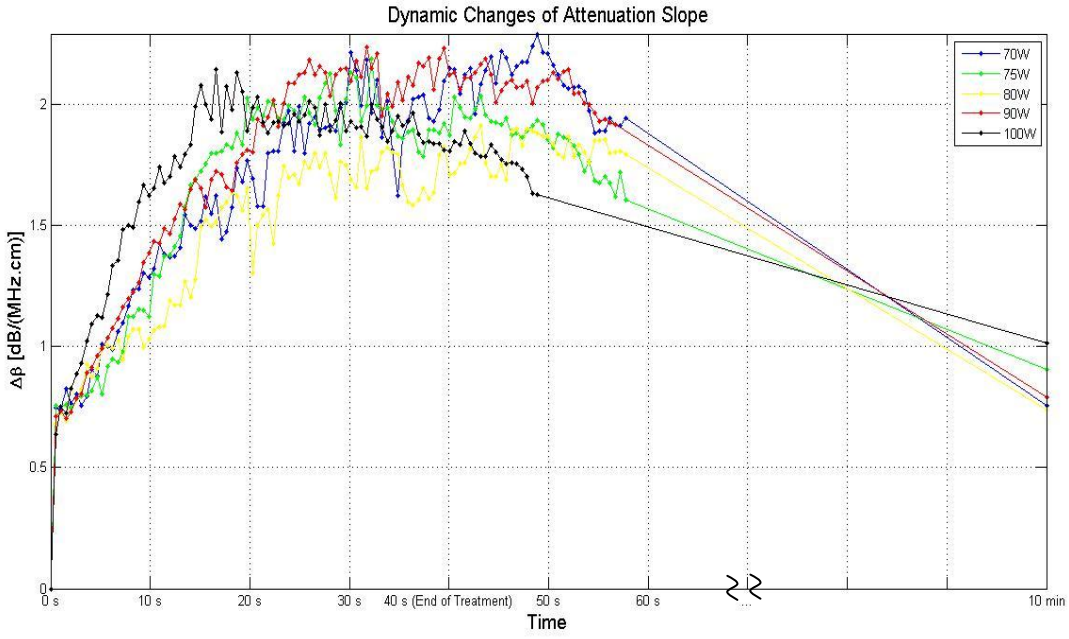

Figure 3-18 Dynamic changes of Δβ (spatially averaged in ROI) in *ex vivo* porcine muscle tissue during HIFU treatment, for monitoring duration of 10 min, the input electric power of HIFU was 70 W, 75 W, 80W, 90 W, 100 W, and the duty cycle was 77% for a total HIFU treatment time of 40 s

Figure 3-13 to Figure 3-18 showed the dynamic changes of attenuation slope as a result of HIFU treatment in *ex vivo* porcine muscle tissue at different input electric powers. These figures provided a quantitative assessment of the changes in Δβ for duration of 10 minutes.

Based on results in Figure 3-18, at all investigated input electric powers, Δβ rose very rapidly in the first 20 s of treatment, from 0 to values in the range of 1.5-2 $\frac{\text{dB}}{\text{MHz.cm}}$ and then maintained its values at that range with some fluctuations for the next 20 s to the end of HIFU treatment at 40 s. After the end of treatment, Δβ values gradually decreased and after10 minutes, the Δβ algorithm detected values in the range of 0.75-1 $\frac{\text{dB}}{\text{MHz.cm}}$. Table 3-5 summarized the Δβ values at 10 minutes, at different input electric powers.

Table 3-5 Δβ values vs. input electric power, at t = 10 min

Input Electric Power (W)	**Δβ ($\frac{\text{dB}}{\text{MHz.cm}}$)**
70	0.76 ± 0.09
75	0.91 ± 0.10
80	0.74 ± 0.03
90	0.79 ± 0.05
100	1.01 ± 0.11

3.5.2 Results of Attenuation Intercept Algorithm

The attenuation intercept algorithm was used on the exact same set of data that was previously used for the attenuation slope algorithm. Once again the visualization of lesion formation was directly correlated with the B-mode images acquired from the pulse-echo RF data, shown in Figure 3-9. Figure 3-19 showed the corresponding $\Delta\alpha_0$ images generated using the same RF data, with every frame representing a 2-D map of change in attenuation coefficient intercept ($\Delta\alpha_0$). Figure 3-20 showed the dynamic changes of attenuation intercept as a result of HIFU treatment in *ex vivo* porcine muscle tissue. The results presented in Figure 3-9 to Figure 3-20 were all obtained from the same experiment.

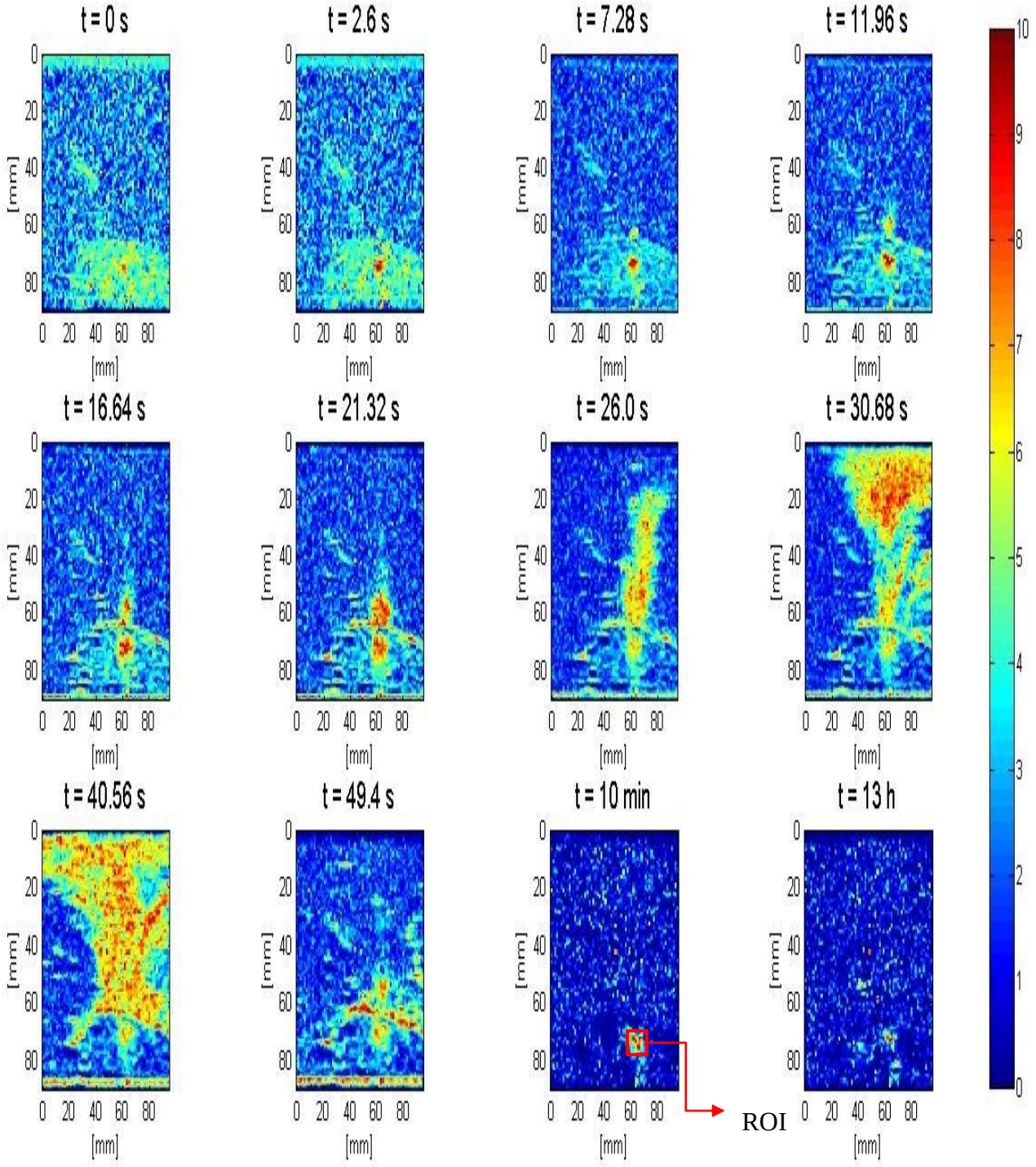

Figure 3-19 Lesion growth in *ex vivo* porcine muscle tissue in $\Delta\alpha_0$ images, the input electric power of HIFU was 100 W, and the duty cycle was 77% for a total HIFU treatment time of 40 s

Similar to previous results, corresponding to the hyperechoic region that appeared in the B-mode images at t = 2.6 s, Figure 3-19 revealed a high intensity region that appeared in the $\Delta\alpha_0$ images at 2.6 s. Once again this high intensity region enlarged and grew in intensity during HIFU treatment. 13 hours after the treatment, the high intensity region in the $\Delta\alpha_0$ images remained visible. However, this high intensity region, in an outcome similar to $\Delta\beta$ images, decreased in size and intensity after 10 minutes had passed, and after 13 hours it decreased in size and intensity to a higher extent. Figure 3-20 provided a more quantitative assessment of the dynamic changes of $\Delta\alpha_0$ in the region of interest.

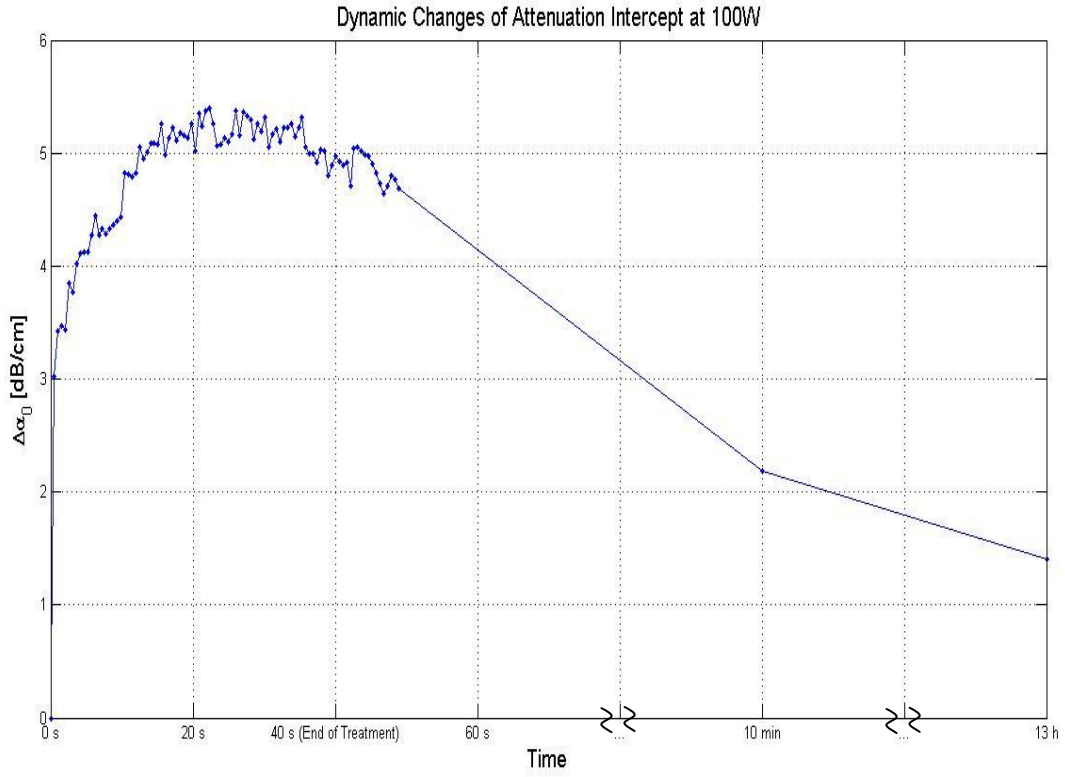

Figure 3-20 Dynamic changes of $\Delta\alpha_0$ in *ex vivo* porcine muscle tissue during HIFU treatment, $\Delta\alpha_0$ values were estimated by spatially averaging the $\Delta\alpha_0$ values, axially and laterally in the region of interest (10 mm × 10 mm) centered around the lesion generated by HIFU as shown in Figure 3-19**, the input electric power of HIFU was 100 W, and the duty cycle was 77% for a total HIFU treatment time of 40 s.**

Based on Figure 3-20 $\Delta\alpha_0$ rose very rapidly in the first 20 s of treatment, from 0 to 5 $\frac{\mathrm{dB}}{\mathrm{cm}}$ and then tended to stay at 5 $\frac{\mathrm{dB}}{\mathrm{cm}}$ with some fluctuations for the next 20 s to the end of HIFU treatment at

40s. After treatment, $\Delta\alpha_0$ gradually decreased and At 10 minutes, the $\Delta\alpha_0$ algorithm detected approximately a value of 2 $\frac{\mathrm{dB}}{\mathrm{cm}}$. At 13 hours, the $\Delta\alpha_0$ algorithm detected a value of 1.5 $\frac{\mathrm{dB}}{\mathrm{cm}}$.

Once again, based on the assumption that all bubble activities had completely vanished 10 minutes after the end of HIFU treatment (Coussios, et al., 2007; Khokhlova, et al., 2006), and due to the heat transfer properties of soft biological tissues, it was safely assumed that the temperature in the region of interest had cooled down to its pre-treatment level. As a result, similar to the case of attenuation slope algorithm, the output of the $\Delta\alpha_0$ algorithm at 10 minutes was used as an indication of the performance of the attenuation intercept algorithm under steady state conditions (the absence of bubbles, and no temperature rise).

Figure 3-21 showed $\Delta\alpha_0$ images generated by the attenuation intercept algorithm at different input electric powers, nearly 10 minutes after the end of treatment. A total of four lesions were created at every power level. These $\Delta\alpha_0$ images were used to assess the performance of the attenuation intercept algorithm.

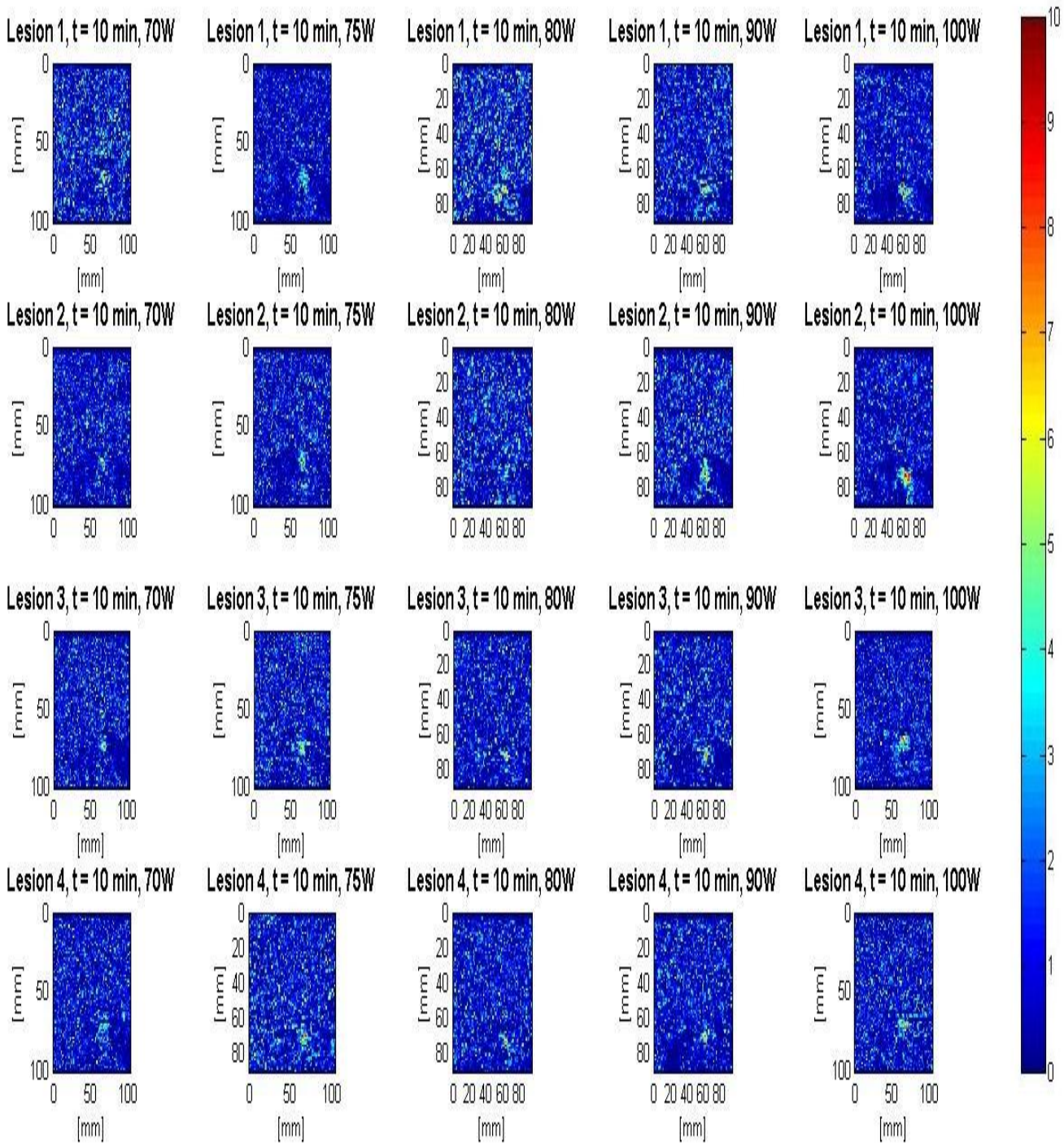

Figure 3-21 $\Delta\alpha_0$ images detecting lesions in *ex vivo* porcine muscle tissues at 10 minutes, the input electric power of HIFU was 70 W, 75 W, 80 W, 90 W, and 100 W, and the duty cycle was 77% for a total HIFU treatment time of 40 s. A total of four lesions were created at every power level.

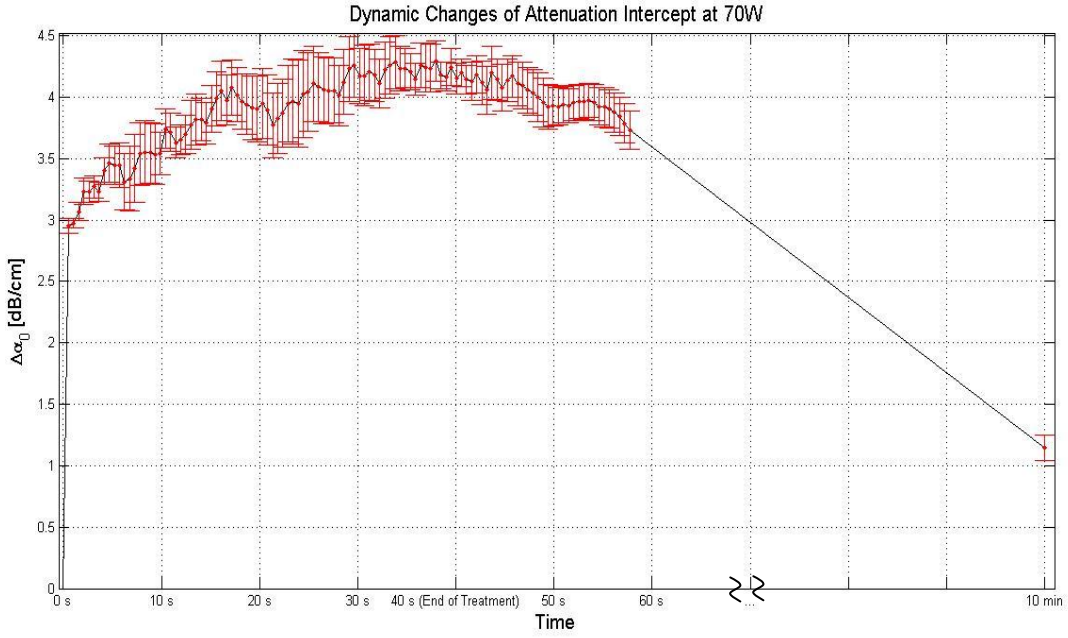

Figure 3-22 Dynamic changes of $\Delta\alpha_0$ (spatially averaged in ROI) in *ex vivo* porcine muscle tissue during HIFU treatment, for monitoring duration of 10 min, the input electric power of HIFU was 70 W, and the duty cycle was 77% for a total HIFU treatment time of 40 s

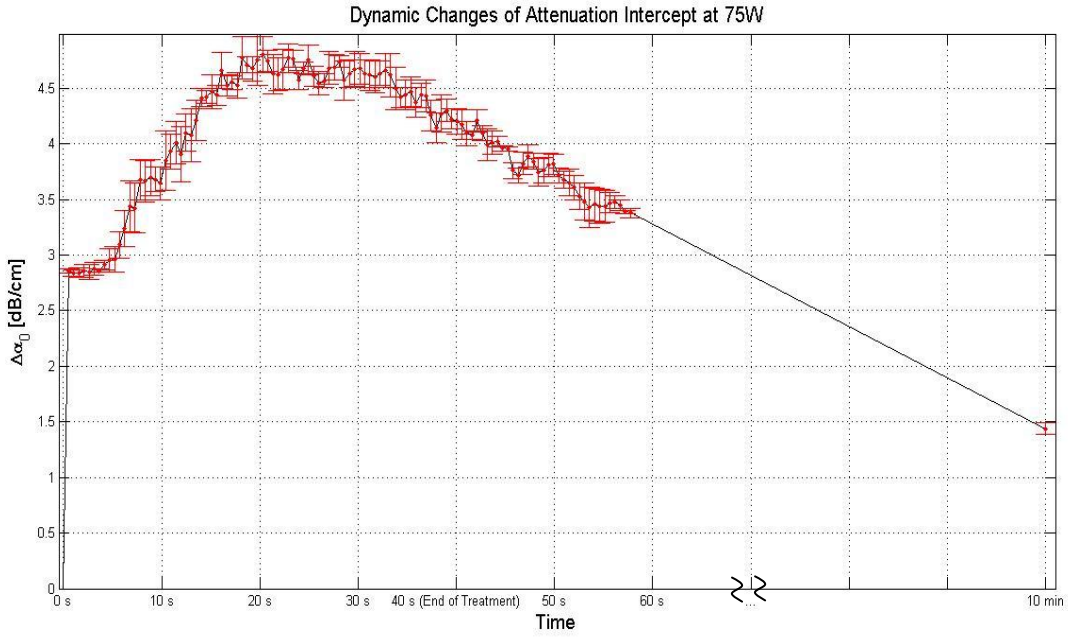

Figure 3-23 Dynamic changes of $\Delta\alpha_0$ (spatially averaged in ROI) in *ex vivo* porcine muscle tissue during HIFU treatment, for monitoring duration of 10 min, the input electric power of HIFU was 75 W, and the duty cycle was 77% for a total HIFU treatment time of 40 s

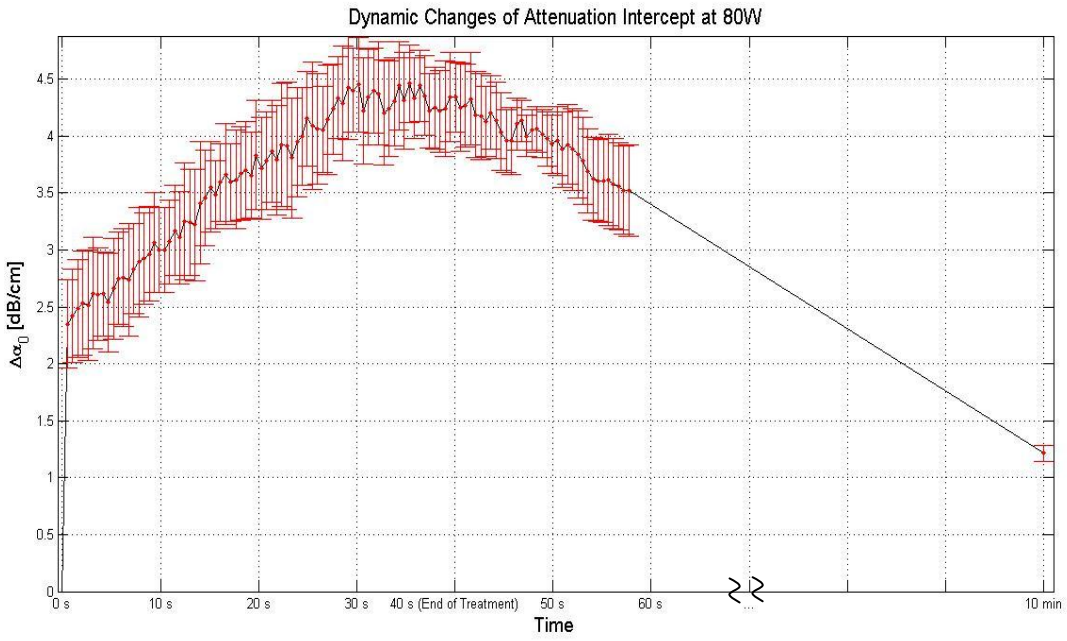

Figure 3-24 Dynamic changes of $\Delta\alpha_0$ (spatially averaged in ROI) in *ex vivo* porcine muscle tissue during HIFU treatment, for monitoring duration of 10 min, the input electric power of HIFU was 80 W, and the duty cycle was 77% for a total HIFU treatment time of 40 s

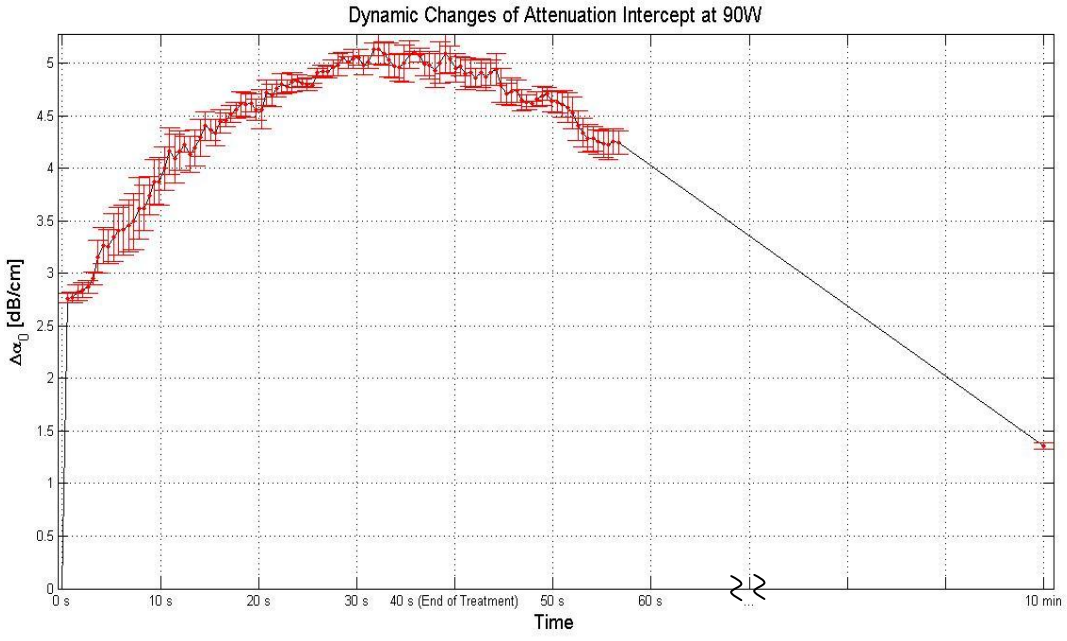

Figure 3-25 Dynamic changes of $\Delta\alpha_0$ (spatially averaged in ROI) in *ex vivo* porcine muscle tissue during HIFU treatment, for monitoring duration of 10 min, the input electric power of HIFU was 90 W, and the duty cycle was 77% for a total HIFU treatment time of 40 s

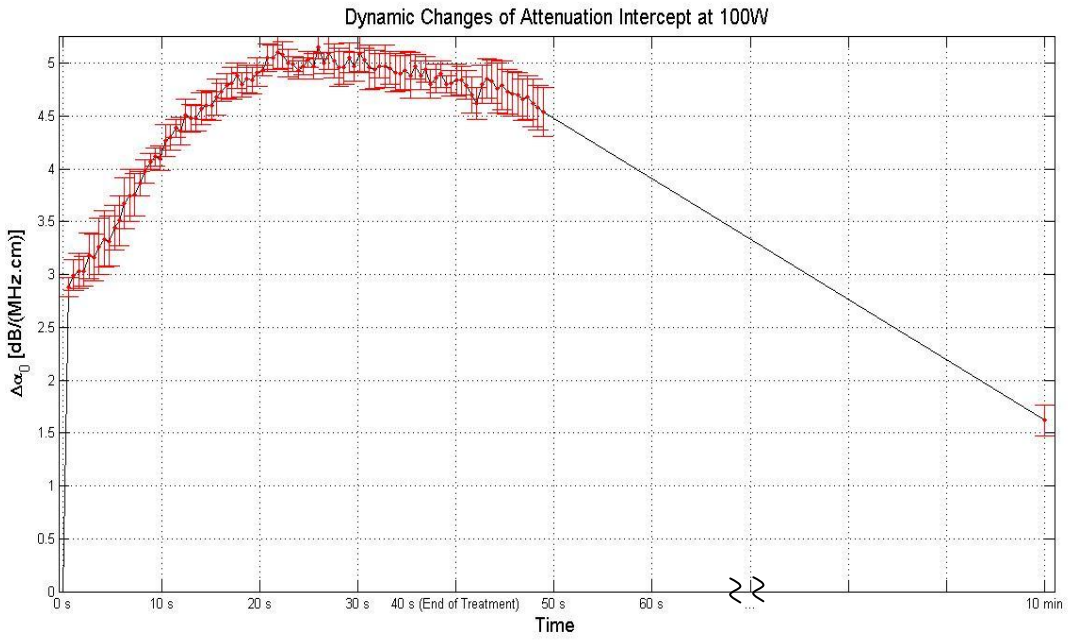

Figure 3-26 Dynamic changes of $\Delta\alpha_0$ (spatially averaged in ROI) in *ex vivo* porcine muscle tissue during HIFU treatment, for monitoring duration of 10 min, the input electric power of HIFU was 100 W, and the duty cycle was 77% for a total HIFU treatment time of 40 s

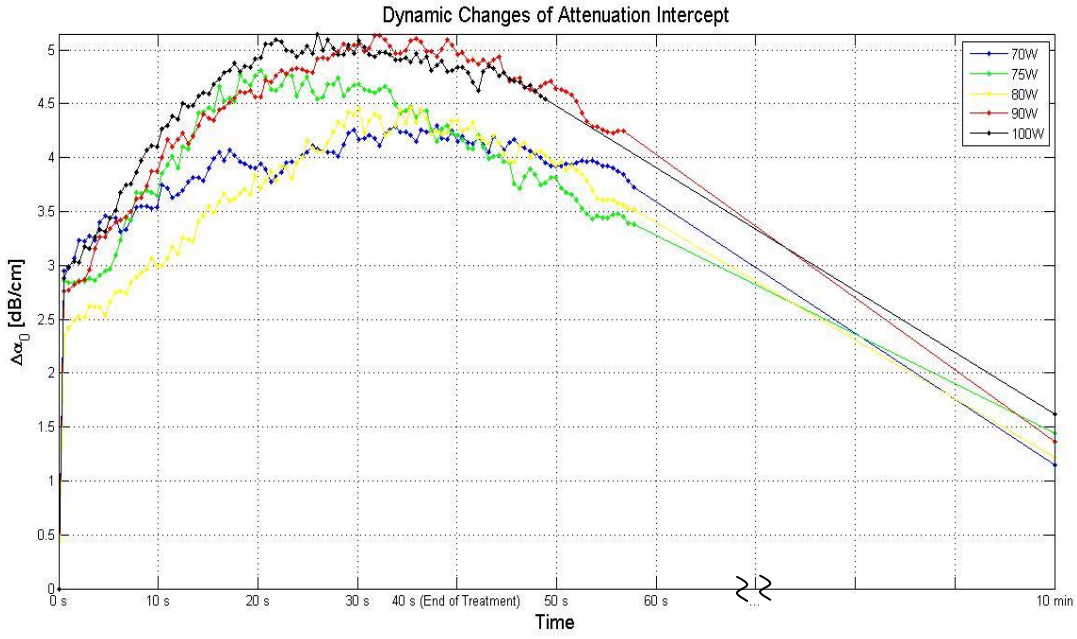

Figure 3-27 Dynamic changes of $\Delta\alpha_0$ (spatially averaged in ROI) in *ex vivo* porcine muscle tissue during HIFU treatment, for monitoring duration of 10 min, the input electric power of HIFU was 70 W, 75 W, 80W, 90 W, 100 W, and the duty cycle was 77% for a total HIFU treatment time of 40 s

Figure 3-22 to Figure 3-27 showed the dynamic changes of attenuation intercept as a result of HIFU treatment in *ex vivo* porcine muscle tissue at different input electric powers. These figures provided a quantitative assessment of the changes in $\Delta\alpha_0$.

As evident in Figure 3-27, at all input electric powers, $\Delta\alpha_0$ rose very rapidly in the first 20 s of treatment, from 0 to somewhere in the range of 4-5 $\frac{\text{dB}}{\text{cm}}$ and then maintained its value at that range with some fluctuations for the next 20 s to the end of HIFU treatment at 40 s. After the end of treatment, $\Delta\alpha_0$ gradually decreased and after10 minutes, the $\Delta\alpha_0$ algorithm detected values in the range of 1-1.6 $\frac{\text{dB}}{\text{cm}}$. Table 3-6 summarized the $\Delta\alpha_0$ values at 10 minutes, at different input electric powers.

Table 3-6 $\Delta\alpha_0$ values vs. input electric power, at t = 10 min

Input Electric Power (W)	$\Delta\alpha_0$ $(\frac{\text{dB}}{\text{cm}})$
70	1.15 ± 0.11
75	1.44 ± 0.05
80	1.21 ± 0.07
90	1.36 ± 0.03
100	1.62 ± 0.14

3.5.3 Comparison between the Attenuation Images and Conventional B-mode imaging

The attenuation slope and attenuation intercept algorithms used the same raw 2-D RF data that was used to form the B-mode frames. As a result, the $\Delta\beta$, $\Delta\alpha_0$, and B-mode images all had identical lateral resolutions. However, in terms of axial resolution, B-mode imaging clearly outperformed both algorithms. The reason lied in the fact that the $\Delta\alpha_0$ and $\Delta\beta$ were generated using a moving window function of length 5λ, with $\lambda = \frac{c}{f_c}$, where f_c was the imaging center frequency (during this study f_c = 4MHz). The moving window was shifted by $(2.5)\lambda$ at every iteration. This meant that the axial resolution for $\Delta\alpha_0$ and $\Delta\beta$ images was fixed at $\Delta z = (2.5)\lambda$

depending on the imaging center frequency (here $\Delta z = 0.96$ mm). On the other hand, the axial resolution of the conventional B-mode images was dependent only on the bandwidth of the imaging pulse (2 MHz) (Rahimian, 2010) and it was fixed at $\Delta z = \frac{1}{2}\frac{c}{BW}$ (~0.385). Therefore, in order to further quantitatively compare the performance of the attenuation slope (β) and attenuation intercept algorithms ($\Delta\alpha_0$) with each other, and further with conventional B-mode imaging, the contrast performances of all three different modes of generating images in this study were investigated.

Patterson and Foster (1983) proposed that the contrast between a given region of interest and the background can be represented as,

$$C = \frac{S_{in} - S_{out}}{S_{in}} \tag{3.10}$$

Where S_{in} was the mean signal measured inside a region of interest and S_{out} was the average signal measured from same-sized regions outside the region of interest. They further noted that if the variances of the signal within and outside of the region of interest were denoted by σ^2_{in} and σ^2_{out}, respectively, then a measure of speckle contrast fluctuations could be represented as,

$$S = \frac{\sqrt{\sigma_{in}^2 + \sigma_{out}^2}}{S_{in}} \tag{3.11}$$

Finally, using equation 3.10 and 3.11, they called the ratio of contrast (C) to the contrast fluctuations (S), contrast to speckle ratio, represented as,

$$CSR = \frac{S_{in} - S_{out}}{\sqrt{\sigma_{in}^2 + \sigma_{out}^2}} \tag{3.12}$$

CSR has been used by other researchers for assessing imaging quality of ultrasound images (Stetson, Sommer, & Macovski, 1997). In this study, CSR was used to assess the performance of each of the two attenuation mapping algorithms along with conventional B-mode imaging for lesions that were created at each of the investigated input electric power levels. To calculate CSR, equation 3.12 was used where S_{in} was the mean signal measured inside the region of interest (focal region) and S_{out} was the average signal measured from same-sized regions outside the region of interest, with the variances of the signal within and outside of the region of interest

being denoted by σ^2_{in} and σ^2_{out}, respectively. The region of interest was 10 mm × 10 mm, and centered around the lesion generated by HIFU as shown in Figure 3-10 and Figure 3-19.

To better assess the performances of attenuation algorithms ($\Delta\beta$ and $\Delta\alpha_0$) and B-mode imaging, CSRs were generated for two sets of images. First set consisted of frames acquired at less than 10 seconds right after the end of HIFU treatment, and the second set consisted of frames that were acquired at nearly 10 minutes after the end of treatment. As it was mentioned before, the fames acquired at 10 minutes represented the performance of each individual algorithm at steady state conditions where the bubbles (either cavitation or boiling) were no longer present and temperature had cooled down to its pre-treatment levels.

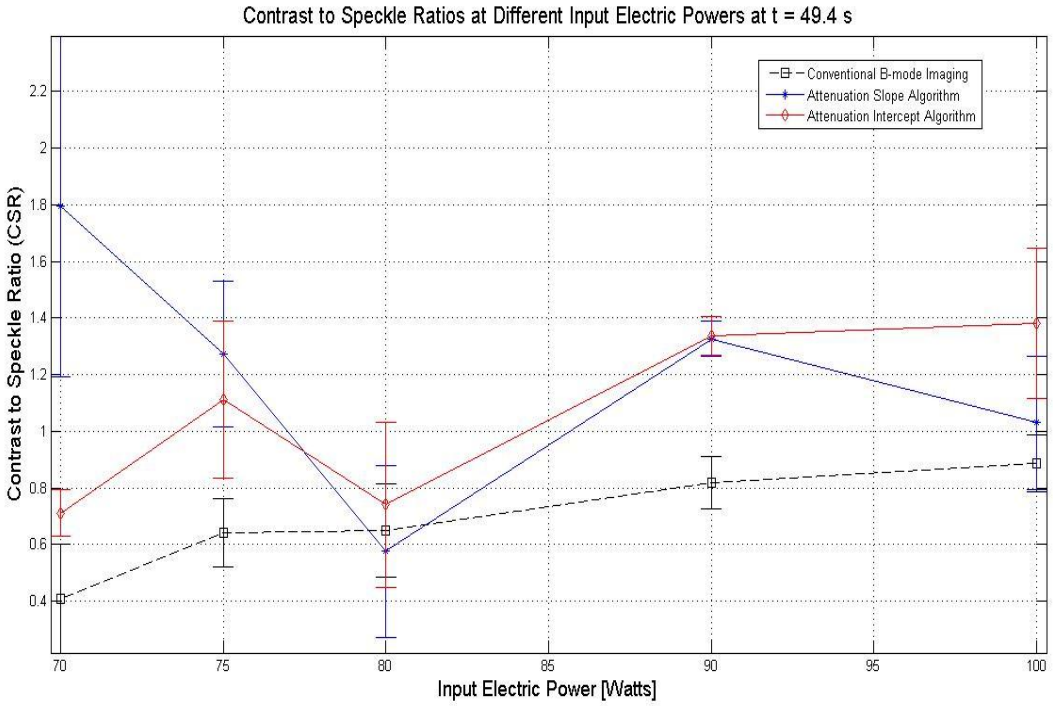

Figure 3-28 Comparison of contrast to speckle ratios at various input electric powers, less than 10 seconds after the end of HIFU treatment

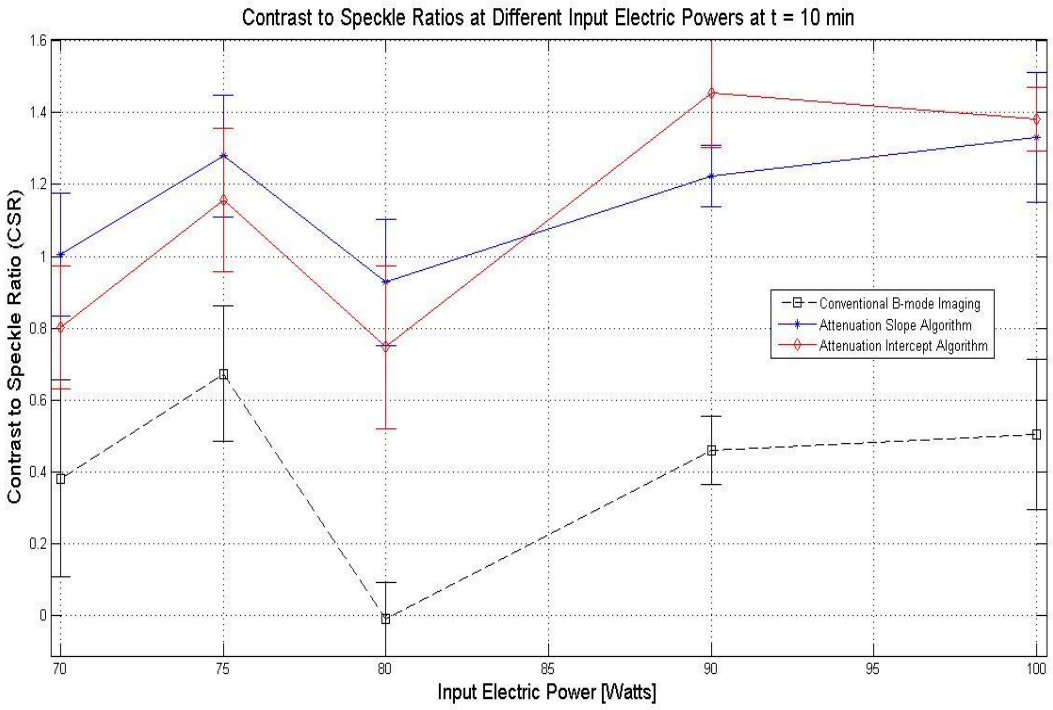

Figure 3-29 Comparison of contrast to speckle ratios at various input electric powers, less than 10 minutes after the end of HIFU treatment

4. Discussions and Conclusions

4.1 Attenuation Measurement on PVCP Phantoms

For verification purposes, the measured frequency dependent attenuation coefficient of the PVCP phantoms along with measurement results from an older study (Soleimankhani, 2007) were presented in Figure 3-7. The results of the older study were obtained from the exact same phantoms, using the same experimental apparatus and procedures. In comparison, it was evident that the results generated in this study closely matched the older measurement results, therefore showing a high degree of reproducibility of the measurement methodology and apparatus.

Based on the results presented in Figure 3-6 and Figure 3-7 it could safely be concluded that the measurement apparatus was capable of conducting attenuation measurements at a reasonably high precision. Moreover, since the main goal of this study was to investigate the *changes* between frequency dependent attenuation coefficients of normal and fully coagulated *ex vivo* porcine muscle tissues, the degree of accuracy of the measurement apparatus was not a determining factor in this study.

4.2 Attenuation Measurement on Normal and Coagulated *Ex vivo* Porcine Muscle Tissue

Results of attenuation measurements on normal and coagulated *ex vivo* porcine muscle tissues indicated that there was indeed a significant difference between the frequency dependent attenuation coefficients of normal and coagulated tissues. Furthermore, the results revealed that there was a 94% increase in the value of least squares attenuation coefficient slope (β) and 119% increase in the value of attenuation coefficient intercept (α_0) of coagulated *ex vivo* porcine muscle tissue with respect to normal *ex vivo* porcine muscle tissue.

At the time of this study there were no studies conducted on *ex vivo* porcine muscle tissues and therefore there were no other set of results available for comparison purposes. However, there

were many studies (Damianou, et al., 1997; Bush, et al., 1993; Gertner, et al., 1997; Goss, et al., 1979) conducted on other types of tissues based on changes in ultrasound tissue properties as a function of temperature or thermal dose in which it was similarly observed that as the temperature of tissue rose and ultimately the tissue became coagulated, there was a significant increase in ultrasound attenuation coefficient. For example, Bush et al. (1993) showed that the attenuation intercept, α_0, for *ex vivo* porcine liver increased by almost 100% at 5MHz. Similarly Gertner et al. (1997) showed that the attenuation intercept, α_0, for *ex vivo* bovine liver increased by 80% at 5MHz, while the attenuation slope, β, increased by 90%. So, to some extent the results of attenuation measurements conducted throughout this study once again confirmed the old findings in this regard.

Additionally, the results might further suggest that due to the larger percentage of increase in attenuation coefficient intercept (α_0), it might be used as a more reliable factor indicative of coagulation. Consequently, the change in attenuation coefficient intercept ($\Delta\alpha_0$) might generate better contrast (between normal and coagulated regions of tissue) and might be a better candidate for detection and localization of the region at which the thermal damage occurred in ultrasound imaging.

Based on these results, there was sufficient evidence that the frequency dependent ultrasound attenuation and its changes as a function of temperature and thermal dose might be a valuable tool in gaining more information towards HIFU-induced thermal lesion detection. Based on this evidence, in subsequent stages of this study, measurement of changes in ultrasound attenuation coefficient was exploited for monitoring of HIFU treatment on *ex vivo* porcine muscle tissues. More specifically, based on the material transfer function model, and the linear approximation of frequency dependent attenuation coefficient, changes in least squares attenuation coefficient slope ($\Delta\beta$), and changes in attenuation coefficient intercept ($\Delta\alpha_0$) were investigated as possible candidates for monitoring of HIFU treatments using pulse-echo ultrasound.

4.3 Attenuation Estimation Using Backscattered Ultrasound Pulses

It has been postulated that bubbles are usually formed soon after the beginning of the HIFU exposure at the HIFU treatment site (ter Haar G. R., 1995; Bailey, et al., 2001). These bubbles are either induced due to acoustic cavitation effects when the temperatures are still not high enough (referred to as cavitation bubbles), or due to boiling effects when the temperatures are sufficiently high (referred to as boiling bubbles) (ter Haar G. R., 1995; Bailey, et al., 2001). Acoustic cavitation is divided into stable cavitation defined as the linear or nonlinear oscillation of an acoustically driven bubble, and inertial cavitation defined as the unstable expansion of a bubble followed by a rapid violent collapse (Coussios, et al., 2007). Following their collapse, inertial cavitations radiate energy in the form of broadband emissions into their surrounding medium. However, as the temperature of the medium increases, inertial cavitation bubbles no longer act as broadband noise sources, and a stable cavitation field in the form of acoustically driven boiling bubbles remains. Visual observations suggest that these bubbles become very large (millimeter size) (Khokhlova, et al., 2006) and will therefore impact the local sound field primarily through acoustic scattering. Boiling bubbles are sufficiently large that they become clearly visible as a bright region in ultrasound B-mode images of the region treated with HIFU (Coussios, et al., 2007). The presence of these bubbles leads to blocking off the HIFU beam and consequently leads to unpredictable lesion shapes, commonly known as the "tadpole-shaped" lesions (ter Haar G. R., 1995; Bailey, et al., 2001). These unpredictable lesion structures have been observed in different studies and their presence has been attributed to ultrasound-induced cavitation or boiling effects (ter Haar G. R., 1995; Khokhlova, et al., 2006). Numerous examples of these "tadpole-shaped" lesions were observed throughout this study at various focal intensities. A few such examples are shown in Figure 4-1. As it is evident from the figure, the lesion pointed to by the red arrow is closest to the more conventional "cigar-shaped" lesions that are usually expected in HIFU treatments, while all the other lesions are more tadpole shaped. It should further be noted that all the lesions shown in Figure 4-1 were induced at the same average focal intensity of 801 $\frac{\mathrm{W}}{\mathrm{cm}^2}$.

Figure 4-1 Lesions induced in degassed *ex vivo* porcine muscle tissues, where the input electric power of HIFU was 75 W, the duty cycle was 77%, and the average focal intensity at the HIFU treatment site was 801 W/cm^2, for a total HIFU treatment time of 40 s

It has further been observed that as a result of HIFU exposure, hyperechoic regions form on the B-mode images at the HIFU treatment site (Bailey, et al., 2001). Previous studies on transparent tissue mimicking phantoms have shown the presence of violent bubble activities at the HIFU treatment site mainly due to boiling effects (Zhang, et al., 2009). These macroscopically-visible gas bubbles usually result in an increase in ultrasound scattering properties where they are present, further resulting in the formation of hyperechoic regions.

Throughout this study, bright hyperechoic regions appeared (at all the investigated HIFU intensities) in the B-mode images as soon as the HIFU was turned on in *ex vivo* porcine muscle tissues, and then faded rapidly right after HIFU was turned off as it was shown in Figure 3-9. Given the special process of degassing that was involved in preparation of tissue samples, and relatively high intensities at the HIFU treatment site, these bubbles were probably mainly due to boiling effects.

During HIFU treatment significant increases in the least squares attenuation coefficient slope (β), and attenuation coefficient intercept (α_0) were found in lesions created in *ex vivo* porcine muscle tissues. These results agreed with previous results by similar studies (Zhang, et al., 2009). During treatment, both $\Delta\beta$ and $\Delta\alpha_0$ rapidly increased, and then retained their values with some fluctuations until 10 seconds after the end of HIFU treatment (Figure 3-18and Figure 3-27). The presence of bubble activities were detected simultaneously by the presence of hyperechoic regions on the B-mode images. Therefore, the rapid increases in $\Delta\beta$ and $\Delta\alpha_0$ and their consequent fluctuations may be attributed to bubble activities causing abrupt changes in acoustic properties of the tissue at the HIFU treatment site. In one possible scenario, the formation of bubbles at the HIFU treatment site may have amplified the tissue ultrasound scattering properties (as evidenced by the presence of hyperechoic regions). Based on equation 2.5, this rapid increase in scattering of tissue at the HIFU treatment site leads to a rapid increase in the total attenuation of tissue at that location. In addition, this abrupt change in scattering properties of tissue significantly undermines our simplifying assumptions that scattering properties of any given soft biological tissue remained constant before, during, and after the HIFU treatment, causing instabilities in the material transfer function (MTF) model. Finally, it has been shown that as a result of temperature rise tissue absorption increases (Damianou, Sanghvi, Fry, & Maass-Moreno, 1997). Therefore, the rapid temperature rise at the site of HIFU treatment may have contributed to the rapid increase in $\Delta\beta$ and $\Delta\alpha_0$ values as well.

After HIFU treatment, the hyperechoic regions in the B-mode images rapidly faded. Corresponding to B-mode images, the high intensity regions in $\Delta\beta$ and $\Delta\alpha_0$ images began to decrease in size at a relatively slower rate, until they became stable at around 10 minutes after the end of treatment. This decrease in size may be attributed to the absence of bubbles long after the HIFU exposure, and the temperatures at the site of the HIFU exposure cooling down to pre-treatment levels. So, the high intensity regions detected in $\Delta\beta$ and $\Delta\alpha_0$ images at 10 minutes, could be used as true representations of the boundaries of the coagulated regions of the tissue.

In the case of the lesion that was monitored overnight, it was observed that the high intensity region further decreased in size and intensity as time passed from 10 minutes to 13 hours after the end of HIFU treatment. This decrease in size and intensity might be attributed to the fact that from 10 minutes to 13 hours after the completion of treatment, the temperature of the entire tissue and the focal spot significantly cooled down to below the pre-treatment levels. In addition,

the tissue might have absorbed water from the water bath that it was submerged in, leading to changes in scattering properties of the tissue and the region of interest, once again undermining our initial simplifying assumption that scattering properties of any given soft biological tissue remained constant before, during, and after the HIFU treatment, causing instabilities in the material transfer function (MTF) model.

It was initially expected that the dynamic changes of $\Delta\beta$ and $\Delta\alpha_0$ would be different for tissues treated with different HIFU powers. However, based on Figure 3-18 and Figure 3-27 there is no evidence of any significant differences for the dynamic changes of $\Delta\beta$ and $\Delta\alpha_0$ as functions of HIFU input electric power.

Attenuation measurement (insertion-loss) data resulted in $\Delta\beta = 0.67 \pm 0.14 \frac{\text{dB}}{\text{MHz.cm}}$ and $\Delta\alpha_0 = 2.87 \pm 0.75 \frac{\text{dB}}{\text{cm}}$ between normal and fully coagulated *ex vivo* porcine muscle tissues. Attenuation estimation using pulse-echo ultrasound on the other hand resulted in $\Delta\beta$ values in the range of 0.77-1.01 $\frac{\text{dB}}{\text{MHz.cm}}$ and $\Delta\alpha_0$ values in the range of 1.15-1.62 $\frac{\text{dB}}{\text{cm}}$ between normal and coagulated regions of *ex vivo* porcine muscle tissues as a result of HIFU treatments. Both sets of results (insertion-loss, and estimation using pulse-echo data) provide enough evidence to show that there is indeed a significant difference between the frequency dependent attenuation coefficients of normal and coagulated *ex vivo* porcine muscle tissues. However, the attenuation estimation data obtained from pulse-echo data does not replicate the attenuation measurement (insertion-loss) results. In the case of $\Delta\beta$, the attenuation slope algorithm overestimates the value of $\Delta\beta$ compared to the insertion-loss technique, while in the case of $\Delta\alpha_0$ the attenuation intercept algorithm underestimates the value of $\Delta\alpha_0$ compared to the $\Delta\alpha_0$ measured using insertion-loss technique.

Initially the attenuation measurement results suggested that attenuation intercept ($\Delta\alpha_0$) might be a better candidate for generating differential attenuation images compared to attenuation slope. However, in the current study, based on the contrast to speckle ratios at different investigated input electric powers at different times during the treatment cycle (Figure 3-28and Figure 3-29), there is not enough evidence to suggest that there is indeed a significant difference between the performance of the two algorithms ($\Delta\beta$ and $\Delta\alpha_0$) in terms of contrast to speckle ratios.

In comparison to conventional B-mode imaging, as evidenced by Figure 3-29 the attenuation algorithms significantly outperform the conventional B-mode images at all the investigated input

electric powers, 10 minutes after the HIFU treatment (in the absence of bubbles and temperature elevations). Given the increased echogenicity of the HIFU treatment sites during and a few seconds after HIFU treatments (due to presence of bubbles), it was initially expected that the conventional B-mode images would outperform the attenuation algorithms a few seconds after HIFU treatment. As shown in Figure 3-9, at t = 49.4 seconds, there was a significantly hyperechoic region that appeared on the B-mode image. However, based on Figure 3-28, there is not enough evidence to suggest that there is any significant difference between conventional B-mode imaging and $\Delta\beta$ and $\Delta\alpha_0$ maps while bubble activity is still present.

In the differential attenuation maps ($\Delta\beta$ and $\Delta\alpha_0$ images), after the creation of lesions, shadow regions right behind the induced lesions were expected to appear. The reason lied in the fact that the lesions represented high attenuation regions (with respect to the surrounding normal tissue) surrounded by normal tissue. Consequently, all the backscattered ultrasound pulses coming from the regions right behind the lesions would have to travel through the lesions (high attenuation regions) as well, and therefore be attenuated resulting in shadow regions. However, throughout this study, these shadow regions never appeared in any of the attenuation maps. The reason was due to the fact that the tissues used for HIFU treatment had relatively small thicknesses (2 cm), and the region right behind the induced lesions virtually consisted of just water. There were no scatterers in the water and therefore no backscattered pulses were generated. As a result the signal levels coming from the region right behind the induced lesions always remained constant at zero. While this shadow region results in an overestimation of the size of the induced lesions, it can also potentially be exploited as further indication of the presence of lesions.

The differential attenuation maps ($\Delta\beta$ and $\Delta\alpha_0$ images) could be very useful tools for detecting tissue thermal damages. Theses $\Delta\beta$ and $\Delta\alpha_0$ images can further be employed as color overlays on the pre-treatment B-mode images, therefore providing information about the size and location of tissue thermal damages (lesions) within the treated tissue.

Throughout this study, all the experiments were conducted in controlled experimental environments (e.g. minimal tissue movements and temperature deviations, consistent tissue preparation procedures, and etc.). During HIFU treatment, minor movements of the tissue samples due to the HIFU radiation force could result in movements of RF data acquisition plane, further inducing variances and artifacts in differential $\Delta\beta$ and $\Delta\alpha_0$ images. To minimize these variances and artifacts, the tissue samples were mounted in an acrylic tissue holder with an

acoustic window. Furthermore, while investigating the dynamic changes of $\Delta\beta$ and $\Delta\alpha_0$, the $\Delta\beta$ and $\Delta\alpha_0$ values were spatially averaged in the region of interest to minimize the effects of these variances. However, slight movements due to the HIFU radiation force, especially at higher powers, were always present to some extent.

4.4 Conclusions

We have obtained preliminary data for the changes in attenuation coefficient induced in *ex vivo* porcine muscle tissues due to coagulation. Changes in least squares attenuation coefficient slope ($\Delta\beta$) and attenuation coefficient intercept ($\Delta\alpha_0$) are both potentially reliable indicators of tissue thermal damage.

Following the preliminary data on $\Delta\beta$ and $\Delta\alpha_0$ that was obtained using measurement techniques, the transient characteristics of least squares attenuation coefficient slope and attenuation coefficient intercept were simultaneously investigated in a novel approach. In this new approach, based on a simplified model, $\Delta\beta$ and $\Delta\alpha_0$ values for any given location were estimated as functions of time and location, with respect to pre-treatment values of β and α_0 at that *same* location, before, during and after HIFU treatment at different HIFU powers, using pulse-echo ultrasound. The rapid increases in attenuation slope and attenuation intercept were generally accompanied by some fluctuations due to rapid rises in temperature and the bubble activities. Violent bubble activities were evident as hyperechoic regions in the B-mode images at the HIFU treatment sites. The performance of the B-mode images relied more on the effects of bubble activities than that of the $\Delta\beta$ and $\Delta\alpha0$ images. The dynamic changes of attenuation coefficient parameters ($\Delta\beta$ and $\Delta\alpha_0$) may be employed in the development of real-time monitoring and guidance of HIFU therapies, and evaluation of HIFU-induced lesions. However, at this point, further studies are necessary to determine the relative contributions of bubble activities and thermal tissue damage to the dynamic changes in attenuation coefficient parameters ($\Delta\beta$ and $\Delta\alpha_0$) in HIFU-induced lesions.

4.5 Future Work

In order to exploit the transient characteristics of $\Delta\beta$ and $\Delta\alpha_0$ further investigations are necessary in order to determine the relative contributions of bubble activities and tissue thermal damage to the rapid increases and oscillations of $\Delta\beta$ and $\Delta\alpha_0$ during HFU treatments. Therefore, in addition to the hyperechoic regions observed in conventional B-mode images, addition of a passive cavitation detection (PCD) system to the current system that was presented in Figure 2-8 may be necessary. PCD systems are relatively simple to implement. A typical PCD system consists of a single element cavitation detection transducer (sometimes referred to as the listening transducer), and a broadband receiver. The listening transducer is positioned so that its focus is orthogonal to the beam axis of the HIFU transducer, effectively covering the focal region of the HIFU beam (Zhang, et al., 2009; Coussios, et al., 2007). It can provide valuable information by collecting RF data scattered by the bubbles in the focal region during HIFU treatment. Having accurate quantitative information on bubble activities will result in more accurate and rigorous investigations of dynamic changes of acoustic parameters such as attenuation coefficient during HIFU treatment and transient characteristics of attenuation coefficient can be more accurately correlated with changes in subharmonic and broadband noise.

Instead of relying on the set of simplifying assumptions mentioned in section 2.3.3, further investigations may be carried out to study the possibility of expanding the material transfer function (MTF) so that, to some extent, it will take into account the effects of changes in scattering properties of tissue.

Finally, as mentioned before, the output of the attenuation slope and attenuation intercept algorithms ($\Delta\beta$ and $\Delta\alpha_0$ maps) can be employed as color overlays on the B-mode images, in real-time. Such a system will constantly provide feedback to the interventionist and therefore can be a valuable tool for real-time monitoring, guidance and control of HIFU procedures. Additionally, various image and signal processing techniques pertaining to biomedical signals (Rangayyan, 1996) can be employed to further improve the performance of the $\Delta\beta$ and $\Delta\alpha_0$ maps.

Appendix-A

Manufacturer Data for Single Element Ultrasound Transducers (Model V308; Olympus NDT, Waltham, MA, USA)

TRANSDUCER DESCRIPTION

PART NO.: V308 FREQUENCY: 5.00 MHz
SERIAL NO.: 546803 ELEMENT SIZE: .75 in. DIA.
DESIGNATION: 4 in. SPHERICAL FOCUS PTF

TEST INSTRUMENTATION

PULSER/RECEIVER: PANAMETRICS 5052UA #1
DIGITAL OSCILLOSCOPE: LeCroy LT342 / SN: LT34202249
TEST PROGRAM: TP103-3 VER. 108AAI
CABLE: RG-58 A/U LENGTH: 4FT

TEST CONDITIONS

PULSER SETTING: ENERGY: 1 ; DAMPING: 50 ohm
RECEIVER SETTING: ATTN: 28dB ; GAIN: 40dB
TARGET: .25 in. STEEL BALL; WATER PATH: 4.062in
JOB CODE: TP200

MEASUREMENTS PER ASTM E1065

FOCAL LENGTH ---- 4.062in.

WAVEFORM DURATION:
-14DB LEVEL -- .392US
-20DB LEVEL -- .488US
-40DB LEVEL -- 1.02US

SPECTRUM MEASURANDS:
CENTER FREQ. ---- 5.40MHz
PEAK FREQUENCY -- 5.44MHz
-6DB BANDWIDTH -- 60.624 %

COMMENTS:

S#: 46.55 F#: 5.54

** ACCEPTED.

TECHNICIAN: (3) _____ DATE: 03-30-2006

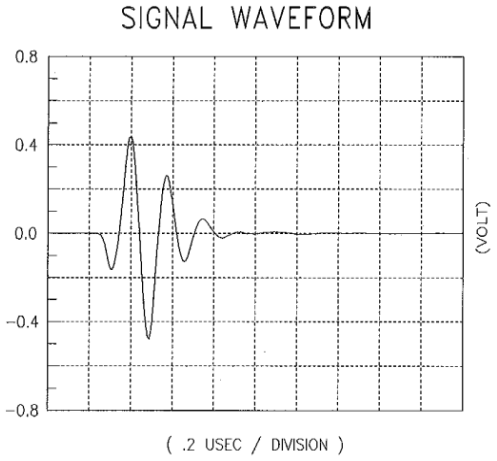

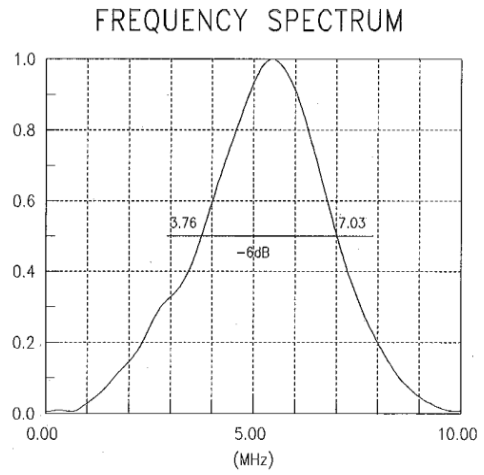

TRANSDUCER DESCRIPTION

PART NO.: V308 FREQUENCY: 5.00 MHz
SERIAL NO.: 556849 ELEMENT SIZE: .75 in. DIA.
DESIGNATION: 4 in. SPHERICAL PTF

TEST INSTRUMENTATION

PULSER/RECEIVER: PANAMETRICS 5052UA #4
DIGITAL OSCILLOSCOPE: LeCroy LT342 / SN: LT34201116
TEST PROGRAM: TP103-3 VER. 108AAI
CABLE: RG-58 A/U LENGTH: 4FT

TEST CONDITIONS

PULSER SETTING: ENERGY: 1 ; DAMPING: 50 ohm
RECEIVER SETTING: ATTN: 26dB ; GAIN: 40dB
TARGET: .25 in. STEEL BALL; WATER PATH: 3.983in
JOB CODE: TP200

MEASUREMENTS PER ASTM E1065

FOCAL LENGTH ---- 3.983in.

WAVEFORM DURATION:
-14DB LEVEL -- .416US
-20DB LEVEL -- 0.52US
-40DB LEVEL --*1.75US

SPECTRUM MEASURANDS:
CENTER FREQ. ---- 5.10MHz
PEAK FREQUENCY -- 5.20MHz
-6DB BANDWIDTH -- 61.002 %

COMMENTS:

S#: 46.66 F#: 5.2
* MEASUREMENT NOT PERFORMED OR MAY BE UNRELIABLE.

** ACCEPTED.

TECHNICIAN: (2)_____ DATE: 07-27-2006

SIGNAL WAVEFORM

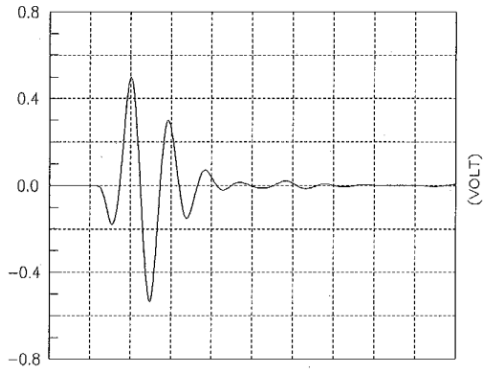

(.2 USEC / DIVISION)

FREQUENCY SPECTRUM

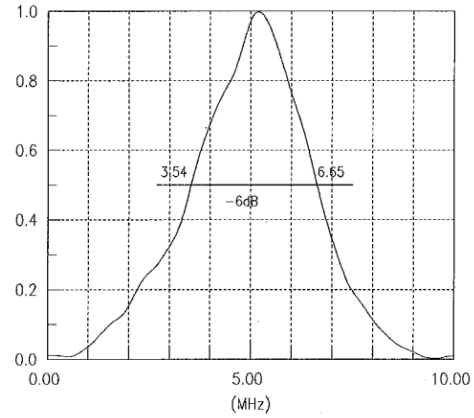

Appendix-B

Experimental Data for Single Element Ultrasound Transducers (Model V308; Olympus NDT, Waltham, MA, USA)

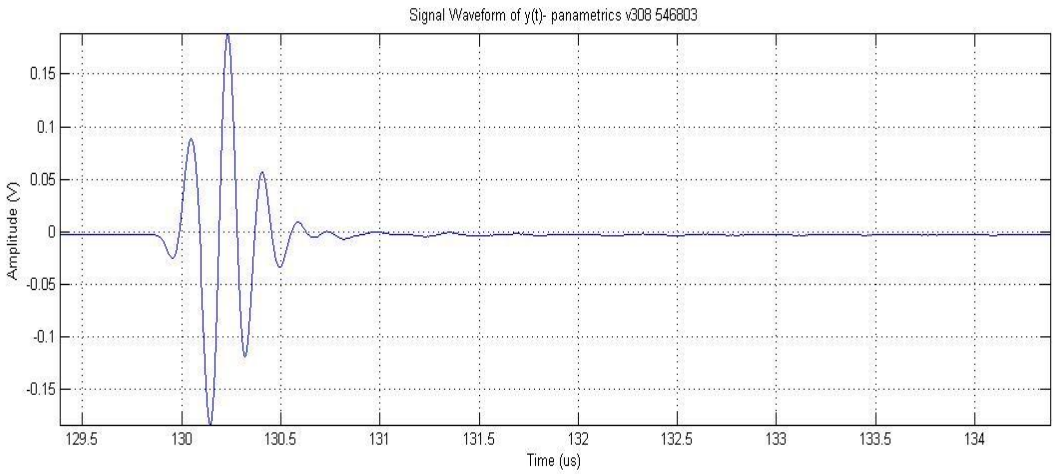

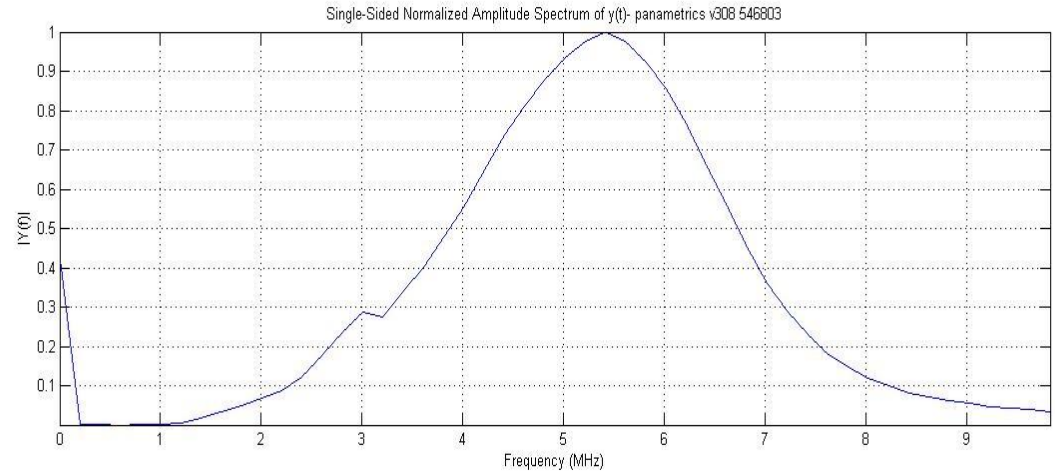

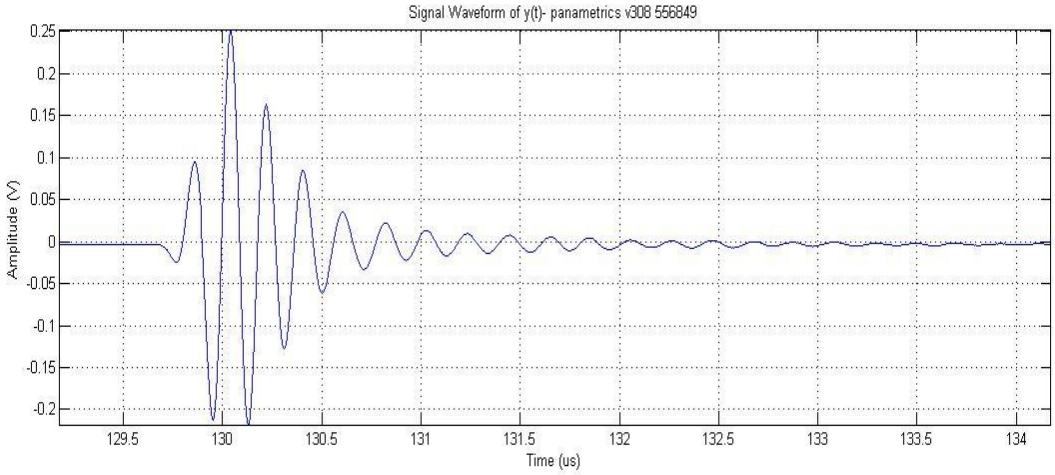
Signal Waveform of y(t)- panametrics v308 556849
Amplitude (V)
Time (us)
0.25
0.2
0.15
0.1
0.05
0
-0.05
-0.1
-0.15
-0.2
129.5
130
130.5
131
131.5
132
132.5
133
133.5
134

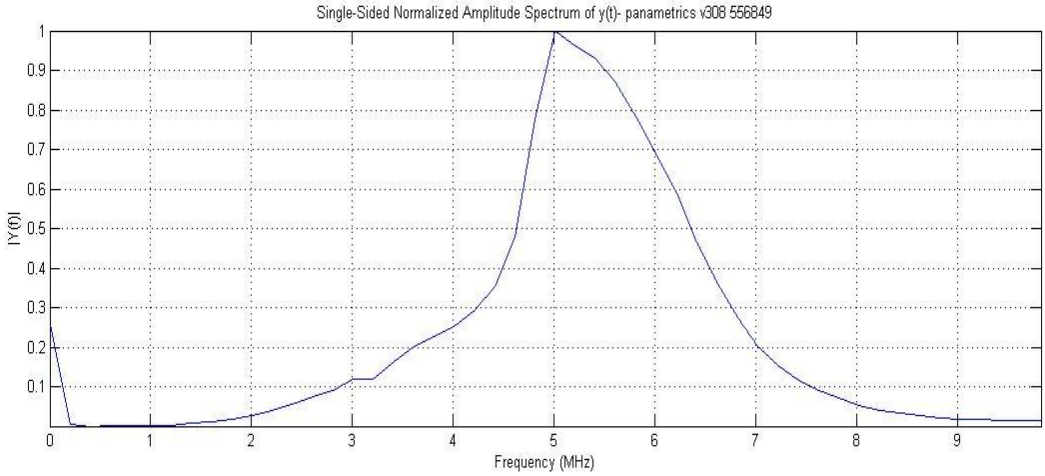
Single-Sided Normalized Amplitude Spectrum of y(t)- panametrics v308 556849
|Y(f)|
Frequency (MHz)
1
0.9
0.8
0.7
0.6
0.5
0.4
0.3
0.2
0.1
0
1
2
3
4
5
6
7
8
9

Appendix-C

Attenuation Slope Algorithm ($\Delta\beta$)

n: is the line number in each frame, and n $\in$[1,128].

T: is the value of time at any given moment throughout the treatment cycle (before, during, and after). It represents the time at which any given frame is obtained in seconds. For example for an exposure duration of 10s, T = 0 represents the frame obtained at the moment right before the beginning of the exposure. T $\in$ [1s, 10s] represents all the frames obtained during the exposure, and T>10s, represents all the frames obtained after the completion of the exposure.

T_0: represents the pre-exposure time, the time at which the first frame right before the exposure is obtained. It represents T = 0s.

echo(n,T): represents each RF line n, acquired at time T.

echo(n,T_0): represents each RF line n, acquired at time T=0s. It is referred to as the reference line.

output(j,n,T): is a set of 2D matrices representing changes in β[dB/(MHz.cm)] (as a function of time (T), depth (z), and line number), with respect to the reference frame obtained at T_0 (T = 0s).

wf: represents the Blackman windowing function. Throughout this investigation a Blackman window of length 5λ was utilized. Taking f = f_c, c_0 = 1540 m/s, and f_s = 40MHz, The window length was 120 samples.

The following represents the algorithm,

```
for T = 1:1:T_final
    for n =1:128
        while(the end of line n has not been reached)

            %(1)Window the signal RF line at n, T
            Windowed_Echo_Signal = wf(echo(n,T))
```

```
            %(2)Window the reference RF line at n, T0
            Windowed_Echo_Reference = wf(echo(n,T0))

            %(3)Take the fft of the windowed signal
            Spectrum_Signal = fft(Windowed_Echo_Signal)

            %(4)Take the fft of the windowed reference
            Spectrum_Reference = fft(Windowed_Echo_Reference)

            %(5)Take the natural logarithm of the signal spectrum,  and
            %take the real part
            S_signal = -Re(ln(Spectrum_Signal))

            %(6)Take the natural logarithm of the reference spectrum,  and
            %take the real part
            S_reference = -Re(ln(Spectrum_Reference))

            %(7) subtract S_reference from S_signal
            deltaS = S_signal - S_reference

            %(8)Fit a line to deltaS, using only the points in the frequency
            %range 3MHz-6MHz

            %(9)Divide the value of slope of the fitted line by 2z, and store
            %it in variable SLOPE

            %(10)Store of the variable SLOPE in the output matrix
            for j = beginning of window: end of window
                output(j,n,T)= output(j,n,T) + SLOPE
            end

            %(11)Shift the window by half the length of the window

        end

    %(12)Reset the window and bring it back to the beginning of the line(z=0)

    end
end
```

Appendix-D

Attenuation Intercept Algorithm ($\Delta\alpha_0$)

n: is the line number in each frame, and n $\in$[1,128].

T: is the value of time at any given moment throughout the treatment cycle (before, during, and after). It represents the time at which any given frame is obtained in seconds. For example for an exposure duration of 10s, T = 0 represents the frame obtained at the moment right before the beginning of the exposure. T $\in$ [1s, 10s] represents all the frames obtained during the exposure, and T>10s, represents all the frames obtained after the completion of the exposure.

T_0: represents the pre-exposure time, the time at which the first frame right before the exposure is obtained. It represents T = 0s.

echo(n,T): represents each RF line n, acquired at time T.

echo(n,T_0): represents each RF line n, acquired at time T=0s. It is referred to as the reference line.

output(j,n,T): is a set of 2D matrices representing changes in β[dB/(MHz.cm)] (as a function of time (T), depth (z), and line number), with respect to the reference frame obtained at T_0 (T = 0s).

wf: represents the Blackman windowing function. Throughout this investigation a Blackman window of length 5λ was utilized. Taking f = f_c, c_0 = 1540 m/s, and f_s = 40MHz, The window length was 120 samples.

The following represents the algorithm,

```
for T = 1:1:T_final
    for n =1:128
        while(the end of line n has not been reached)

            %(1)Window the signal RF line at n, T
```

```
            Windowed_Echo_Signal = wf(echo(n,T))

            %(2)Window the reference RF line at n, T0
            Windowed_Echo_Reference = wf(echo(n,T0))

            %(3)Take the fft of the windowed signal
            Spectrum_Signal = fft(Windowed_Echo_Signal)

            %(4)Take the fft of the windowed reference
            Spectrum_Reference = fft(Windowed_Echo_Reference)

            %(5)Take the natural logarithm of the signal spectrum,  and
            %take the real part
            S_signal = -Re(ln(Spectrum_Signal))

            %(6)Take the natural logarithm of the reference spectrum,  and
            %take the real part
            S_reference = -Re(ln(Spectrum_Reference))

            %(7) subtract S_reference(fc) from S_signal(fc)
            delta_Alpha0 = S_signal(fc) - S_reference(fc)

            %(8)Store of the variable delta_Alpha0 in the output matrix
            for j = beginning of window: end of window
                output(j,n,T)= output(j,n,T) + delta_Alpha0
            end

            %(9)Shift the window by half the length of the window

        end

    %(10)Reset the window and bring it back to the beginning of the line(z=0)

    end
end
```

Bibliography

Anand, A., Savery, D., & Hall, C. (2007). Three-dimensional spatial and temporal temperature imaging in gel phantoms using backscattered ultrasound. *IEEE Trans Ultrasound Ferroelectr Freq Control* , 54:23-31.

Arefiev, A., Prat, F., Chapelon, J. Y., Tavakkoli, J., & Cathignol, D. (1998). Ultrasound-induced tissue ablation: studies on isolated perfused porcine liver. *Ultrasound Med. Biol.* , 24: 1033-1043.

Arthur, R. M., Straube, W. L., Starman, J. D., & Moros, E. G. (2003). Noninvasive temperature estimation based on the energy of backscattered ultrasound. *Med Phys* , 30:1021-1029.

Bailey, M. R., Couret, L. N., Sapozhnikov, O. A., Khokhlova, V. A., ter Haar, G. R., Vaezy, S., et al. (2001). Use of overpressure to assess the role of bubbles in focused ultrasound lesion shape in vitro. *Ultrasound Med Biol* , (27) 695-708.

Bailey, M. R., Khokhlova, V. A., Sapozhnikov, O. A., Kargl, S. G., & Crum, L. A. (2003). Physical Mechanisms of Therapeutic Effect of Ultrasound. *Acoustical Physics* , 49(4):369-388.

Bamber, J. C. (1998). Ultrasonic Properties of Tissues. In F. A. Duck, & A. C. Baker, *Ultrasound in Medicine.* Bristol: Institute of Physics Publishing.

Bamber, J. C., & Hil, C. R. (1979). Ultrasonic attenuation and propagation speed in mammalian tissues as a function of temperature. *Ultrasound Med Biol* , 5:149-157.

Bevan, P. D., & Sherar, M. D. (2001b). B-scan ultrasound imaging of thermal coagulation in bovine liver: Frequency shift attenuation mapping . *Ultrasound Med Biol* , 27:809-817.

Bevan, P. D., & Sherar, M. D. (2001a). B-scan ultrasound imaging of thermal coagulation in bovine liver: log envelope slope attenuation mapping. *Ultrasound Med Biol* , 27:379-387.

Bleier, A. R., Jolesz, F. A., Cohen, M. S., & Weisskoff, R. M. (1991). Real-Time Magnetic Resonance Imaging of Laser Heat Deposition in Tissue. *Magnetic Resonance in Medicine* , 21:132-137.

Bloch, S., Michael, R., Crum, L. A., Kaczkowski, P. J., Keilman, G. W., & Mourad, P. D. (1998). Measurements of sound speed in excised tissue over temperatures expected under high-intensity focused ultrasound conditions. *J Acoust Soc Am* , 103:2868.

Burov, A. K. (1956). High intensity ultrasonic vibrations for action on animal and human malignant tumours. *Dokl. Akad. Nauk.* , (106)239-241.

Bush, N. L., Rivens, I., ter Haar, G. R., & Bamber, J. C. (1993). Acoustic Properties of Lesions Generated with an Ultrasound Therapy System. *Ultrasound Med Biol* , 9:789-801.

Butt, F. (2011). *High Performance Computing for Linear Acoustic Wave Simulation.* M. Sc. thesis, Toronto: Ryerson University.

Butt, F., & Tavakkoli, J. (2011). *Linear Acoustic and Temperature Simulation (LATS) version 1.2.* Toronto: Ryerson University, Department of Physics.

Butt, F., Abhari, A., & Tavakkoli, J. (2011). An application of high performance computing to improve linear acoustics simulation. *Spring Simulation Multi-Conference (SpringSim11)* (pp. 71-78). Boston, MA, USA: Conference Proceedings.

Chaussy, C., Brendel, W., & Schmiedt, E. (1980). Extracorporeallu induced destruction of kidney stones by shock waves. *Lancet* , 2(8207):1265-68.

Chivers, R. C., & Hill, C. R. (1975). Ultrasonic attenuation in human tissue. *Ultrasound Med. Biol.* , (2):25-29.

Cobbold, R. S. (2007). *Foundations of Biomedical Ultrasound.* New York: Oxford University Press, Inc.

Cohen, I. K., Diegelmann, R. F., & Lindblad, W. J. (1992). In W. B. Suanders, *Wound healing: Biochemical and Clinical Aspects* (pp. 1-630). Philadelphia.

Coleman , D. J., Lizzi, F. L., Driller, J., Rosado, A. L., Torpey, J. H., Smith, M. E., et al. (1985c). Therapeutic ultrasound in the treatment of glaucoma-II Clinical applications. *Ophthalmology* , (92)347-353.

Coleman, D. J., Lizzi, F. L., Driller, J., Rosado, A. L., Chang, S., Iwamoto, T., et al. (1985b). Therapeutic ultrasound in the treatment of glaucoma-I Experimental Model. *Ophthalmology* , (92)339-346.

Coleman, D. J., Lizzi, F. L., Torpey, J. H., Burgess, S., Driller, J., Rosado, A. L., et al. (1985a). Treatment of experimental lens capsular tears with intense focused ultrasound. *Br. J. Ophthalmol.* , (69)645-649.

Coussios, C. C., Farny, C. H., ter Haar, G., & Roy, R. A. (2007). Role of acoustic cavitation in the delivery and monitoring of cancer treatment by high-intensity focused ultrasound (HIFU). *International Journal of Hyperthermia* , 23(2): 105-120.

Daffertshofer, M., & Hennerici, M. (2003). Ultrasound in the treatment of ischemic stroke. *Lancet-Neurol* , (2):283-290.

Damianou, C. A., Sanghvi, N. T., Fry, F. J., & Maass-Moreno, R. (1997). Dependence of ultrasonic attenuation and absorption in dog soft tissue on temperature and thermal dose. *J Acoust Soc Am* , 102:628-634.

Fahey, B. J., Nightingale, K. R., Stutz, D. L., & Trahey, G. E. (2004). Acoustic radiation force impulse imaging of thermally- and chemically induced lesions in soft tissues: Preliminary ex vivo results. *Ultrasound Med Biol* , 30:321-328.

Frenkel, V. (2011). *Therapeutic Ultrasound, Mechanisms to Applications.* New York: Nova Science Publishers.

Fry, F. J. (1958). Precision high intensity focusing ultrasound machines for surgery. *Am. J. Phys. Med.* , (37)152-156.

Fry, W. J., & Fry, F. J. (1960). Fundamental neurological research and human neurosurgery using intense ultrasound. *IRE Trans. Med. Electron.* , (ME-7)166-181.

Fry, W. J., Barnard, J. W., Fry, F. J., Krumins, R. F., & Brennan, J. F. (1955). Ultrasonic lesions in the mammalian central nervous system. *Science* , (122)517-518.

Gelet, A., Chapelon, J. Y., Bouvier, R., Rouviere, O., & Lasne, Y. (2000). Transrectal high-intensity focused ultrasound: minimally invasive therapy of localized prostate cancer. *J. Endourol.* , 14(6):519-28.

Gertner, M. R., Wilson, B. C., & Sherar, M. D. (1997). Ultrasound Properties of Liver Tissue During Heating. *Ultrasound Med Biol* , 9:1395-1403.

Goss, S. A., Frizzell, L. A., & Dunn, F. (1979). Ultrasonic Absorption and Attenuation in Mammalian Tissues. *Ultrasound Med Biol* , 5:181-186.

Harris, G. R. (1981). Review of transient field theory for a baffled planar piston. *Journal of the Acoustical Society of America* , 70(1):10-20.

Heisterkamp, J., Matheijssen, N., & van Hillegersberg, R. (1999). Accuracy of MR phase mapping for temperature monitoring during interstitial laser coagulation (ILC) in the liver at rest and simulated respiration. *MRM* , (41):919-925.

Hill, C. R., Rivens, I., Vaughan, M. G., & ter Haar, G. R. (1994). Lesion development in focused ultrasound surgery: A general model. *Ultrasound Med. Biol.* , (20):259-269.

Huisman, H., & Thijssen, T. (1996). Precision and accuracy of acoustospectrographic parameters. *Ultrasound in Medicine and Biology* , 22:855-871.

Hynynen, K. (1991). The threshold for thermally significant cavitation in dog's thigh muscle in vivo. *Ultrasound Med Biol* , 17:157-169.

Hynynen, K., Damianou, C. A., & Colucci, V. (1995). MR monitoring of focused ultrasonic surgery of renal cortex: Experimental and simulation studies. *JMRI* , 5(3):259-266.

Hynynen, K., Darkazanli, A., Unger, E., & Schenck, J. F. (1993). MRI-guided noninvasive ultrasound surgery. *Med. Phys.* , 20(1):107-115.

Hynynen, K., Freund, W. R., Cline, H. E., Chung, A. H., & Watkins, R. D. (1996). A clinical, noninvasive, MR imaging-monitored ultrasound surgery method. *Radiographics* , 16)1:185-95.

Ishihara, Y., Calderon, A., Watanabe, H., Okamoto, K., Suzuki, Y., Kuroda, K., et al. (1995). A Precise and Fast Temperature Mapping Using Water Proton Chemical Shift. *MRM* , 34:814-823.

Jolesz, F. A., & Hynynen, K. (2007). *MRI-Guided Focused Ultrasound Surgery.* New York, NY: Informa Healthcare.

Khokhlova, V. A., Bailey, M. R., Reed, J. A., Cunitz, B. W., Kaczkowski, P. J., & Crum, L. A. (2006). Effects of nonlinear propagation, cavitation, and boiling in lesion formation by high intensity focused ultrasound in a gel phantom. *J Acoust Soc Am* , (119)1834-1848.

Kim, H. J., Greenleaf, J. F., Kinnick, R. R., & Bronk, J. T. (1996). Ultrasound mediated transfection of mammalian cells . *Human Gene Ther.* , (7):1339-1346.

Le Bihan, D., Delannoy, J., & Levin, R. (1989). Temperature mapping with MR imaging of molecular diffusion: application to hyperthermia . *Radiology* , 171:853-857.

Lynn, J. G., & Putnam, T. J. (1944). Histological and cerebral lesions produced by focused ultrasound. *Am. J. Pathol.* , (20)637-649.

Lynn, J. G., Zwemmer, R. L., Chick, A. J., & Miller, A. F. (1942). A new method for the generation and use of focused ultrasound in experimental biology. *J. Gen. Physiol.* , (26)179-193.

Matsumoto, R., Mulkern, R. V., Hushek, S. G., & Jolesz, F. A. (1994). Tissue Temperature Monitoring for Thermal Interventional Therapy: Comparison of T1-weighted MR sequences. *JMRI* , 4:65-70.

Mencaglia, L., Guidetti, R., Tonellotto, D., & Fanfani, A. (2000). Energy focused ultrasound for the clinical treatment of uterine myoma. *Ultrasound Med. Biol.* , 26(2):A207.

Miller, N. R., Bamber, J. C., & Meany, P. M. (2002). Fundamental limitations of noninvasive temperature imaging by means of ultrasound echo strain estimation. *Ultrasound Med Biol* , 28:1319-1333.

Moriarty, J., Chen, J., & Purcell, C. (1998). MRI monitoring of interstitial microwave-induced heating and thermal lesions in rabbit brain in vivo. *JMRI* , 8(1):128-135.

Nassiri, D. K., & Hill, C. R. (1986). The differential and total bulk acoustic scattering cross sections of some human and animal tissues. *J. Acoust. Soc. Am.* , (79):2034-2047.

Ocheltree, K. B., & Frizzell, L. A. (1989). Sound field calculation for rectangular sources. *IEEE transactions on ultrasonics, ferroelectrics, and frequency control* , 36(2):242-248.

Ophir, J., Shawker, T., Makland, N. F., & Miller, J. G. (1984). Attenuation Estimation in Reflection: Progress and Prospects. *Ultrasonic Imaging* , 6:349-395.

Parker, K. J. (1983). Ultrasonic attenuation and absorption in liver tissue. *Ultrasound in Med Biol* , 9:363-369.

Parker, K. J., Huang, S. R., Musulin, R. A., & Lerner, R. M. (1990). Tissue response to mechanical vibrations for sonoelasticity imaging. *Ultrasound Med Biol* , 16:241-246.

Patterson, M. S., & Foster, F. S. (1983). The improvements and quantitative assessment of B-mode images produced by an annular array/cone hybrid. *Ultrasonic Imaging* , (5):195-213.

Peters, R., Hinks, R., & Henkelman, R. (1998). Ex vivo tissue-type independence in proton-resonance frequency shift MR thermometry. *Magnetic Resonance in Medicine* , (40):454-459.

Pilla, A. A., Mont, M. A., Nasser, P. R., Khan, S. A., Fgueiredo, M., Kaufman, J. J., et al. (1990). Non-invasive low intensity pulsed ultrasound accelerates bone healing in the rabbit . *J. Orthopaed. Trauma* , 4: 246-253.

Rahimian, S. (2010). *EC9-5/10: Understanding the Received Signal.* Toronto: Ryerson University.

Rangayyan, R. M. (1996). *Biomedical Signal Analysisn A Case-Study Approach.* Piscataway, NJ: IEEE Press.

Ribault, M., Chapelon, J. Y., Cathignol, D., & Gelet, A. (1998). Differential attenuation imaging for the characterization of high intensity focused ultrasound lesions. *Ultrasound Imaging* , 20:160-177.

Righetti, R., Kallel, F., Stafford, R. J., Price, R. E., Krouskop, T. A., Hazle, J. D., et al. (1999). Elastographic characterization of HIFU-induced lesions in canine livers. *Ultrasound Med Biol* , 25:1099-1113.

Rosenthal, I., Sostaric, J. Z., & Riesz, P. (2004). Sonodynamic therapy- a review of the synergistic effects of drugs and ultrasound. *Ultrason. Sonochem.* , (11):349-363.

Sanghvi, N. T., Foster, R. S., Bihrle, R., & Uchida, T. (1999). Noninvasive surgery of prostate tissue by high intensity focused ultrasound: an updated report. *Eur. J. Ultrasound* , 9(1):19-29.

Schafer, S., Kliner, S., Klinghammer, L., Kaarman, H., Lucic, I., Nixdorff, U., et al. (2005). Influence of ultrasound operating parameters on ultrasound-induced thrombolysis in vitro. *Ultrasound Med. Biol.* , (31):841-847.

Seip, R., & Ebbini, E. S. (1995). Noninvasive estimation of tissue temperature response to heating fields using diagnostic ultrasound . *IEEE Trans Biomed Eng* , 42:828-839.

Seip, R., Tavakkoli, J., Carlson, R. F., Wunderlich, A., Sanghvi, N. T., Dines, K. A., et al. (2002). High-Intensity Focused Ultrasound (HIFU) Multiple Lesion Imaging: Comparison of Detection Algorithms for Real-Time Treatment Control. *IEEE Ultrasonics Symposium*, (pp. 1395-1398).

Seo, J., Tran, B. C., Hall, T. L., Fowlkes, J. B., O'Donnell, M., & Cain, C. A. (2002). Evaluation of ultrasound tissue damage based on changes in image echogenicity. *Proc IEEE Ultrason Symp* , 2:1431-1434.

Shi, X., Martin, R. W., Rouseff, D., Vaezy, S., & Crum, L. A. (1999). Detection of high-intensity focused ultrasound liver lesions using dynamic elastometry. *Ultrasonic Imaging* , 21:107-126.

Siegel, R. J., Atar, S., Fishbein, M. C., Brasch, A. V., & Peterson, T. M. (2000). Noninvasive, transthoracic, low-frequency ultrasound augments thrombolysis in a canine model of acute myocardial infraction. *Circulation* , 101(17):2026-29.

Simon, C., VanBaren, P., & Ebbini, E. S. (1998). Two-dimensional temperature estimation using diagnostic ultrasound . *IEEE Trans Ultrason Ferroelectr Freq Control* , 45:1088-1099.

Soleimankhani, E. (2007). *An investigation of the use of transmission ultrasound to guide minimally invasive thermal therapy.* M. Sc. thesis, Tonronto, Ontario, Canada: Ryerson University.

Souchon, R., Rouviere, O., Gelet, A., Detti, V., Srinivasan, S., Ophir, J., et al. (2003). Visualization of HIFU lesions using elastography of the human prostate in vivo: Preliminary results. *Ultrasound Med Biol* , 29:1007-1015.

Spirou, G. M., Oraevsky, A. A., Vitkin, A., & Whelan, W. M. (2005). Optical and acoustic properties at 1064 nm of polyvinyl chloride-plastisol for use as a tissue phantom in biomedical optoacoustics . *50* (14).

Stauffer, P. R., Diederich, C. J., & Seegenschmiedt, M. H. (1995). Chapter 13: Interstitial Heating Techniques. In M. H. Seegenschmiedt, P. Fessenden, & C. C. Vernon, *Thermoradiotherapy and Thermochemotherapy* (pp. 253-278). Berlin Heidelberg: Springer-Verlag.

Stetson, P. F., Sommer, F. G., & Macovski, A. L. (1997). Lesion constrast enhacement in medical ultrasound imaging. *IEEE Trans. Ulrason. Ferroelect. Freq. Contr.* , (16)416-425.

Stollberger, R., Ascher, P., & Huber, D. (1997). Temperature monitoring of interstitial thermal tissue coagulation using MR phase images. *JMRI* , 8:188-196.

Szabo, T. (2004). Attenuation. In T. Szabo, *Diagnostic Ultrasound Imaging: Inside Out* (pp. 72-90). Elsevier Academic Press.

Tavakkoli, J., & Sanghvi, N. T. (2011). Ultrasound-Guided HIFU and Thermal Ablation. In V. Frenkel, *Therapeutic Ultrasound, Mechanisms to Applications* (pp. 137-161). New York: Nova Science Publishers.

ter Haar, G. (1988). Biological Effects of Ultrasound in Clinical Applications. In *Ultrasound: Its Chemical, Physical, and Biological Effects* (pp. 305-320). New York: VCH.

ter Haar, G. R. (1995). Ultrasound focal beam surgery . *Ultrasound Med. Biol. 21* , 1089-1100.

ter Haar, G. R., & Robertson, D. (1993). Tissue destruction with focused ultrasound in vivo. *Eur. Urol. 23* , (Suppl. 1), 8-11.

ter Haar, G. (2006). Therapeutic application of ultrasound. *Progress in Biophysics & Molecular Biology* , 111-129.

Thomsen, S. (1999). Mapping of Thermal Injury in Biologic Tissues Using Quantitative Pathologic Techniques. *SPIE Conference on Thermal Treatment of Tissue with Image Guidance* (pp. 82-95). San Jose: SPIE.

Thomsen, S., Pearce, J. A., Randeri, R., & Chan, E. (1995). Determination of Isotherms of Thermal Damage. *IEEE/LEOS*, (pp. 2295-2296).

Vaezy, S., Andrew, M., Kaczkowski, P., & Crum, L. (2001b). Image-Guided Acoustic Therapy. *Annu. Rev. Biomed. Eng.* , 3:375-390.

Vaezy, S., Shi, X., Martin, R. W., Chi, E., Nelson, P. I., Bailey, M. R., et al. (2001a). Real-time visualization of high-intensity focused ultrasound treatment using ultrasound imaging. *Ultrasound Med Biol* , 27:33-42.

Visioli, A. G., Rivens, I. H., ter Haar, G. R., Horwich, A., & Huddart, R. A. (1999). Preliminary results of a phase I dose escalation clinical trial using focused ultrasound in the treatment of localised tumours. *Eur. J. Ultrasound* , 9(1):11-18.

Waterman, F. (1995). Chapter 15: Invasive Thermometry Techniques. In M. Seegenschmiedt, P. Fessenden, & C. Vernon, *Thermoradiotherapy and Thermochemotherapy* (pp. 1: 253-278). Berlin : Springer.

Wells, P. N. (1975). Abrosption and dispersion of ultrasound in biological tissue. *Ultrasound Med. Biol.* , (1):369-376.

Zhang, S., Wan, M., Zhong, H., Xu, C., Liao, Z., Liu, H., et al. (2009). Dynamic Changes of Integrated Backscatter, Attenuation Coefficient and Bubble Activities During High-Intensity Focused Ultrasound Treatment. *Ultrasound in Medicine and Biology* , 35:(11), pp. 1828-1844.

Zheng, X., & Vaezy, S. (2010). An acoustic backscatter-based method for localization of lesions induced by high-intensity focused ultrasound. *Ultrasound Med. Biol.* , 36(4):610-622.